(4)
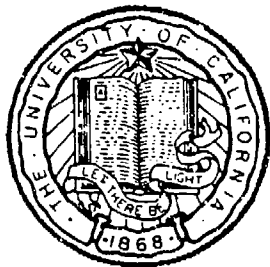
MARINE PHYSICAL LABORATORY

SCRIPPS INSTITUTION OF OCEANOGRAPHY

San Diego, California 92152

AD-A220 009

On Array Performance: A Methodology of System Calibration and Noise Identification

B. J. Sotirin and W. S. Hodgkiss

MPL TECHNICAL MEMORANDUM 410

90 04 02 181

REPORT DOCUMENTATION PAGE

1a. REPORT SECURITY CLASSIFICATION	1b. RESTRICTIVE MARKINGS
UNCLASSIFIED	

2a. SECURITY CLASSIFICATION AUTHORITY	3. DISTRIBUTION/AVAILABILITY OF REPORT
2b. DECLASSIFICATION/DOWNGRADING SCHEDULE	Approved for public release; distribution unlimited.

4. PERFORMING ORGANIZATION REPORT NUMBER(S)	5. MONITORING ORGANIZATION REPORT NUMBER(S)
MPL Technical Memorandum 410 [MPL-U-25/89]	

6a. NAME OF PERFORMING ORGANIZATION	6b. OFFICE SYMBOL (If applicable)	7a. NAME OF MONITORING ORGANIZATION
Marine Physical Laboratory	MPL	Office of Naval Research Department of the Navy

6c. ADDRESS (City, State, and ZIP Code)	7b. ADDRESS (City, State, and ZIP Code)
University of California, San Diego Scripps Institution of Oceanography San Diego, CA 92152	800 North Quincy Street Arlington, VA 22217-5000

8a. NAME OF FUNDING/SPONSORING ORGANIZATION	8b. OFFICE SYMBOL (If applicable)	9. PROCUREMENT INSTRUMENT IDENTIFICATION NUMBER
Office of Naval Research	ONR	N00014-87-C-0127

8c. ADDRESS (City, State, and ZIP Code)	10. SOURCE OF FUNDING NUMBERS			
Department of the Navy 800 North Quincy Street Arlington, VA 22217-5000	PROGRAM ELEMENT NO.	PROJECT NO.	TASK NO.	WORK UNIT ACCESSION NO.

11. TITLE (Include Security Classification)
ON ARRAY PERFORMANCE: A METHODOLOGY OF SYSTEM CALIBRATION AND NOISE IDENTIFICATION

12. PERSONAL AUTHOR(S)
B. J. Sotirin and W. S. Hodgkiss

13a. TYPE OF REPORT	13b. TIME COVERED	14. DATE OF REPORT (Year, Month, Day)	15. PAGE COUNT
tech memo	FROM ___ TO ___	June 1989	83

16. SUPPLEMENTARY NOTATION

17. COSATI CODES			18. SUBJECT TERMS (Continue on reverse if necessary and identify by block number)
FIELD	GROUP	SUB-GROUP	acoustic arrays, oceanic ambient noise, system noise sources, Electronic Equipment, FLIP

19. ABSTRACT (Continue on reverse if necessary and identify by block number)

The assumption that acoustic array measurements are a true reflection of the oceanic noise field can lead to misinterpretation of the data collected. Characterization of the array self noise levels and knowledge of individual element amplitude and phase responses are required to assess the results with confidence. In recent years emphasis on low frequencies and high resolution has led to the development of large aperture arrays with many elements. Establishing individual element calibrations and system noise levels of these arrays is not easily achieved in the laboratory environment due to facility and time constraints. Therefore, a series of tests are suggested to assist in the identification of system noise sources in such an array using a combination of oceanic ambient noise measurements and limited laboratory measurements. An in-situ element calibration is also discussed which compares magnitude estimates from two independent methods and generates a phase error curve. These methods are somewhat limited by incomplete knowledge of the environmental parameters and the statistical nature of ambient noise. Results are demonstrated using data collected by a large aperture vertical array deployed from the research platform FLIP in the NE Pacific. Floating Instrument Platform

20. DISTRIBUTION/AVAILABILITY OF ABSTRACT	21. ABSTRACT SECURITY CLASSIFICATION
☐ UNCLASSIFIED/UNLIMITED ☒ SAME AS RPT. ☐ DTIC USERS	UNCLASSIFIED

22a. NAME OF RESPONSIBLE INDIVIDUAL	22b. TELEPHONE (Include Area Code)	22c. OFFICE SYMBOL
W. S. Hodgkiss	(619) 534-1798	MPL

DD FORM 1473, 84 MAR — 83 APR edition may be used until exhausted. All other editions are obsolete

On Array Performance:
A Methodology of System Calibration and Noise Identification

B. J. Sotirin and W. S. Hodgkiss

Marine Physical Laboratory
Scripps Institution of Oceanography
University of California, San Diego
La Jolla, CA 92093

ABSTRACT

The assumption that acoustic array measurements are a true reflection of the oceanic noise field can lead to misinterpretation of the data collected. Characterization of the array self noise levels and knowledge of individual element amplitude and phase responses are required to assess the results with confidence. In recent years emphasis on low frequencies and high resolution has led to the development of large aperture arrays with many elements. Establishing individual element calibrations and system noise levels of these arrays is not easily achieved in the laboratory environment due to facility and time constraints. Therefore, a series of tests are suggested to assist in the identification of system noise sources in such an array using a combination of oceanic ambient noise measurements and limited laboratory measurements. An *in-situ* element calibration is also discussed which compares magnitude estimates from two independent methods and generates a phase error curve. These methods are somewhat limited by incomplete knowledge of the environmental parameters and the statistical nature of ambient noise. Results are demonstrated using data collected by a large aperture vertical array deployed from the research platform *FLIP* in the NE Pacific.

1

On Array Performance:
A Methodology of System Calibration and Noise Identification

B. J. Sotirin and W. S. Hodgkiss

Marine Physical Laboratory
Scripps Institution of Oceanography
University of California, San Diego
La Jolla, CA 92093

Introduction

Acoustic arrays are commonly used to study many aspects of the ocean environment such as propagation effects, background noise, deep scattering layers, internal wave fields, and bottom characteristics to name a few. Interpretation of the data collected by such arrays must be viewed in terms of the array characteristics. All to often however, for data processing expediency, the characteristics of the array are assumed to be inconsequential and the effects of the instrumentation are not considered. This unrealistic attitude may lead to unsubstantiated conclusions.

The theoretical effect of element failure and random amplitude and phase errors on array sidelobe level has been examined by other investigators [Ramsdale and Howerton, 1980; Quazi and Nuttall, 1979; Quazi, 1982; Nuttall, 1979] and should there be element failures, algorithms for optimal reshading exist [Sherrill and Streit, 1987]. However, techniques for estimating these errors are not typically discussed.

Error sources must be realistically identified in order to separate the desired signal from the measurement. The measurement encompasses the hydrophone input modified by the channel response plus system noise. Our experience has been that catastrophic element failure occurs seldomly in real applications and post processing of array data must include criteria to identify elements with low performance, and evaluate their effect with respect to the application. The amplitude measurement of the incoming signal may be corrupted by a variety of factors including variable hydrophone sensitivities, inaccurate gain amplifiers, quantizing errors, saltwater leakage, cable response, crosstalk, ground loops and digital switching noise. The phase measurement of the incoming signal may be modified by the element location, the phase response of electrical components and cables, crosstalk, switching noise and timing errors.

The purpose of this paper is to present a methodology for characterizing large aperture array system noise and estimating channel amplitude and phase responses using *in-situ* data. The methods recommended are applied to data collected by a 900 m, 120 channel acoustic array which was deployed vertically from the research platform *FLIP* in the Northeast Pacific during September 1987. Laboratory tests were minimized because of the large number of channels, the size of the array and time and facility constraints. Array system noise is characterized using ambient noise data collected during the experiment and when possible verified by subsystem laboratory tests. To estimate channel amplitude and phase errors, ambient noise and a series of narrowband signals transmitted from a known location with known source level were used.

I. System Description

Array description with regard to system performance must address the physical and electrical attributes of the signal path. Utilizing *in-situ* data places the individual array elements in an almost constant temperature and pressure environment however the response of exposed components to the lower temperature and higher pressure must be considered. Physical layout of the signal path must also be considered for potential cross-talk, grounding and noise contamination. Design amplitude and phase characteristics for individual filters, amplifiers, cables, converters, etc. should be recorded. For coherent processing, the timebase in the array must be accurately calibrated and system delays accounted for.

The array addressed in this paper was composed of 120 elements separated physically into 12 hose sections each containing 10 elements spaced 7.5 meters apart with the first and last elements being 3.75 meters from either end of a hose. The sections were terminated at processor pressure cases which contain the electronics to process the data from the 10 physically closest elements. Therefore, electrically the elements in a single hose section were associated with two processors. The data stream originated at the hydrophones. It was amplified, filtered, converted to a digital signal, reformatted and finally transmitted to the surface where it was recorded on magnetic tape in real time. A detailed description of the entire array system is found in [Sotirin and Hildebrand, 1988].

One section of the low frequency signal path in the array is shown schematically in Figure 1.1. The power for the analog components is supplied by 12 individual section switching power supplies whose 5 VDC, 250 ma input is supplied by the 350 VDC, 4 A high power line running the length of the array. Array elements consisted of the transducer, preamplifier, anti-aliasing filter and differential line driver. The transducers were composed of two Aquadyne AQ-1 hydrophones wired in series to increase the sensitivity to a nominal -197 dB re 1 V/μPa each with a 12 nF capacitance at mid ocean depths. The hydrophone output is amplified by a very low noise FET with 40 dB of fixed gain and a low frequency cutoff below 10 Hz. The preamplifier output is filtered by a phase matched, six pole, low pass filter with a corner frequency of 220 Hz and an in-band gain of 1. A differential line driver is used to transmit the bandpassed amplified signal to the processor, a distance of up to 37.5 meters. Each processor receives signals from 10 elements, 5 from the hose section above and 5 from the hose section below. The two elements immediately adjacent to a processor are filtered within the processor pressure case rather than at the element to provide access to the 12 KHz acoustic information required for navigating the array [Sotirin and Hildebrand, 1989]. All array element components are subjected to ambient oceanic pressure.

Within the processor pressure case, the element inputs follow a common path. Each input is selected sequentially by a differential multiplexer, converted from differential to single-ended, amplified by a programmable variable gain amplifier (14 to 60 dB), then captured by a sample-and-hold circuit and converted to 12 bit digital form. In digital form the data is less susceptible to degradation by component response, noise, cross-talk and ground loops. The digital data integrity is monitored by several counters and synchronization words which are verified prior to processing. The timing for each processor is controlled by individual oscillators which are phase locked to a 1 MHz clock signal running the length of the array. Digital component delays (typically on the order of ns) are negligible at the 500 Hz (2 ms) data sampling rate. The sequential operation of the multiplexer imparts a deterministic phase shift of $\omega n\tau$ where ω is the frequency, n is the channel position (defined in Appendix A) and τ is the 0.2 ms sample frequency.

II. Laboratory Calibration

Laboratory tests were minimized due to lack of facilities in which an environmentally controlled system test could be executed and time constraints. Tests were performed under one atmosphere pressure and room temperature with no special electrical shielding. Nominal element calibration was conducted during array construction and the self noise tests were conducted for a 10 element array subsection. Typically, these tests are completed prior to the experiment to verify minimum operating conditions. However, during the September 1987 experiment, strict time constraints delayed completion of the tests until after the experiment.

Nominal Element Calibration. Each element was tested individually as it was constructed and the array hose section assembled. Within a hose section are the hydrophones, preamplifiers, filters and line drivers for 10 elements. As these electronics are subjected to ambient ocean pressures during deployment, the individual components used were pressure soaked and cycled to 8000 psi prior to fabrication. Typical hydrophone amplitude, phase and impedance responses were measured with respect to temperature and pressure [Lastinger. 1982]. Before the array is pulled into the urethane hose section, several tests were conducted to measure the pass band level, and -3 dB cutoff frequencies of the filters. Data for this test is presented in Appendix A. The pass band level was measured at 100 Hz by injecting a sinusoid electronically at the hydrophone input and monitoring the results at the differential line driver output. The signal is amplified by 40 dB in the preamplifier and received differentially, adding an additional 6 dB. The noise in this preamplifier has been measured to be approximately 30 dB re 1 μPa at 100 Hz in a shielded controlled environment. The level recorded is in dB referenced to the signal injected amplified by 46 dB, that is, the setup is designed to output a measurement of 0.0 dB for this test. All elements exhibit a pass band level at 100 Hz within ± 1 dB of the design level except the top element and the bottom element which are within 1.2 dB.

The high frequency cutoff was designed to accommodate a 500 Hz sampling frequency. The -3 dB cutoff frequency was measured by increasing the frequency of the signal injected as described above and monitoring the same output. Two elements in each section are low pass filtered after the signal is received by the processor to allow detection of the 12 kHz navigation pulses. These elements have an expected -3 dB cutoff frequency at 15 kHz. The remaining elements roll off at about 220 Hz. The low frequency cut off is about 5 Hz for all elements.

The operating environment at each individual element during a sea test is stable in temperature (at 3 °C) and pressure. The element components should be invariant when subjected to this environment. The components most likely to change would be the capacitors. Preliminary pressure and temperature tests were conducted during which the capacitors were found to be virtually invariant over a pressure range of 0 to 6000 psi but capacitance values decreased with temperature. A decrease in capacitance increases the high frequency cutoff, and increases the potential for aliasing problems.

Electrical Self Noise Level. Laboratory tests conducted to determine the level of the electronic noise floor in the array were delayed until after the experiment. These tests consisted of decoupling the inputs to various stages of the signal path from the array and changing specific control options to ascertain the origin and amplitude of the array self noise. No special precautions were taken to insure the noise integrity of the array in the lab environment, therefore the data was subjected to a variety of additional noise sources which would not be encountered in an ocean environment. The narrow band signals apparent in the spectral plots are not stationary and are normally identified with an outside source such as machinery

magnetostriction components and ship radar [Anderson, 1989].

The tests were conducted using 10 representative array elements. One array hose section was removed from the urethane tube and the hydrophone inputs to the preamplifiers were replaced by equivalent capacitors (channels 6-15). These 10 channels are addressed by two processors; processor 1 (P1) monitors channels 1-10, processor 2 (P2) monitors channels 11-20. The ±15 volt power leads were removed from the elements whose phones were still connected (channels 1-5 and 16-20). The tests were conducted by recording data utilizing the same system setup as was used at sea [Sotirin and Hildebrand, 1988]. The plots shown in Figures 2.2 and 2.3 are generated by incoherently averaging 46 FFT's (Kaiser-Bessel window, α = 2.5) with 50% overlap which estimates the spectra within a confidence interval of +1.4 dB to -1.2 dB [Bendat and Piersol, 1971]. Increasing the number of averages to generate a confidence interval between +0.5 and -0.4 did not appreciably alter any of the spectra levels or character. The magnitude is normalized to a 1 Hz band and does not account for the array gain amplification but treats the array signal as a black box input at the analog-to-digital converter (ADC) to facilitate comparison between the gain settings. The actual noise levels initiated at the element are amplified by the fixed gain stage of 46 dB and by the variable gain stage which is notated on the individual plots. These levels are on the order of a microvolt making it extremely difficult to insure absolute repeatability in the tests within the lab environment available.

The noise levels at various stages in the analog power circuit and data stream were measured. The power for the analog circuits must be regulated and free of harmonic content. In this array, the main array power supply was located aboard *FLIP* and each processor case contained two switching DC-to-DC converters, one at a +5 VDC output and the other at ±15 VDC output. Frequency response for the input and two outputs are shown in Figure 2.1. The input to the converters has a significant 120 Hz level (-75.4 dBv/√Hz) which is filtered and appears in the 5 VDC output at a low level (about -112 dBv/√Hz); there are other intermittent narrow band peaks at 55 Hz and 6 Hz. There is also a 60 Hz signal at about -116 dBv/√Hz. The noise level in the ±15 volt power supply is quite flat with a 2 dB increase at 60 Hz to a -124.2 dBv level (Figure 2.1c). These narrow band levels are quite low and appear only intermittently in the low frequency self noise data. Contributors to the array self noise were identified by shorting the inputs to or bypassing stages. The spectra of the array system noise with the input to the variable gain stage shorted (see Figure 2.2f) was flat with an 8 or 9 mv variation at the ±10 volt ADC indicating that no unexpected noise sources were active in this stage. The 12 bit ADC had a resolution of 4.8828 mv which when normalized over the system bandwidth of 250 Hz (23.98 dB) corresponds to a -70.2 dB level. There were two multiplexer modes, the scan on mode which samples each of 10 channels with a user selectable (5 kHz default) sampling frequency, and the scan off mode which samples only one channel. The noise contributed by the multiplexer and sample-and-hold amplifier (SHA) was measured by comparing the levels obtained with the input to the multiplexer for channel 8 (P1H2) hardwired to the differential receiver effectively bypassing the multiplexer, to those obtained using the same channel with the multiplexer operating in the scan off mode and during normal operation (scan on). Each exhibited the same spectral levels and characteristics indicating that no additional noise was injected at the multiplexer or SHA.

Although the data signals were driven differentially, there is the possibility of coupling common mode noise into the relatively low level analog data. The digital switching noise from the 1 MHz clock signal running the length of the array was of high enough level that it was not completely removed by the differential receivers (common mode rejection ratio of 80 dB). Clock noise is suspected in Figure 2.2 as spectrum levels tend to increase with wire length in the array (physical phone

position from the processor) by as much as 15 dB. This noise was substantially decreased by the addition of a small 0.0153 μf capacitor at each of the multiplexer inputs which effectively shorts the inputs of the differential receiver at frequencies above about 10 kHz, indicating that it is high frequency noise generated in the array hose. As the variable gain is increased two distinct effects are noticeable. First, for a specific variable gain increase, the spectral levels are not amplified by the same amount channel to channel. Second, the relative spectral level increase in any particular channel does not coincide with the change in variable gain. Both of these effects could be attributed to high frequency noise being slew rate limited in the variable gain amplifier. Limiting the slew rate would effectively filter out the high frequency content and amplify only the low frequency portion, creating a gain discrepancy channel to channel and because slew rate increases as gain increases, more of the high frequency noise would be blocked, rectifying the discrepancies between channels as the gain is increased. These effects are shown in Figure 2.3 which displays the difference between channels 11 and 15 (farthest and closest respectively) and the channel 11 output for different variable gains. Ideally, as the variable gain is increased from 34 dB (top) to 54 dB (bottom), the magnitudes in Figure 2.3a should always be 0 or at least constant, indicating that both channels are amplifying the signal by the same amount. This is the case only at a gain setting of 54 dB, where the slew rate filter effect would be strongest, eliminating more of the high frequency noise. The difference between channels increases as the gain and the slew rate limitations decrease. The second effect is observed by examining the change in magnitude for channel 11 (Figure 2.3b) as the gain increases. Changing the variable gain from 34 to 44 dB should produce a 10 dB increase in magnitude rather than the 4-5 dB increase shown for channel 11; although the effect is substantially less, there is an 15-20% reduction in effective gain in the closest channels as well.

This noise exhibits a coherent structure shown in Figure 2.4 which is effectively removed by the line filter capacitors. The high coherence effect is limited to only a few channels in the section and does not appear in the directionality plot of Figure 2.5. The beam levels are very consistent with no substantial increase in the broadside beam which is indicative of pervasive common mode noise. The array self noise levels at a relatively low array gain are compared (Figure 2.6) to corresponding measured ambient noise at the same gain settings. The quality of the high frequency data depends on the level of the incoming signal, the array variable gain setting and the channel position. The amount of degradation is elucidated in the following section.

III. Performance Indicators

In-situ performance tests require a knowledge of the acoustic noise field used as a signal to enable identification of array system problems. Each test shows a different facet of array data characteristics and requires some interpretation.

Time Series. A 4 s time series of either the voltage (Figure 3.1) or power response of each channel provides insight into the signals received by the array, identifying biological disturbances, noise levels, and signal levels. It also insures that all sections of the array are telemetering, and clearly identifies certain types of occurrences such as dead channels (e.g. 71), insensitive channels (e.g. 21,100), high frequency glitches (e.g. 30, 77), saturation due to strum (e.g. 94, 99, 116), and saturation due to DC offsets (e.g. 75). Examination of an impulsive return during the experiment revealed a polarity reversal in some of the channels (indicated in Table A1) which was subsequently corrected and is not shown in the figures presented here.

6

Time Series Distribution. A histogram of the time series monitored by each channel indicates the voltage distribution of the signal being recorded. The distribution was calculated with 0.1 v bins over 16 s, and shows a Gaussian random process (left half of Figure 3.2). The variance of the distribution increases with gain and low frequency vibrations as in channel 18. The mean of the distribution corresponds to the DC offset of the channel (channel 16). The spikey character of channel 20 is an artifact of the software error discussed below.

Bit Distribution. The correct operation of the analog to digital converter (ADC) and some aspects of bit formatting and reformatting are verified by examining the distribution of each of the channel bits. If the ADC is correctly converting zero mean Gaussian random signals, the distribution of each bit representing the 2's complement digital signal should be high half of the time and low half of the time as the signal varies between positive and negative numbers, shown in Figure 3.3 by simulation. The simulations were implemented by generating a Gaussian random signal in volts with a different seed for each panel in Figure 3.3, clipping at $\pm$ 10 v (as the ADC does) and converting it to bit integer format before accumulating the high bits. The output format of the ADC's in the array was offset binary and the data was converted to 2's complement prior to the telemetry link. The conversion only requires that the most significant bit be complemented so the 2's complement representation is adequate for this investigation. The zero mean simulated signals have the expected distribution even in the event of clipping. A DC offset in the signal appears as a bias of the higher order bits in the distribution; the bias migrates to less significant bits with a decrease in the variance of the random signal, and the amplitude of the bias increases with the DC offset. The bit histogram of 4096 words telemetered by the array is shown in the right half of Figure 3.2 for 5 channels. The effect of a low amplitude signal (low variance) and negative DC offset in channel 16 (-0.81 V) is manifested as an increase in the occurrence of the high order bits. The distribution in Figure 3.3c simulates channel 16. The higher variance in channel 18 decreases the impact of the DC offset relative to channel 17. These results are corroborated by the time series and time series distribution data. The least significant 4 bits of the 10th channel (H0) in each section were contaminated by noise due to an error in the array software such that the data for H0 was logically OR'ed with the least significant four bits of the previous H8 data. The effect of this noise is shown in the distribution for channel 20. The least significant bits of all array channels also display a peculiar distribution. This is an indication of the switching noise level within the processor as it couples into the ADC and affects the more sensitive lower order bits (4.88 mv resolution). The lowest order bit is consistently affected decreasing the effective resolution of the system.

Power Spectral Density. The spectra illustrates a variety of characteristics of the array coupled with the acoustic noise field. To interpret array system noise, the acoustic noise field components must first be identified. The array is capable of resolving the frequency b. nd between 10 and 220 Hz as discussed in Section II. The spectra shown in Figure 3.4 represent data taken at 4 different times to illustrate the variety of sources which contribute to the low frequency domain; within this band there are two major acoustic ambient noise contributors, ship generated noise and wind generated noise. A typical acoustic spectrum (Figure 3.4a) shows a broad hump due to shipping between 25 and 125 Hz at approximately 75 to 90 dB//μPa/$\sqrt{}$Hz which rolls off to about 70 dB//μPa/$\sqrt{}$Hz at the wind dominated high end of the spectrum. Noise due to array mechanical motion (strum) and biological sources is sometimes seen below 25 Hz. The close passage of a ship imparts tonal components to the low frequency end of the spectrum (Figure 3.4b); a pseudo random coded signal is noticeable at 200 Hz. A seismic profiler operating off the coast of California appears periodically throughout the data set, degrading the

ambient noise measurements above 100 Hz (Figure 3.4c). Ambient noise source identification assists in selecting data which is not dominated by these processes such that system problems may be recognized. The 1 MHz clock switching noise discussed in the previous section is seen in panels d, e and f, where the panel f shows the signal from the hydrophone furthest away from the processor, and the higher frequency levels of this channel increase by 5 dB relative to the other channels, indicating that the system noise is interfering with the ambient noise measurements at the higher frequencies. The system noise is virtually white across the array frequency band (Figure 2.6) and the noise levels shown in Figure 3.4f do not affect the measurements above the 250 Hz level; e.g. channel 20 is capable of measuring acoustic levels above 76 dB//μPa/$\sqrt{Hz}$. High levels are also seen for the closest hydrophones which are due to switching noise within the processor pressure case where the filtering for this signal resides; this noise is reduced with proper shielding. The line frequency harmonics exist at significant but variable levels and are discussed at the end of this section.

Channel to Channel Coherence. Coherence is a measure of the similarity of two signals. The data shown in Figure 3.5a-c is similar to other estimates of the coherence function of ambient noise [Hodgkiss and Fisher, 1987][Urick, 1983]; however in the interest of characterizing array noise, only significant aspects of the coherence data which pertain to array system noise are discussed. These are 1) the high coherence of the line frequency harmonics demonstrating that in spite of the variability in levels, the signals originate from the same source; 2) the notch near 10 Hz as the array filters rolloff and the relative self noise increases; 3) the low frequency peaks which are associated with the array strum and affect the width of the 10 Hz notch which increases with wind speed; and 4) the degradation of the characteristic shape of the elements filtered within the pressure case indicating that substantial incoherent noise is picked up by these channels particularly between 60 and 100 Hz. These particular channels (5 and 6) were chosen for illustration and have substantially higher noise levels than the other channels filtered within the processor case. Spatial correlation of isotropic ambient noise is a sinc function [Cron, Hassell and Keltonic, 1965] where the first zero occurs at $d/\lambda=0.5$ which corresponds to 100 Hz on the array coherence plot. Although the true distribution of ambient noise deviates from the isotropic assumption, the low coherence values at higher frequencies is expected. Therefore the high frequency clock noise discussed above does not affect the ambient noise coherence because at the frequencies of significant coherence, this noise level is below than of ambient noise.

Narrowband Spectral Estimate Across Array. The average spectral estimate of a particular frequency across the array may be used effectively in identifying channels with high noise levels and/or low sensitivity, providing a coarse relative calibration of the channel amplitudes and information concerning the extent of degradation in the ambient noise measurements due to system noise. Figure 3.6 are spectral averages for data received by each channel at 6 specified frequencies. The magnitudes of spectral estimates for one bin of width 0.98 Hz were averaged (n=2583) over a Kaiser-Bessel (α=2.5) windowed time series 21.9 minutes long for each array channel. These linear estimates were averaged, calibrated and plotted in dB re μPa/$\sqrt{Hz}$ reflecting the estimate for each array channel at a specific frequency. The 95% confidence level for the averages is ±0.16 dB. The data were selected carefully avoiding any known nonstationary effects (e.g. seismic profiler, large strum amplitudes, nearby ships). The variation across the array is illustrated in Figure 3.6 for two frequencies within the shipping dominated part of the ambient noise spectrum (35 and 75 Hz), two line frequency harmonics (60 and 120 Hz), and

8

two wind dominated frequencies (135 and 150 Hz). Although the general character of the data within each frequency pair is similar, there is a striking difference between the pairs. The level variation of the line harmonics (3.6d) is clearly shown; the pattern does not reflect any array section commonality. The effect of the coupled switching noise (seen in Figure 3.4f) is evident at the higher frequencies where the acoustic ambient noise levels are lower. Figure 3.6 e and f shows the variability in the 135 and 150 Hz spectral levels across the array as some channels are more susceptible to system noise components than others. A spatial transform across the array shows a broad peak at 0.02667 samples/m which corresponds to a 5 hydrophone spacing. Examination of the high frequency spectral components of each section shows that the two farthest and two closest channels to the processor exhibit a propensity for noise contamination however the levels are affected by the proximity of the wiring to the noise source within the wire bundle and are not predictable.

Spectral Estimate Distribution. The distribution of the power in the individual estimates discussed above provides a basis of confidence in the average level. The distribution (Figure 3.7) was calculated for each of the calibrated estimates with bin widths of 350 μPa/$\sqrt{}$Hz. The figure shows a Rayleigh distribution as expected for the square root of the sum of the squares of two normally distributed components (real and imaginary spectral components). This distribution is used to determine the sensitivity of the average value to outlier estimates. Differences in mean value reflect array calibration variations (channel 32); differences in variance reflect the noise level of the channel. Notice that although the channels filtered within the processor in array section 1 (channels 5 and 6) indicated excessive noise levels on the coherence estimate (Figure 3.5) at 75 Hz and on the single frequency estimate across the array (Figure 3.6c), the same channels in section 3 (channels 35 and 36) shown here do not.

Beampatterns. One way to evaluate the array performance is to investigate the degradation in beampattern as errors are introduced to the amplitude and phase element responses. The amplitude and phase element errors reported in the next section were incorporated into the array beampattern calculation (derived in Appendix B):

$$AF = \sum_{n=0}^{N-1} (A + \delta A_n)e^{j(k(n-\frac{N-1}{2})d(\cos\theta - \cos\theta_i)+\delta\phi_{n}+0.0002(ne)2\pi f)}$$

where A_n is the Kaiser-Bessel (α=1.5) amplitude shading function, δA_n are the amplitude errors, $\cos\theta_i$ is the beam scanning angle, $\delta\phi_n$ represent the random phase errors due to element positional errors as well as electrical phase mismatch, and the last term is the phase sampling error discussed previously with ne — element number and f — frequency in Hz. Since a time shift is the time domain translates into a phase shift in the frequency domain, at a single frequency ω, the correction for this time offset τ=0.2 ms is simulated in terms of a linearly increasing phase delay $e^{+jn\omega\tau}$ for each hydrophone n in a section. The results at 56 Hz are shown in Figure 3.8 for errors in amplitude obtained from the broadband averages, errors in phase from the narrowband calibration and the effect of phase sampling errors which is deterministic and can be removed from the acoustic signal. The beampattern incorporating both amplitude and phase errors (Figure 3.8e) shows a deterioration in side lobe level from the theoretical pattern (Figure 3.8a) and a slight distortion of the main beam. The resulting pattern has virtually constant side lobe levels at about 35 dB below the main beam.

Beam Levels. Directionality plots represent the spatial distribution of the data and

potentially identify relative side lobe levels. The directional beams are calculated by taking a Fourier Transform of the spectral estimates at a single frequency after compensating for the sampling offset discussed above. The plots in Figure 3.9 are the result of computing a linear average, dB average and the standard deviation of the dB estimates [Wagstaff *et al., 1982*] with n = 63 in the presence of a narrowband far field signal. The abscissa is normalized phase ($\frac{\phi}{2\pi} \approx \frac{d}{\lambda}\cos\theta$), with positive phase looking up, and the visible region marked by dotted lines (see Appendix B). A 5 or 6 dB variance is typical of a single transform estimate for a random process [Bendat and Piersol, 1971] and the 2 or 3 dB difference in the averages is caused by the nonlinear logarithm transformation of the Rayleigh distributed spectral time series. Should the beam estimates have significant outliers, the difference between the averages will increase as the linear average weights the outliers more heavily. A strong coherent arrival is indicated by a drop in variance and the coincidence of the two averages as seen in Figure 3.9. The directionality response is a function not only of the array side lobe levels and main beam width but of the noise field with which the array beampattern is convolved. Simulations which assist in the interpretation of the directionality data as measured by this particular array are presented in [Sotirin and Hodgkiss, 1989]. The constant response at $|\phi| > 0.12°$ indicates that both the ambient noise and the array side lobe level are essentially flat. The absence of a decrease in level as the main beam enters invisible space indicates that this level is dominated by the array side lobe response to the signal but does not indicate the relative side lobe level.

Beam Correlation Levels. The correlation beam to beam is an indication of coherent signal arrivals. Because the linear correlation function is normally interpreted in terms of a binormal joint beam distribution, an alternative nonparametric test is performed known as Spearman's rank correlation and has been used successfully by others [Wagstaff *et al., 1982*]. Estimations of the power arriving at 64 specific directions are calculated as described above. If the value of these beam estimations are ordered for any one direction, and the position of the estimation within the ordered set is substituted for the actual value then the distribution of the positions or ranks is uniform provided each estimate is unique. If the estimates are not unique then they are assigned a midposition rank such that the sum of the ranks for any one beam is equal to $\sum_{i=1}^{N} i$ where N is the number of estimates. Once ranked, the correlation coefficient ρ_{jk} for beams j and k is calculated as the linear correlation of the ranks:

$$\rho_{jk} = \frac{\sum_{i=1}^{N}[(r_{ij}-\bar{r}_j)(r_{ik}-\bar{r}_k)]}{\left[\sum_{i=1}^{N}(r_{ij}-\bar{r}_j)^2\sum_{i=1}^{N}(r_{ik}-\bar{r}_k)^2\right]^{\frac{1}{2}}}$$

where r_{ij} and r_{ik} are the assigned ranks for the ith estimation of beam j or k. To verify that a nonzero value of ρ reflects the existence of a statistically significant correlation, the null hypothesis ($\rho_{jk} = 0$) is tested, where a significant correlation is indicated if the hypothesis is rejected. With the function w defined as:

$$w = \frac{1}{2}\ln\left[\frac{1+\rho_{jk}}{1-\rho_{jk}}\right]$$

where w is distributed normally with zero mean and a variance of $\sigma_w^2 = 1/(N-3)$ [Bendat and Piersol, 1971], the null hypothesis of zero correlation is accepted at the α level of significance if

$$-z_p \leq \sqrt{N-3}(w) < z_p \qquad\qquad 3.1$$

where $p = \alpha/2$ and z_p is the p quantile of a standard normal random variable. For display purposes, the correlation matrix M_{jk} consists of 100ρ on and above the main diagonal and $10w/\sigma_w$ below the main diagonal if Equation 3.1 is not satisfied (0 if it is). In general, the results of tests which require a significant amount of data processing are more difficult to interpret in terms of the system noise and are not recommended as independent tests. However, used in conjunction with the other tests these results may support hypotheses. The beam correlation matrix for 120 Hz is displayed in Figure 3.10 at a 95% confidence level. Although this matrix shows significant correlation between the beams, indicated by the grey level below the main diagonal, it is demonstrated below that this is an artifact of the amplitude variability in the signal. Although not an indication of high array side lobe levels which would be the interpretation inferred by others in the absence of a strong multipath acoustic signal, the results do indicate that there is a problem. A typical ambient noise matrix displays few nonzero levels below the main diagonal.

Line Frequency Analysis. The levels of the signals appearing at line frequency harmonics in the *in-situ* are surprisingly strong as the high power input to the array is filtered and the data is digitized in the array itself. The results of self noise tests performed in the laboratory show a conspicuous lack of any consistent 60 Hz harmonics in the spectrum. Although there are spurious peaks throughout the test data set, there were no perpetual signals which would suggest a system (electronic) generated noise source. This implies that the 60 Hz signals and associated harmonics observed in the *in-situ* data set were either acoustic in origin or an artifact of the setup aboard *FLIP*, and were not an inherent component of the array self noise. The acoustic data from the sea test indicated that the 120 Hz line is dominant, appearing mostly broadside (Figure 3.11a) and at high power levels (Figure 3.7d). Acoustic noise propagating from *FLIP* would appear endfire, with a monotonically decreasing level. Spectral levels of vibrational noise within the processor case would decrease as it propagated away from the processor. The 120 Hz signal appears in all array channel spectra at randomly varying levels and although the broadside component is 20 dB above the higher angle arrivals, there appear to be components that arrive at other angles (low variance and significant correlation). The appearance of these arrivals can be explained by examining the Fourier Transform of the channel magnitudes which behaves as an amplitude shading function in the beamformer. The result (Figure 3.11b) illustrates that the 'arrivals' are due to the variability in amplitudes. Not finding a suitable acoustic path for the line frequency harmonics to travel in, this noise must be coupled in through a grounding path in the array when it is deployed from *FLIP* or coupled in from the DC-to-DC converter inputs.

IV. Array Calibration

The array calibration enables one to convert the ADC output recorded on tape to the pressure field seen by the hydrophones. A nominal calibration of a system is obtained from the design specifications of the component parts. For this particular array, the signal path conversion consists of the hydrophone sensitivity at the ambient environmental conditions (-197 dB re V/uPa), the preamplifier gain (40 dB re V), the differential receiver (6 dB re V), the variable gain stage (12 to 60 dB re V), and the ADC (46.23 dB re counts/V). The calibrations addressed here refer to the deviation of the array elements from the nominal calibration. The *in-situ* amplitude calibration was determined from two independent methods. The narrowband calibration consists of comparing monochromatic transmissions, of known

frequency and source levels from a navigated source position, to a predicted response. The broadband method assumes that the average ambient noise levels across the array do not vary significantly from the mean, so defective channels may be identified by examining the variance and a relative calibration is obtained by examining the mean. To minimize the effect of variability in the environment over 1000 ambient noise spectra are normalized and averaged for the broad band estimate, and for the narrow band estimate, the strength of the signal was substantial compared to the noise (SNR of 45 dB//μPa/$\sqrt{Hz}$). The phase calibration was generated by differencing a multiple linear regression with the smoothly varying phase data obtained during the narrow band transmission.

Method Description and Data Collection

Narrowband. The narrowband method depends on modeling the signal arriving at the array by correctly simulating the ocean environment at the test site. The transmission was conducted on Julian day 267 from 2246 GMT until 00 GMT, under benign environmental conditions; wind velocity was 6 to 7 kts at 250 °, swell was 0.5 m at 310 °. A deep conductivity, temperature and depth (CTD) cast (3885 m) was executed coincident with the commencement of the narrow band transmission and this CTD data was desampled for utilization in the sound speed profile calculation [Sotirin and Hildebrand, 1989] required by the models. The water depth obtained by echo sounding from *FLIP* was 4668 meters, therefore the data from the deep CTD was extended by using data from a 4906 meter CTD taken on Julian day 264 at 1605 GMT near 37° 04.10' N and 134° 46.75' S. The ship was allowed to drift during transmissions and source range from *FLIP* (Figure 4.1) was calculated from radar measurements taken every 5 minutes, ship heading and deployment geometry. The source was deployed at a depth of 27 meters, and source level was monitored by a calibrated hydrophone at a range of 1 meter (Table 4.1) as each of the specified frequencies was transmitted for a period of 6 minutes. Array depth was estimated from navigation measurements taken at 1730 GMT. Several propagation models, encompassing normal mode, parabolic equation, fast field and eigenray approaches, were compared using the array test environment parameters to determine the inputs [D'Spain, 1988]. This comparison showed 0.5 to 1.5 dB deviations between the different model spectral level predictions away from transmission loss peaks (Figure 4.2). The models require estimates of ocean bottom parameters such as layer thickness, compressional wave speed and attenuation, shear wave speed and attenuation and density and surface reflection coefficient which were estimated from references in the literature. Small deviations in the predicted transmission loss levels could be due to errors in these estimates. Small variations also occurred in determining the exact location and loss levels associated with the signal null (transmission loss peak) which is sensitive to source range and array receiver depth, changing the phase of the signal arriving across the array. The estimated parameters also affects the phase prediction and was probably responsible for the differences observed in the results, therefore only magnitude predictions will be used. The Generic Sonar Model (eigenray) was chosen as the prediction vehicle due to its robust simplicity in this application where the amplitude is controlled by two dominant paths, consistent results at close range and reasonable execution times. The array data was obtained by extracting the raw data from tape at the same time as the radar fix to obtain as precise a range measurement as possible for the modeling effort. Spectral estimates were calculated and averaged for each channel at the frequencies transmitted during the calibration. The time series, which had to be long enough to generate reasonable confidence limits, was limited to 98 seconds to reduce the errors in range due to ships drift to less than 50 m assuming a drift rate of 1 kt. A single transform estimate was compared to the averaged results at each frequency with slight

12

differences (<0.5 dB) except near the transmission loss peak and at a few isolated channels where the difference was as much as 2 dB for one particular frequency. The 40-50 dB signal to noise ratio was more than adequate to alleviate doubts regarding interfering signals and random noise levels. The comparison between the data and model outputs indicated the necessity of iterating range and source level to match the location of the transmission loss peak and the mean received signal level. The range estimation by ship radar is accurate to within approximately ± 50 m, the range increment in the iteration was 5 m and the final deviation was less than 30 m at 56 Hz and the source level was adjusted by +1.8 dB. The GSM predictions were subtracted from the array received signal at selected frequencies and the element deviations were compared. The data at 56 Hz is shown in Figure 4.3 and results are discussed below.

Broadband. Ambient noise levels are reported to vary only slightly (e.g. 1 dB) with depth [Morris] therefore incoherently averaging the ambient noise measured during the sea test should yield a virtually constant level across the array. If this is the case, then deviation from this level offers an independent amplitude calibration. Figure 4.4 a, b, d and e are spectral averages and the standard deviation of the spectral estimates for data received by each channel at a specified frequency for 4 different time periods. The averages are calculated from linear estimates (middle trace) and dB estimates (bottom trace), and the standard deviation is based on the dB estimates offset to 90 dB for display purposes (top flat trace). The magnitudes of spectral estimates are calculated as described in Section III. The linear estimates were averaged, calibrated and plotted in dB re μPa/$\sqrt{Hz}$ reflecting the estimate for each array channel at a specific frequency. The lower trace was calculated by converting the linear estimates to dB, then averaging and plotting the calibrated results. The standard deviations were calculated from the calibrated dB estimates. The standard deviation of the log values has been shown to be a constant value of 5.6 dB [Dyer, 1970] (displayed as 95.6 on the plot); the 95% confidence level for the averages is +0.166 dB, -0.162 dB for 2583*2 (real and imaginary estimates) degrees of freedom. The data were selected carefully avoiding any known nonstationary effects (e.g. seismic profiler, large strum amplitudes, nearby ships) with the expectation that the spectral level would vary smoothly across the array on the order of 1 dB, deviating only at the level of channel calibration.

Phase. The phase results presented below were the result of a single coherent FFT as described above. The raw phase data was processed by: (a) unwrapping the inherent 2π rollover, (b) accounting for the 0.2 ms/element/section sampling error in the array by subtracting $\omega n\tau$ where n is the channel position described in Section I, (c) correcting for the 180° phase shift at the transmission loss peak as a result of the interference between the direct and surface reflected paths arriving at the array, and (d) subtracting a multiple linear regression curve to realize the plots in Figure 4.5.

Results.

Magnitude. Limitations in the calibration methods due to the incomplete knowledge of environmental parameters and the temporal variability of ambient noise were minimized. The modeling efforts of the narrowband transmissions resulted in 0.5 to 1.5 dB variations between various models and required iteration in source level and range. The mismatch in Figure 4.3a especially apparent at either end of the array results in a spatially varying offset. Consequently, the absolute calibration levels (Figure 4.3b) were interpreted relative to the offset trend, and the modeling results were confined to an advisory position in terms of the smoothness of the array response. The response shown at 56 Hz reveals a smooth variation across the array and the measured values plotted on an expanded scale (Appendix C) expose channel deviants more clearly. Relative deviation levels greater than 1 dB

13

from the smooth response were empirically identified and recorded at specified frequencies. These results were reviewed for consistency and the average results tabulated (Table 4.2). The ambient noise collected every 7.5 m for 18 days, varies smoothly with depth on a large scale. The small scale deviations however, are on the order of ±1.5 dB. The variation across the array is illustrated in Figure 4.4 for 75 Hz at 4 different times (a, b, c and d) where the time difference between the averages is about 1 hour for the vertical panels (a-b and c-d), and 2 days for the horizontal panels (a-c and b-d). The degree of channel to channel variability increased during the 2 day period. This variation in time is seen by examining the bottom panels (e and f). A multiple linear regression was subtracted from the linear averages to estimate the relative channel variation. The top plot in panels e and f represent the difference in relative channel variation between the two panels directly above and the difference in relative channel variation between the 2 day estimates in the bottom plot. Short term (1 hour) time variation is small, only one channel has more than a ± 1 dB variation. The variance across the channels is 0.13 dB (e) and 0.095 dB (f); because the channel calibration should remain constant, these differences represent changes in the ambient noise field. Long term (2 days) time variation is larger, with more than 10% of the channels having deviations of greater than ± 1 dB. The variance across the channels is 0.68 dB (e) and 0.78 dB (f) increasing from the 2 hour variance due to the nonstationarity of the noise field. It is this variability in the ambient noise field which limits the broadband calibration. To minimize the effects, estimates of the ambient noise field were calculated at 15 different times during the experiment in hopes that the variations were random and would average out, leaving a more accurate estimate of the channel calibration levels. The standard deviation of the 15 time estimates (Figure 4.6a for 56 Hz) for the 3 frequencies processed exhibit 3 channels with consistently high variance (21, 55 and 100). The broadband amplitude results for 56 Hz, illustrated in Figure 4.6b, were compared to the narrowband calibration results at 56 Hz shown in Figure 4.3b. Ignoring channels 40 to 60 in the narrowband calibration which are close to the interference peak at 56 Hz and the channels with high variance, the comparison shows that most channels deviations of more than 1 dB are noticeable in both results, however there are some obvious differences. These differences, notably channels 5, 6, 29, 30, 65 and perhaps 85 are a result of excessive system noise levels. The ambient noise measurements for these channels are distorted even at low frequencies. These channels do not exhibit a high variance at a specified frequency due to the consistency of the level; the level of channel 30 in Figure 3.6 is 88 dB re $\mu Pa/\sqrt{Hz}$ at frequencies other than line harmonics. This imposes a frequency dependent calibration as the ambient noise level changes with frequency. Another obvious difference is the channel 27 estimate which is consistently high in the narrowband results but is not identified as a deviant in the ambient noise results. The cause of the apparent transient nature in a few of the channel levels has not been resolved.

Phase. The phase regression differences were examined for 5 different frequencies, the result for 56 Hz is shown in Figure 4.5f. Besides channel 100, the only other identifiable error mode were the channels which are filtered within the processor case (e.g. 5, 6, 15, 16). These channels are most likely affected by the switching noise identified in the previous section. The phase of the incoming signal should vary smoothly across the array (Appendix C); ignoring the mismatch in the regression curve and the transmission loss peak, the deviation in phase at 56 Hz is within 0.1π radians. The smooth phase variation assisted in identifying the channels with reversed polarity discussed previously. Phase deviations are also evident in the time series plots (e.g. Figure 3.1) during an impulsive arrival. The deviations for acoustic arrivals such as the seismic profiler are small as discussed above however for mechanical vibration (strum), every fifth channel per section (e.g.

14

5, 15, 25, etc) is delayed on the order of 50 ms due to propagation interference by the processor pressure case.

V. Conclusion

Large aperture low frequency arrays are inherently difficult to test because of the physical size and number of channels which impose time and facility constraints. Utilizing ambient noise in system tests allows the array performance to be monitored throughout the experiment, identifying low performance channels and their effect on experimental results. The tests discussed here, although not exhaustive and yet to some extent repetitive, illuminate problems associated with the array hardware and software. The repetitive aspect of the tests is necessary due to the random nature of the ambient noise and the specific manifestation of the problem being investigated. In addition to system noise testimony, *in-situ* data was successfully used to calibrate the individual channels. A combination of narrowband transmissions and ambient noise measurements provides magnitude deviations to within ±1 dB.

Although the tests amplify the negative aspects of the array system, based on the results shown here, the array might well be used without adjustments to the nominal calibration. The -35 dB array side lobe level is more than adequate for many applications. However, spectral levels for individual channels are frequency limited due to system noise. Specific results for the array discussed show that four elements in each array section (the closest to and furthest from the processor) potentially have noise problems at high frequencies. The noise in the furthest elements is coherent and with the exception of channel 30 (consistently above 85 dB in the data processed to date) and channel 29 (slightly lower), the average level is about 78 dB//μPa/$\sqrt{}$Hz but affects few enough channels that the degradation in the directionality plots is minimal. The noise in the closest elements is incoherent but at about the same levels with the exception of channels 5 and 6 which exhibit a frequency dependence when compared to spectra from other channels. The distinct comb-like pattern fades as the amplitude of the ambient noise increases. The high frequency contamination was identified during the self noise laboratory test as a common mode problem in the channels furthest from the processor. The system noise in the channels filtered within the processor case was not identified because the electronic packages were removed from the case and separated physically to provide access to test points reducing the coupling effect. Precursory laboratory system tests are required to eliminate system noise sources prior to deployment. The coherence shown is channels 5 and 6 indicates substantially higher noise levels than most of the other channels, and although not shown, this is corroborated by their spectral estimate distribution. Few channels show this level of noise contamination however, and it is not expected to affect coherent processing results. This is supported by the -35 dB side lobe levels in the array beampattern. Few of the tests would individually provide conclusive evidence of a system noise problem due to the stochastic nature of ambient noise and the particular manifestation of a specific system problem. However, as evidence is accumulated through the results of the series of tests, these problems may not only be identified but cause may be narrowed. The impact on experimental results is of course tied to the specific purpose of the experiment. For the results shown here, absolute spectral levels for ambient noise are obviously damaged for specific channels and specific frequency bands, however the array is capable of measuring signals above the system noise levels defined by the test results, and the directionality estimates would satisfy most application specifications.

An *in-situ* array calibration was demonstrated successfully at a ±1 dB re μPa/$\sqrt{}$Hz level by comparing the results of the two independent methods for

relative channel to channel information. Although the narrowband results have the potential of providing absolute calibration values, modeling the narrowband transmission requires precise knowledge of environmental parameters. Some of this information is not readily available for specific test sites and must be estimated, increasing the error of the modeled response. Consequently the model outputs were utilized as an indication of the smoothness of the array response at specified frequencies. The level of system noise and the temporal variation of the ambient noise levels posed problems during the broadband array calibration which examines channel variation after averaging large numbers of spectra. Deviation from a regression across the array removes the time-varying mean of the ambient noise and allows comparison of channel to channel variation. The variance of the estimates must also be considered as confidence in the mean deviation increases. Comparing broadband calibration results to the narrowband results yields good agreement however, with the exception of the channels with excessive system noise levels. Being aware of the potential for deviation between the two methods facilitates the analysis. Phase calibration results were based on the assumption of smooth phase variation across the array and were identified as deviations from a multiple linear regression. The deviation in phase was small (0.1π at 56 Hz) with the exception of those channels identified with system noise degradation.

Acknowledgments

Appendix A Element and Processor Identification.

Element Identification. Identification of the hydrophone elements varies with the associated stage of array fabrication. Table A1 illustrates the ID cross-reference for the vertical deployment during the VLA1 experiment in September 1987. The first column results from the 'at sea' configuration recorded on magnetic tape, the second column refers to the laboratory array test setup, the third column is the identification scheme used during hose fabrication and testing, and the fourth column lists individual element numbers. *Channel* numbers represent the order in which the data was recorded on magnetic tape throughout the experiment. The channels are numbered from the bottom or physically deepest phone (# 1) to the top phone (# 120) which was closest to *FLIP*, the phase-reversed channels are indicated. The *ID* is referenced to a particular processor. P_1 is the deepest processor which collects data from 5 phones below it (channels 1-5) and 5 phones above (channels 6-10). The H designation refers to the acquisition timing. The data from each 10 channel P-section are stored as equally spaced time multiplexed samples, starting with H0. The clocks are resynchronized every 2 ms with a pulse generated in the array telemetry module. This results in a phase shift of $\omega n r$ where ω is the frequency, n is the channel position Hn, and r is the 0.2 ms sample frequency. The effect of this phase shift on the beampattern is significant as frequency increases (Figure 3.8c). The *nose* designation identifies which physical hydrophone hose section was being sampled. The hose sections are identical facilitating construction, testing and maintenance, and were tested individually in the laboratory prior to array installation. The lab test results are summarized in the last three columns; *100 Hz level* is the amplified output of the differentially received line driver in dB referenced to the signal injected electronically at the hydrophone, *low and high -3 dB* are the frequency cutoff points in Hz. The *phoneid* identifies the individual phones prior to installation within the hose section.

Processor Identification. The processors are identified with a software ID and a hardware ID (Table A2). The software ID reflects the physical position the processor claims within the array and is programmed as such in the EPROM. Each processor transmits the data sampled during a 2 ms frame within a time window dictated by its software ID. This ID may be reprogrammed by the operator and will have the effect of changing the position of data transmission window for the specified processor. The hardware ID is hardwired for each individual processor, providing a fixed ID reference. The bit stream location refers to the processor data location within a 2 ms frame of data. The contents of the 8 locations assigned to each processor varies with the commands the processor receives [Sotirin and Hildebrand, 1988].

Table A1a. Element Identification - September 1987

channel	ID	hose	phoneid	100Hz level	low3db Hz	high3db Hz
1	P1H9	20B5	196	-1.2	6.4	214
2	P1H8	20B4	197	+0.7	4.0	220
3	P1H7	20B3	198	-1.2	5.8	216
4	P1H6	20B2	199	-0.7	5.1	221
5 (-)	P1H5	20B1	200	-0.1	4.6	15.0 k
6 (-)	P1H4	12A1	111	+0.3	3.9	14.6 k
7	P1H3	12A2	112	+0.2	4.7	226
8	P1H2	12A3	113	+0.1	5.2	217
9	P1H1	12A4	114	+0.2	4.5	225
10	P1H0	12A5	115	+0.4	4.6	232
11	P2H9	12B5	116	+0.1	4.4	212
12	P2H8	12B4	117	0	4.8	240
13	P2H7	12B3	118	+0.1	4.4	211
14	P2H6	12B2	119	-0.1	4.8	204
15	P2H5	12B1	120	-1.2	5.1	15.2 k
16 (-)	P2H4	19A1	181	-0.4	6.1	14.7 k
17	P2H3	19A2	182	+0.1	4.6	217
18	P2H2	19A3	183	+0.2	4.9	223
19	P2H1	19A4	184	-0.8	5.5	220
20	P2H0	19A5	185	-0.6	6.3	221
21 (-)	P3H9	19B5	186	-0.3	4.5	230
22 (-)	P3H8	19B4	187	-0.5	4.7	223
23	P3H7	19B3	188	-0.6	5.3	217
24	P3H6	19B2	189	-0.8	5.3	218
25 (-)	P3H5	19B1	190	-0.6	4.7	15.3 k
26	P3H4	16A1	151	-1.1	5.2	15.0 k
27	P3H3	16A2	152	-0.6	4.7	220
28	P3H2	16A3	153	-0.4	4.8	211
29	P3H1	16A4	154	+0.3	4.6	230
30	P3H0	16A5	155	+0.4	4.4	229
31	P4H9	16B5	156	0	5.0	225
32	P4H8	16B4	157	+0.1	4.7	224
33	P4H7	16B3	158	0	4.9	223
34	P4H6	16B2	159	-0.7	5.5	218
35 (-)	P4H5	16B1	160	-0.7	6.0	14.1 k
36 (-)	P4H4	11A1	101	-0.5	5.0	14.3 k
37	P4H3	11A2	102	-0.5	5.0	220
38	P4H2	11A3	103	-0.7	4.6	217
39	P4H1	11A4	104	0	4.3	227
40	P4H0	11A5	105	0	4.9	225
41	P5H9	11B5	106	+0.3	4.5	231
42	P5H8	11B4	107	+0.1	4.5	220
43	P5H7	11B3	108	-0.4	4.8	220
44 (-)	P5H6	11B2	109	+0.1	4.8	223
45 (-)	P5H5	11B1	110	-0.2	4.3	14.6 k
46 (-)	P5H4	7A1	61	-0.3	4.2	15.3 k
47	P5H3	7A2	62	-0.3	4.7	216
48	P5H2	7A3	63	-0.3	4.2	218
49	P5H1	7A4	64	+0.3	4.6	222
50	P5H0	7A5	65	-0.3	4.0	214
51 (-)	P6H9	7B5	66	-0.4	5.0	211
52	P6H8	7B4	67	+0.2	4.7	214
53	P6H7	7B3	68	-0.3	5.8	217
54	P6H6	7B2	69	0	4.1	216
55 (-)	P6H5	7B1	70	-0.3	4.7	15.2 k
56 (-)	P6H4	5A1	41	-0.3	4.4	14.2 k
57	P6H3	5A2	42	+0.5	4.0	220
58	P6H2	5A3	43	-0.1	4.8	220
59	P6H1	5A4	44	0	3.8	210
60	P6H0	5A5	45	0	4.5	225

18

Table A1b. Element Identification - September 1987						
channel	ID	hose	phoneid	100Hz level	low3db Hz	high3db Hz
61	P7H9	5B5	46	0	4.8	222
62	P7H8	5B4	47	+0.3	4.4	223
63	P7H7	5B3	48	-0.2	5.0	226
64 (-)	P7H6	5B2	49	+0.1	4.0	226
65	P7H5	5B1	50	-0.4	4.2	15.2 k
66 (-)	P7H4	2A1	0	-0.6	4.7	14.5 k
67 (-)	P7H3	2A2	0	-0.6	5.9	228
68	P7H2	2A3	13	0	3.7	230
69 (-)	P7H1	2A4	0	-0.6	3.7	201
70 (-)	P7H0	2A5	0	-0.1	4.9	217
71 (-)	P8H9	2B5	0	-0.4	6.0	219
72 (-)	P8H8	2B4	17	-0.5	4.6	205
73 (-)	P8H7	2B3	0	+0.4	4.3	235
74	P8H6	2B2	212	-0.2	4.6	228
75 (-)	P8H5	2B1	0	0	5.8	14.8 k
76 (-)	P8H4	13A1	121	-0.3	5.1	14.9 k
77 (-)	P8H3	13A2	122	-0.7	5.1	210
78	P8H2	13A3	123	-0.8	5.3	218
79	P8H1	13A4	124	-0.8	5.6	219
80	P8H0	13A5	125	-0.7	5.7	212
81	P9H9	13B5	126	-0.4	4.8	225
82	P9H8	13B4	127	+0.5	4.8	219
83	P9H7	13B3	128	+0.5	4.6	230
84	P9H6	13B2	129	-0.8	5.4	212
85 (-)	P9H5	13B1	130	-0.5	5.1	14.8 k
86 (-)	P9H4	17A1	161	-0.6	5.6	13.9 k
87	P9H3	17A2	162	-0.6	5.0	215
88	P9H2	17A3	163	-0.4	5.0	211
89	P9H1	17A4	164	-0.5	4.9	214
90	P9H0	17A5	165	-0.5	4.9	217
91	P10H9	17B5	166	-0.7	5.2	217
92	P10H8	17B4	167	-0.6	5.0	224
93	P10H7	17B3	168	-0.7	5.1	223
94	P10H6	17B2	169	+0.7	4.1	226
95 (-)	P10H5	17B1	170	-0.6	4.6	14.26 k
96 (-)	P10H4	14A1	131	-0.4	4.3	14.8 k
97	P10H3	14A2	132	+0.7	4.4	232
98	P10H2	14A3	133	-0.7	5.3	216
99	P10H1	14A4	134	+0.2	4.6	226
100	P10H0	14A5	135	-0.1	4.9	220
101	P11H9	14B5	136	-0.5	4.9	227
102	P11H8	14B4	137	-0.3	5.1	220
103	P11H7	14B3	138	-0.1	4.6	218
104	P11H6	14B2	139	+0.4	4.4	240
105 (-)	P11H5	14B1	140	0	4.5	15.5 k
106 (-)	P11H4	4A1	31	-0.3	5.0	15.8 k
107	P11H3	4A2	32	+0.4	4.5	230
108	P11H2	4A3	33	0	4.4	234
109	P11H1	4A4	34	-0.1	4.9	223
110	P11H0	4A5	35	-0.1	4.8	231
111	P12H9	4B5	36	+0.2	4.6	225
112	P12H8	4B4	37	+0.3	4.0	231
113	P12H7	4B3	38	-0.3	4.2	219
114	P12H6	4B2	39	0	4.7	223
115 (-)	P12H5	4B1	40	-0.5	5.0	15.6 k
116 (-)	P12H4	21A1	201	-0.6	8.2	15.6 k
117	P12H3	21A2	202	-0.5	5.1	222
118 (-)	P12H2	21A3	203	+0.2	4.5	226
119	P12H1	21A4	204	-0.6	6.5	211
120	P12H0	21A5	205	-1.1	6.2	215

Hose #	Processor SWID	Processor HWID	Bit Stream Location
	*** *FLIP* ***		
	Adaptor		-----
21B			
21A	12	6	91-98
4B			
4A	11	14	83-90
14B			
14A	10	13	75-82
17B			
17A	9	11	67-74
13B			
13A	8	15	59-66
2B			
2A	7	7	51-58
5B			
5A	6	10	43-50
7B			
7A	5	16	35-42
11B			
11A	4	12	27-34
16B			
16A	3	3	19-26
19B			
19A	2	C	11-18
12B			
12A	1	8	3 - 10
20B			
20A			
	Terminator		

Table A2. Processor Identification - September 1987

Appendix B Array Beampattern.

The directional characteristics of the array may be used as an indicator of the robustness of coherent processing schemes when confronted with random errors in amplitude shading and phase response. The expressions are also useful in evaluating the effect of modifying array design parameters eg. number of elements and element separation. Generation of the beampatterns the array described in Section 1 follows a similar development to that described by Stutzman and Thiele [1981]. The array is an equally spaced linear array with 10 elements per section and 12 section per array.

The hydrophone response is omnidirectional and is designated as $A_0 = A_1 = ...A_N$ where N is the number of elements. A beampattern in terms of angle of arrival θ is calculated by summing the phase corrected response for each element to an incoming plane wave; this pattern is referred to an the array factor when it is expressed in terms of phase angle ϕ described below. The phase of the incoming wave arriving at the middle of the array is arbitrarily set to zero. The phase of the incoming wave arriving at the element just below the middle is delayed by a factor which is proportional to the distance traveled by the wave $\frac{(1/2)d\cos\theta}{\lambda} = \frac{\phi}{2\pi}$ such that for this element $\phi = \frac{2\pi(d/2)\cos\theta}{\lambda}$, where d is the distance between elements in meters, λ is the wavelength of the incoming wave, and θ is the angle of arrival of the incoming wave where a wave arriving normal to the array has an angle of arrival of $\frac{\pi}{2}$ radians. The phase of the incoming wave arriving at subsequent array elements is calculated similarly thus:

$$AF = \sum_{n=0}^{N-1} A_n e^{jk(n - \frac{N-1}{2})d\cos\theta}$$

where k = wavenumber = $\frac{2\pi}{\lambda}$ and the index n is initialized to 0 at the top element of the array. By assuming that the amplitude response is identical for each element, the array factor may be written in closed form which permits evaluation of specific beampattern parameters by inspection. With ϕ defined as $\phi = kd\cos\theta$ and by assuming that the element amplitude response is equal to A, the array factor becomes,

$$AF = Ae^{-j\frac{N-1}{2}\phi} \sum_{n=0}^{N-1} e^{jn\phi}$$

Although the above equation could be evaluated using Fourier series in terms of ϕ, the beampattern is normally plotted in terms of θ, the angle of arrival. Rewriting the summation in closed form and manipulating,

$$AF = Ae^{-j\frac{N-1}{2}\phi} \frac{1 - e^{jN\phi}}{1 - e^{j\phi}} = Ae^{-j\frac{N-1}{2}\phi}\left[\frac{e^{jN\phi/2}}{e^{j\phi/2}} \frac{e^{jN\phi/2} - e^{-jN\phi/2}}{e^{j\phi/2} - e^{-j\phi/2}}\right]$$

$$= Ae^{-j\frac{N-1}{2}\phi}\left[e^{j\frac{(N-1)\phi}{2}} \frac{\sin(\frac{N\phi}{2})}{\sin(\frac{\phi}{2})}\right]$$

The array factor may be normalized by the maximum response $A \sum_{n=0}^{N-1} 1 = AN$ at $\phi=0$ resulting in an expression which is symmetric about π:

$$AF_{normalized}= f(\phi)= \frac{sin(N\phi/2)}{Nsin(\phi/2)} = \frac{sin((Nkd\cos\theta)/2)}{N \; sin((kd\cos\theta)/2)}.$$

The main beam width and number and location of the sidelobes are easily evaluated from the closed form notation. The width of the main lobe may be measured by the position of the first zero crossing which occurs when $sin(N\phi/2) = 0$. or $\phi = 2\pi/N$. This occurs at $\theta = \arccos(\frac{\lambda}{Nd})$. A rule-of-thumb, using a small angle approximation, is that the mainlobe width $= 2 * (\pi/4 - \theta) = 2 * \arcsin(\lambda/\Gamma) = 2\lambda/\Gamma$, where Γ is the array aperture Nd, and to half power is $0.886\lambda/\Gamma$. For the array at 100 Hz, $\lambda = 15$ meters, $d = 7.5$ meters, $N = 120$ and the first zero crossing occurs at $\phi = \pm \pi/60$ or $\theta = \pi/2 \pm 0.0053\pi$ yielding a main beam width measured at the zero crossings of 1.9° which corresponds to a half-power beamwidth of less than 1°. Subsequent zero crossings define the widths of the sidelobes and occur at $\phi_i = \frac{i2\pi}{N}$. This indicates that for one period of $f(\phi)$ there are N-2 sidelobes plus one mainlobe, that the width of each sidelobe is $2\pi/N$, and that the width of the mainlobe is twice that or π/N. The array factor response pattern of an equally spaced linear array is independent of the incoming wave frequency and of the element spacing. It is dependent only on the number of elements in the array N. The beampattern is not however, and in terms of θ, further inspection indicates that as the aperture Nd increases (this parameter may increase with the inter-element spacing or with the number of elements) or the frequency increases the number of sidelobes increases, the width of the sidelobes decreases, and the width of the mainlobe decreases. The mainlobe can be thought of as a spatial sampling instrument whose bandwidth is $2\lambda/\Gamma$. The finest angular resolution of the noise field that can be achieved then is related to the array aperture size in terms of the mainlobe width. This angular resolution, termed the critical angle [Bracewell, 1954], is half the mainlobe width or $\theta_c = \lambda/\Gamma$.

The beampattern of a vertical linear array is a function of elevation angle θ but not of the azimuthal angle. Thus the beampattern exhibits cylindrical symmetry about the line of the array, and it is completely determined for $0 < \theta < \pi$ or $-1 < \cos \theta < 1$. This region, known as the visible region, is described in terms of ϕ as $-kd < \phi < kd$. Interpretation of directional data is facilitated with an intuitive understanding of the mapping between electrical phase ϕ and physical phase θ. If the element response is linearly phase-shifted electronically to redirect the pattern in space, the phase-shift factor α is additive redefining the visible region as $\alpha - kd < \phi < \alpha + kd$. The array described was cut for a $\lambda/2$ spacing at 100 Hz of 7.5 meters between elements. Therefore at 100 Hz, exactly one period of the array factor appears within the visible region. At 50 Hz, only half a period is visible; in terms of steering the main beam as shown in Figure 3.7, as ϕ is increased beyond the visible region, the main beam disappears and only the side lobes of the array remain directed toward real space. Consequently, if the level is dominated by the side lobe response, the main beam's disappearance will have little effect. Increasing the frequency to 200 Hz, two periods are visible giving rise to the grading lobes, which are at the same magnitude as the main beam, at 0 and 180 degrees for a broadside beam. These grading lobes restrict the ability of the array to discriminate between signals arriving at different angles.

Appendix C Narrowband Calibration Results.

The array measurements of the narrowband transmissions during the *in-situ* calibration are presented for 16, 22, 27, 41, 56, 81, 98, 135 and 159 Hz. The channels identified during the analysis are circled. The GSM output and a normal mode propagation model prediction (ATLAS) for the same frequencies are also shown to give an indication of the smoothness of the response. Two model predictions are shown for comparison and to indicate the relative sensitivity to environmental parameters (especially bottom parameters). The high frequency oscillations in the GSM response at 159 Hz are due to the bottom reflection arriving almost endfire with respect to the array with a wavelength of 9.4 m. These outputs are not intended to be utilized in an absolute calibration. The phase response for 27, 56 and 81 Hz is shown on an expanded scale as deviations from a linear regression. The channels with the highest phase variability are those filtered within the processor case.

Narrowband Calibration: 16 Hz
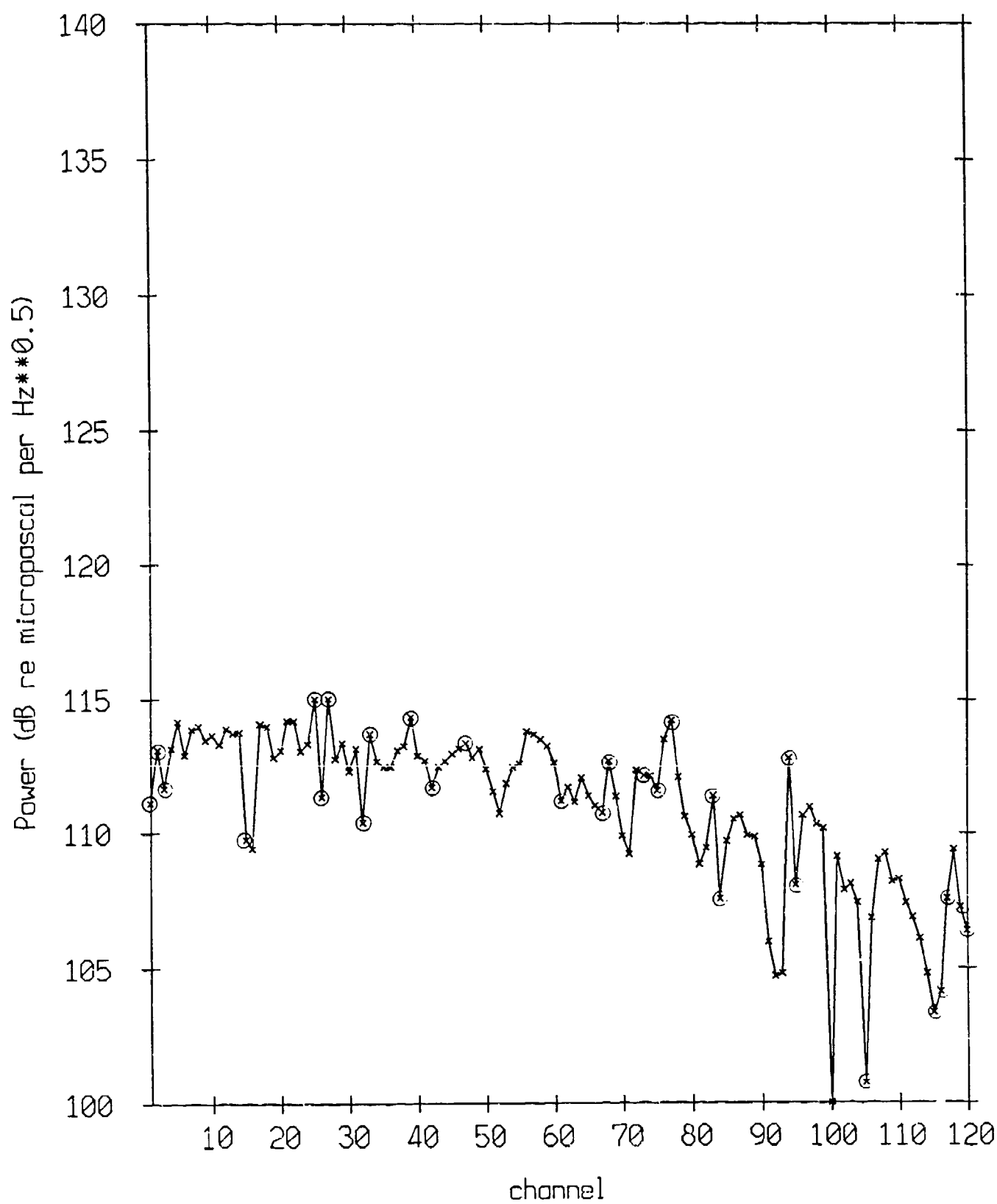
Narrowband Calibration: 22 Hz
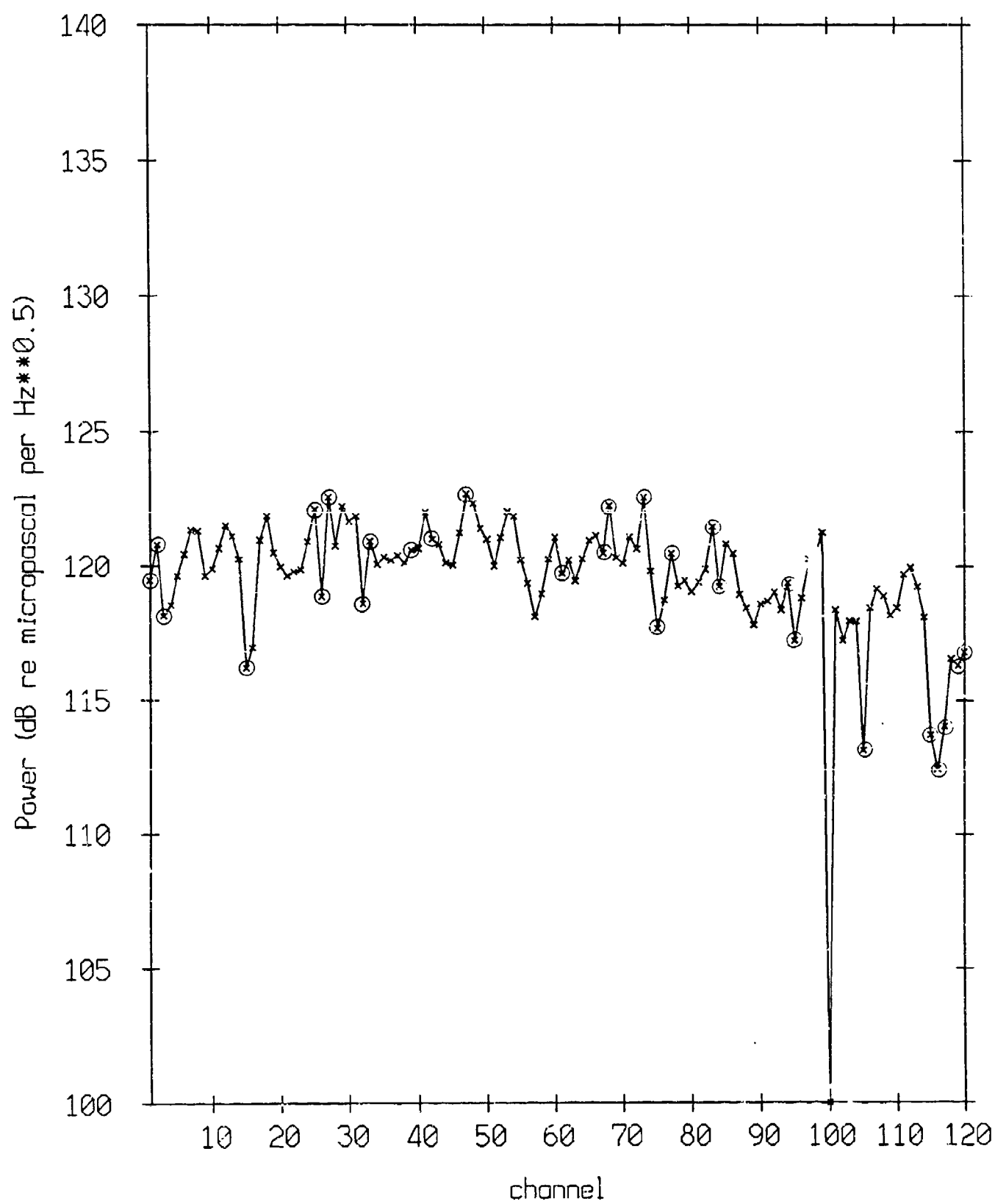
Narrowband Calibration: 27 Hz
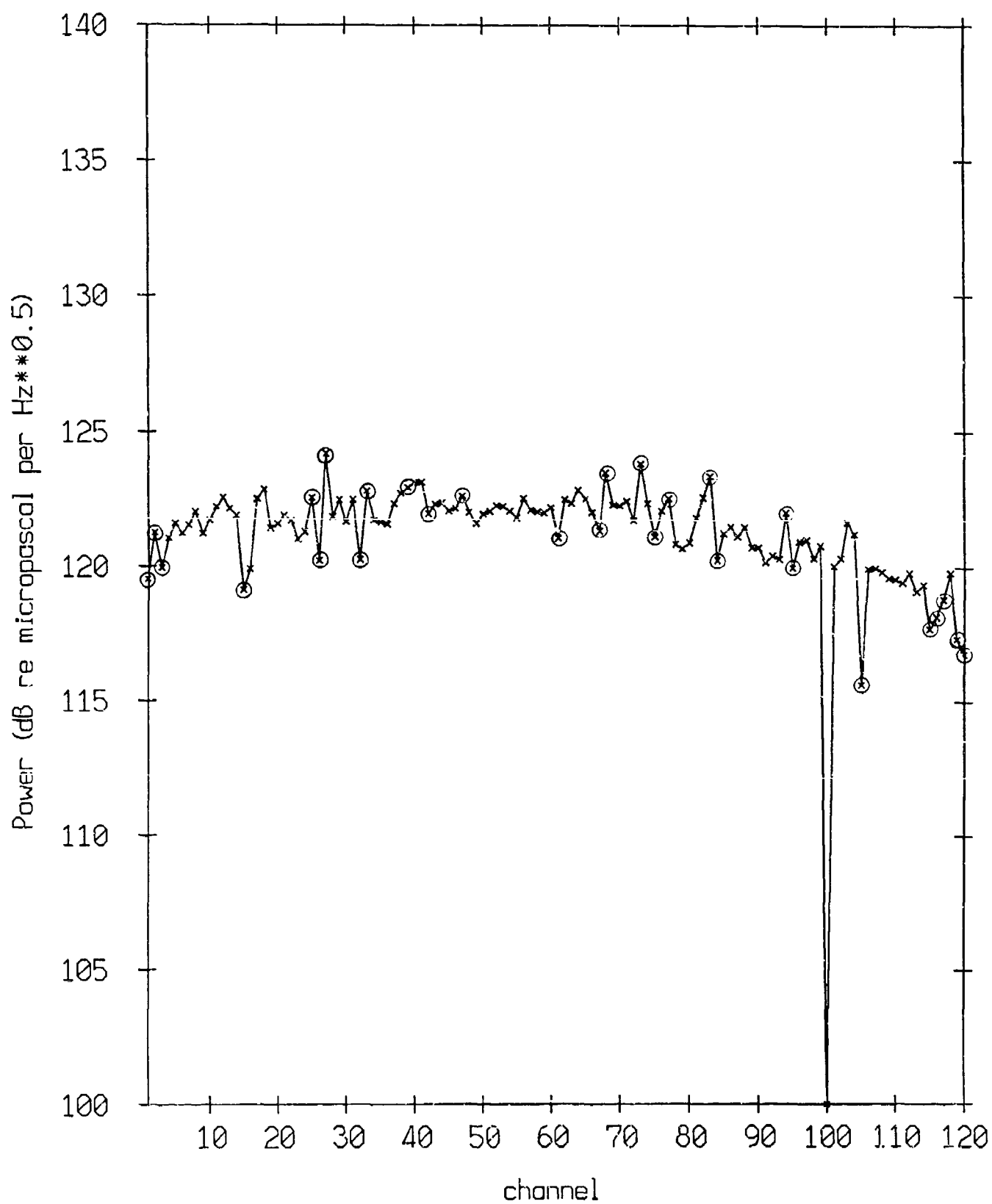
Narrowband Calibration: 41 Hz
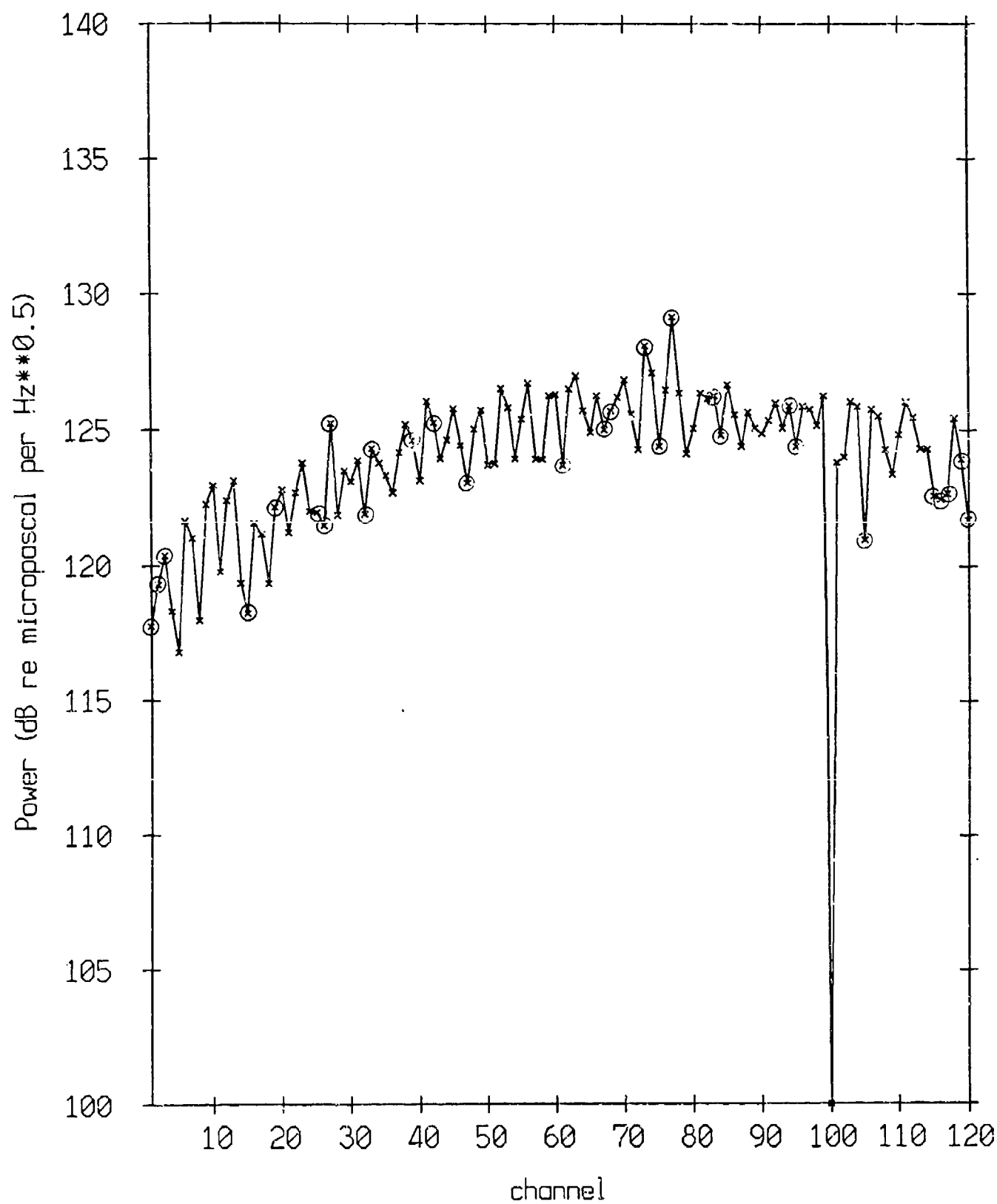
Narrowband Calibration: 56 Hz
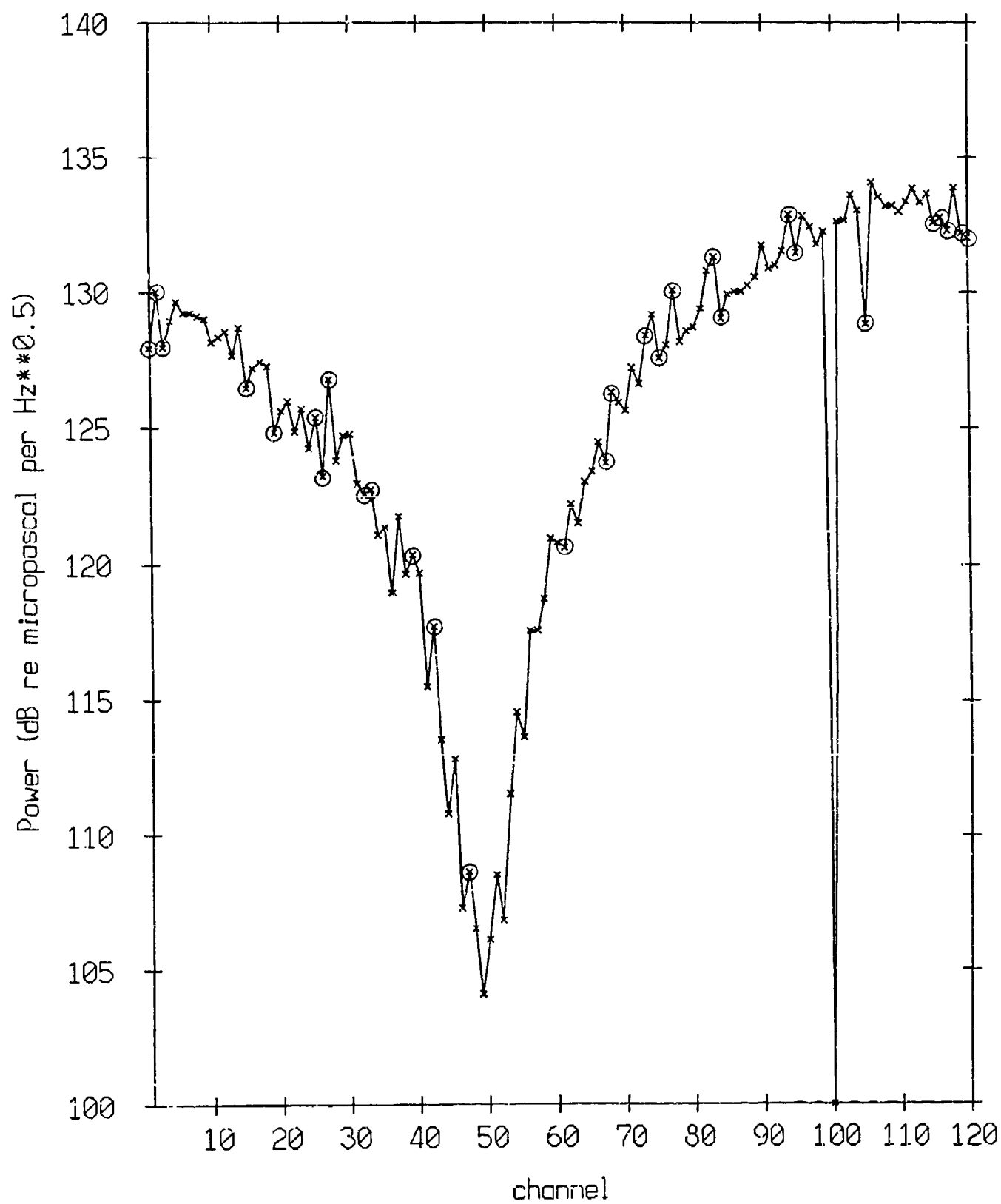
Narrowband Calibration: 81 Hz
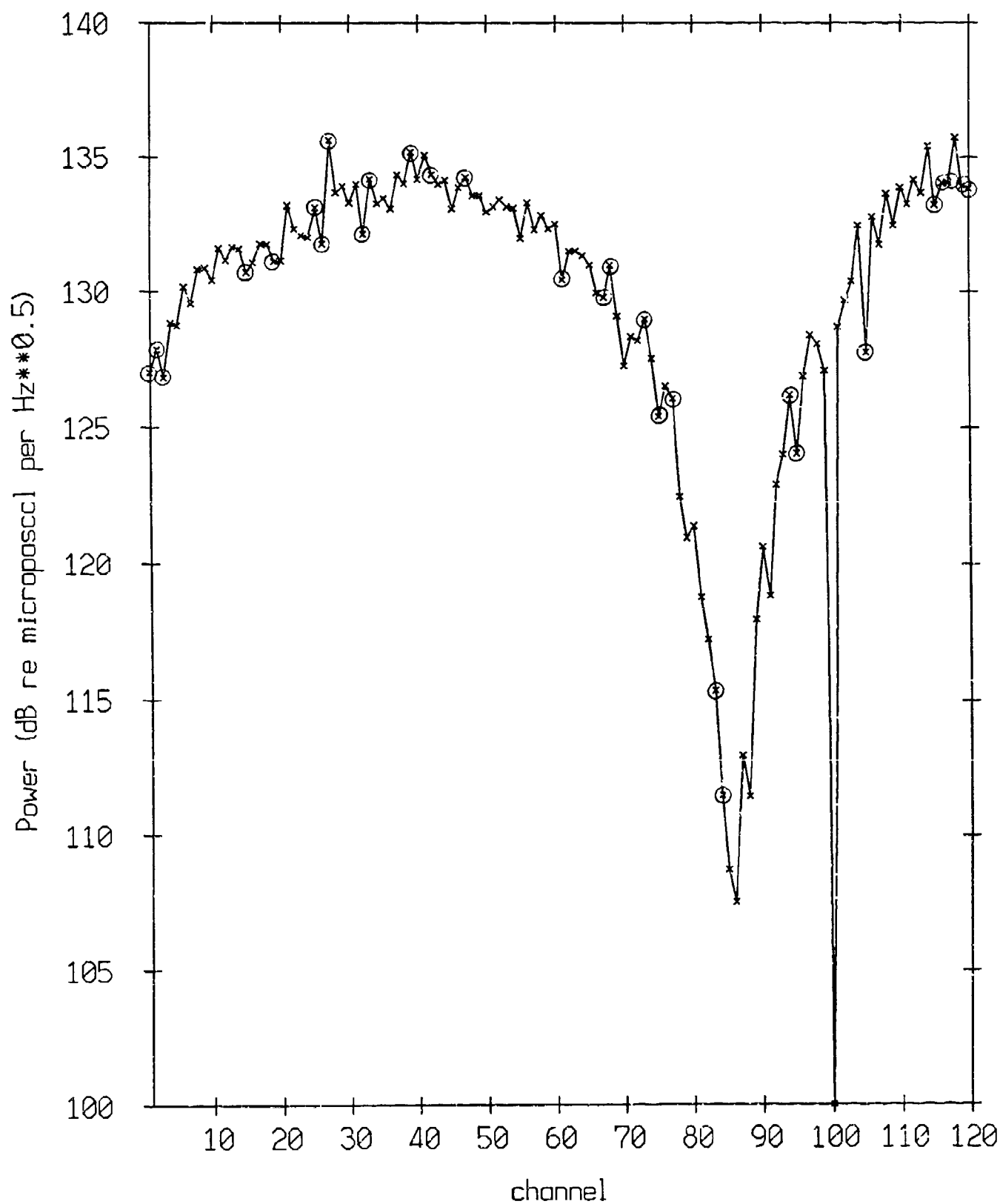
Narrowband Calibration: 98 Hz
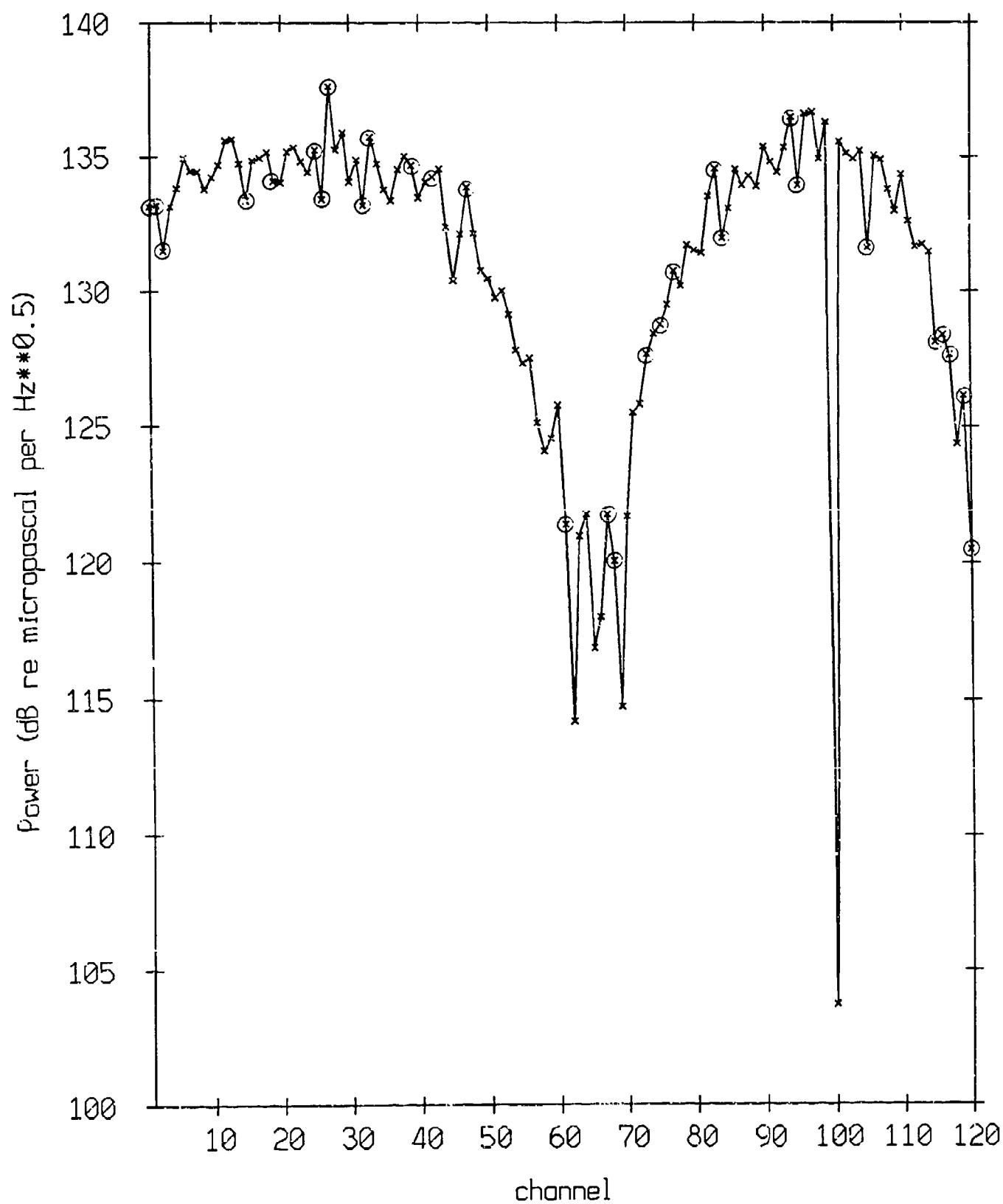
Narrowband Calibration: 115 Hz
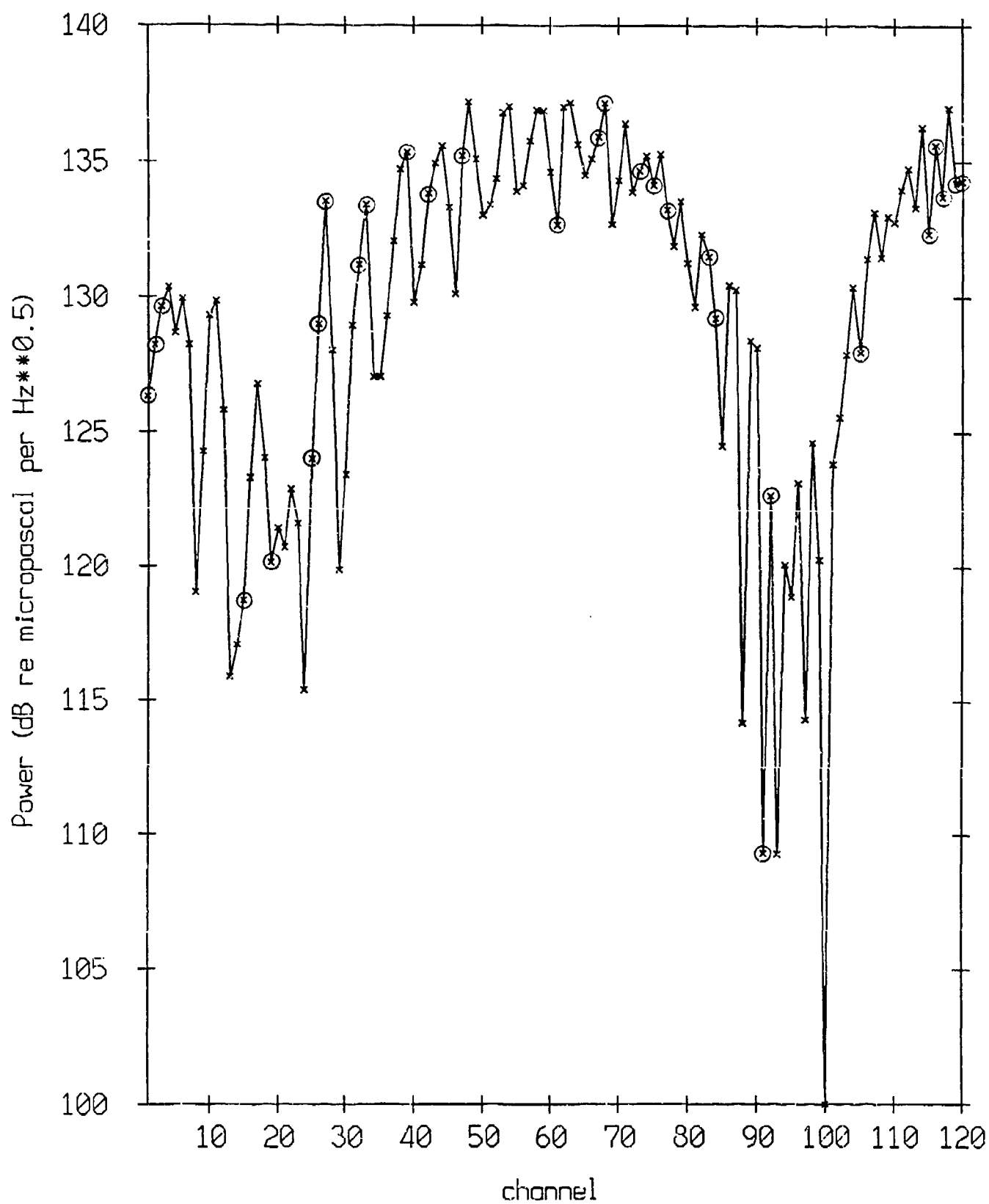
Narrowband Calibration: 135 Hz
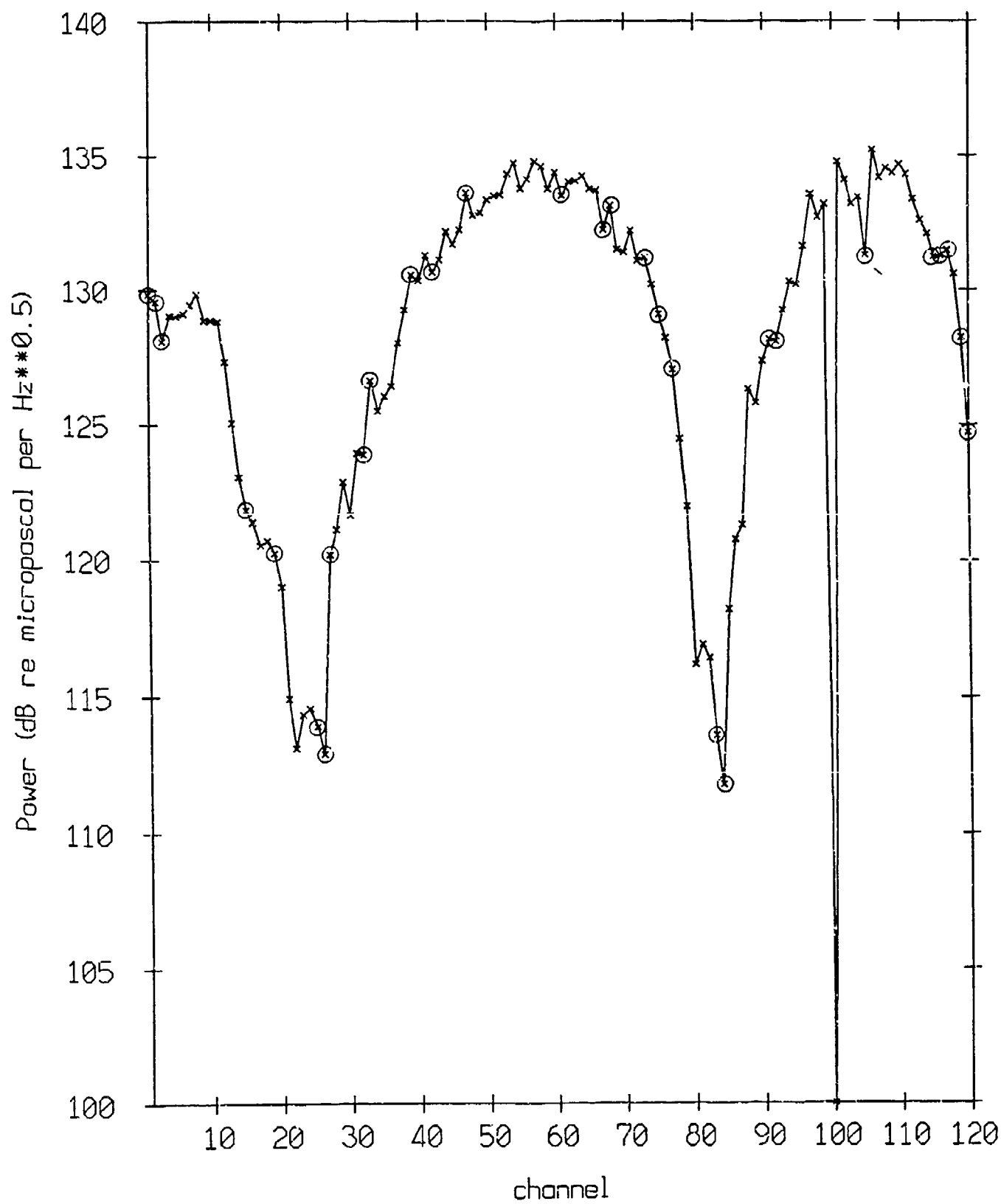
Narrowband Calibration: 159 Hz

GSM Results   16 Hz

34

GSM Results 22 Hz

Power (dB re micropascal per Hz**0.5) vs channel
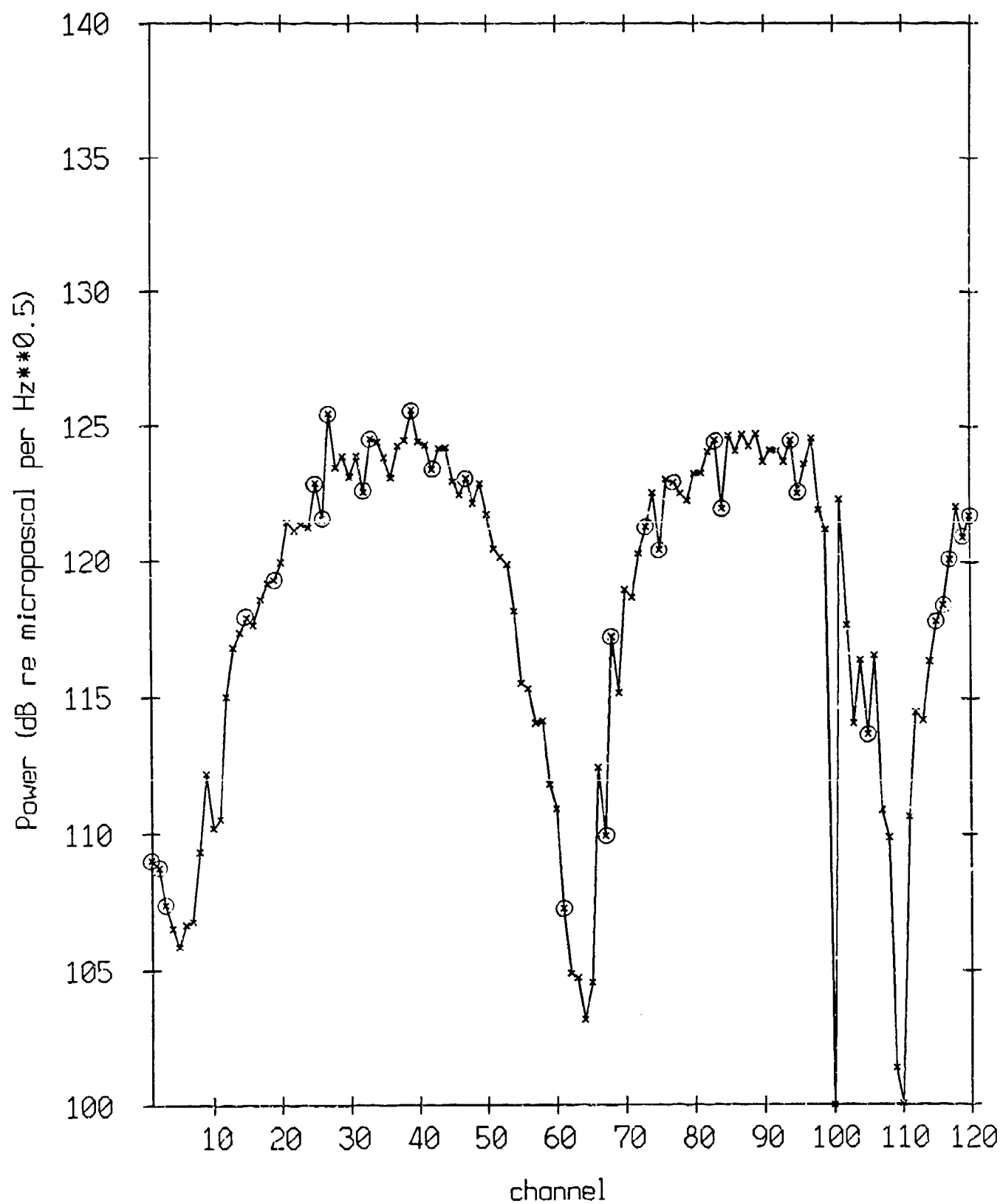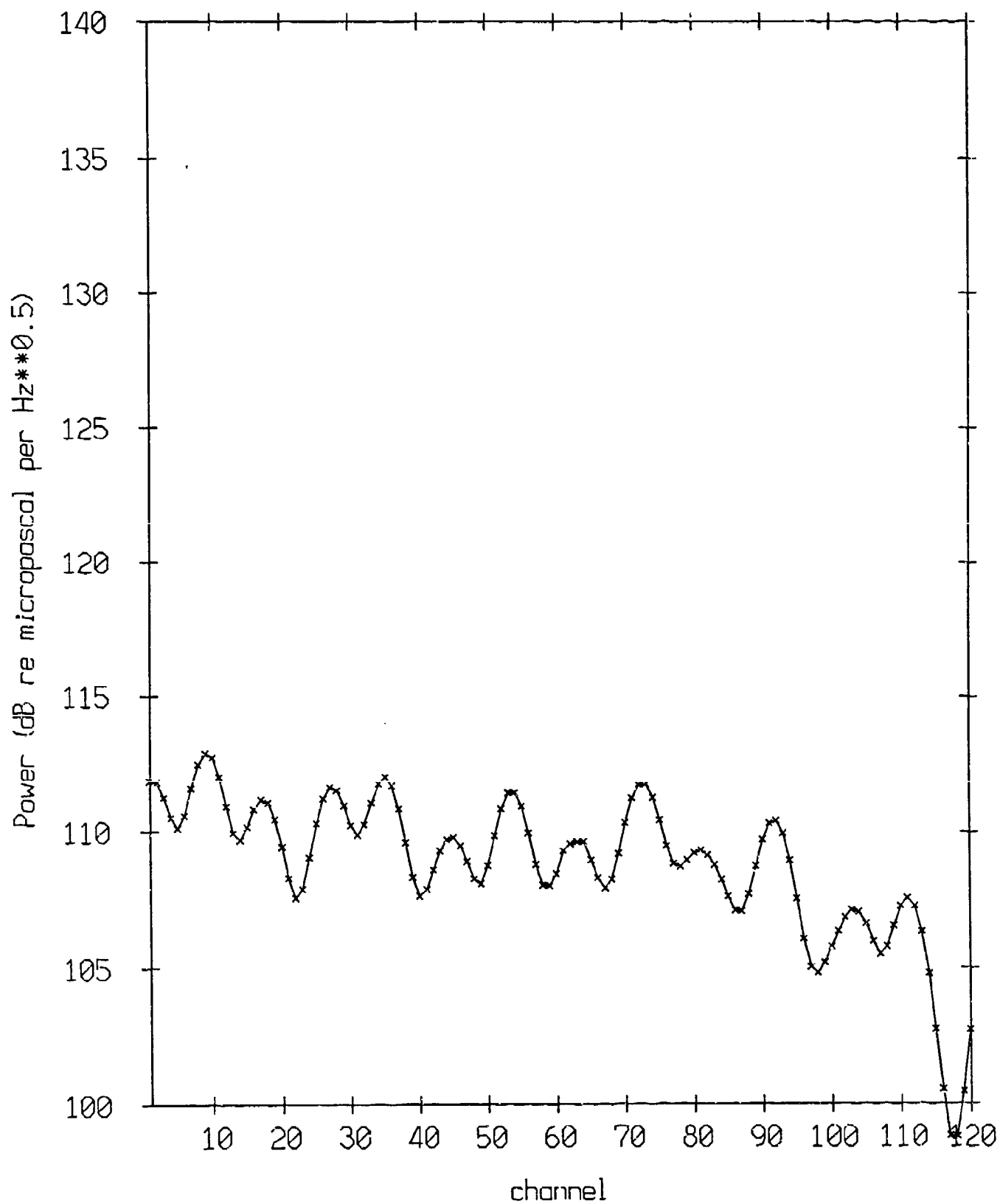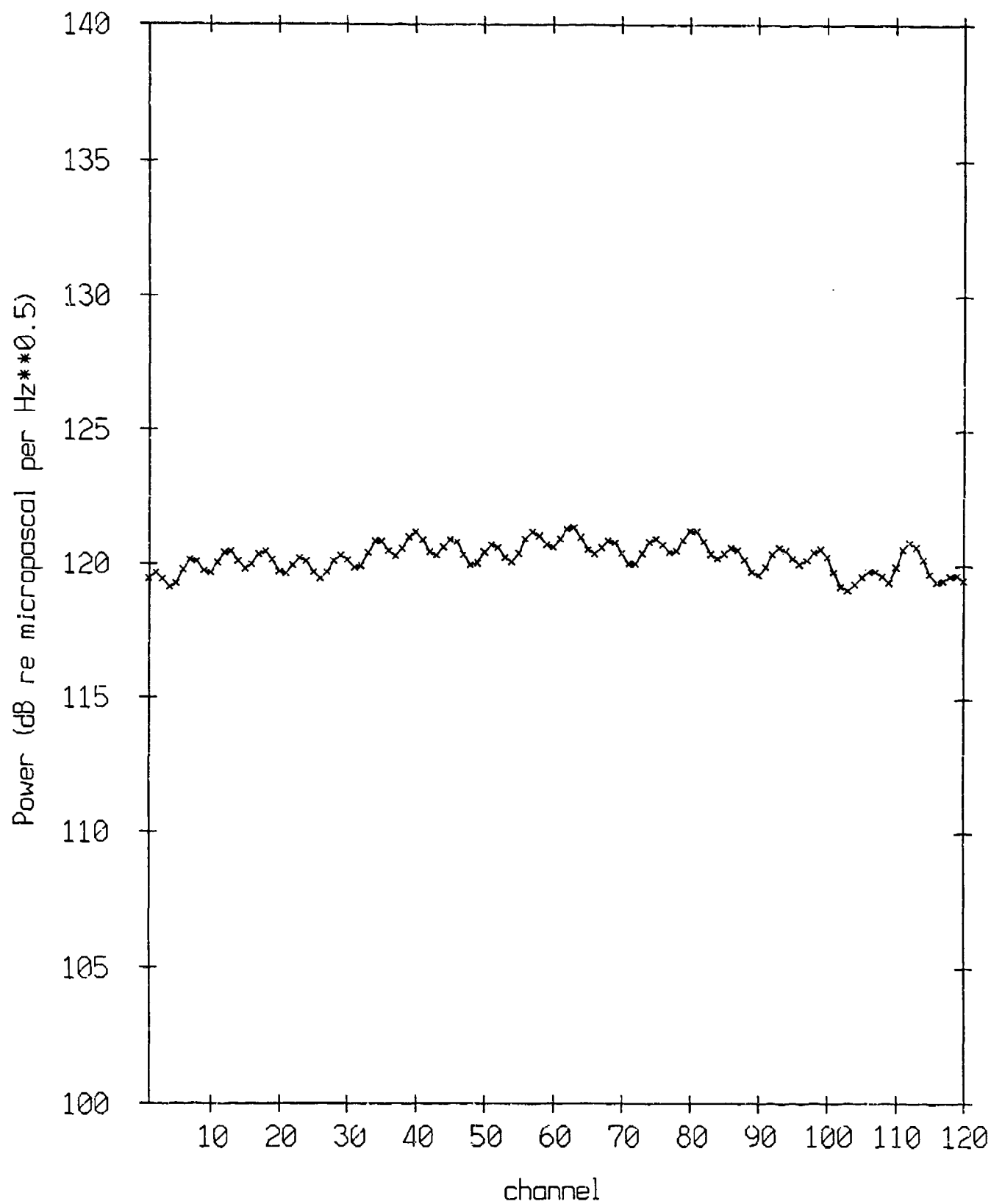
GSM Results   27 Hz

GSM Results   41 Hz

(Plot: Power (dB re micropascal per Hz**0.5) vs channel, ranging from channel 10 to 120, with power values between approximately 120 and 126)

37
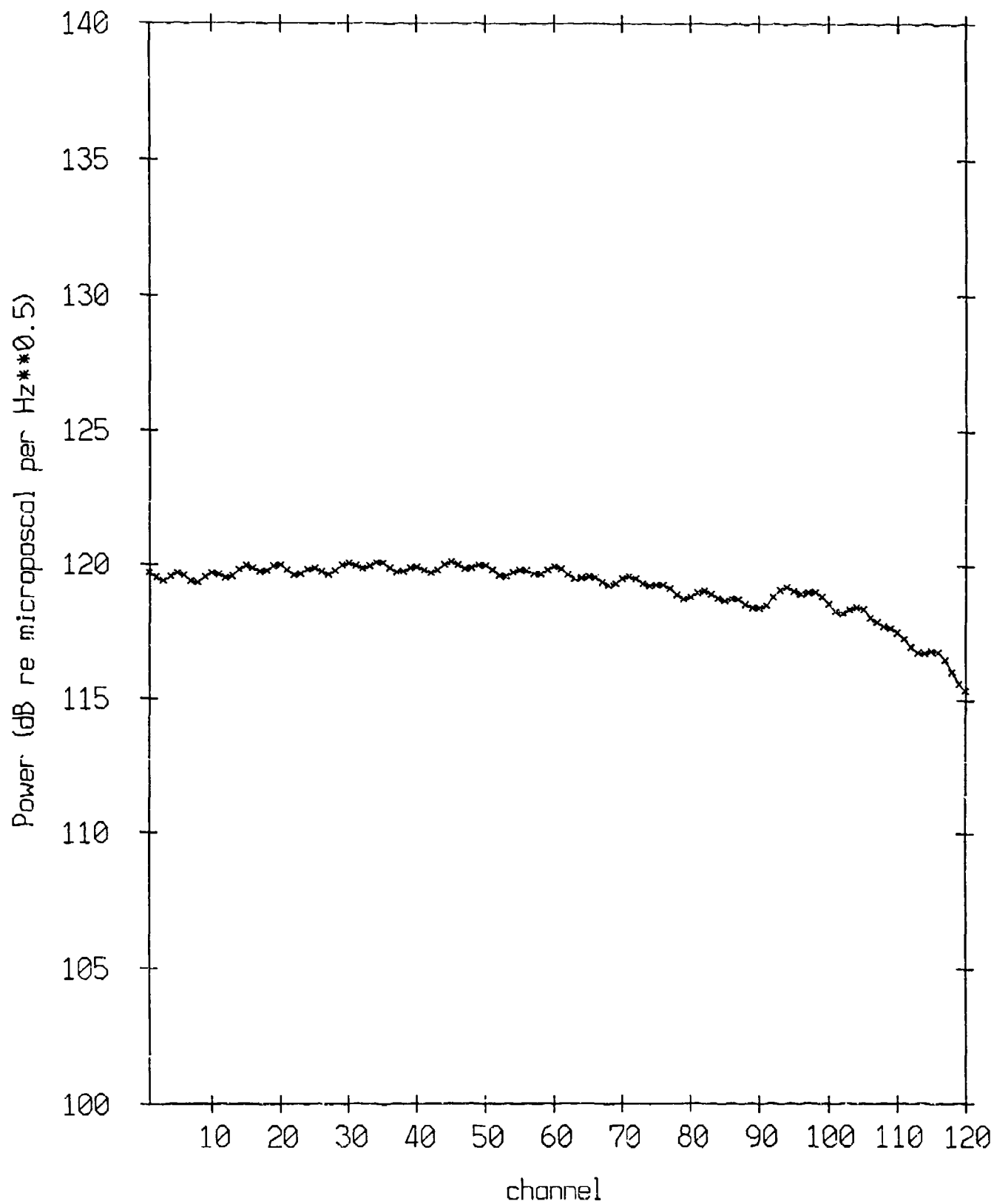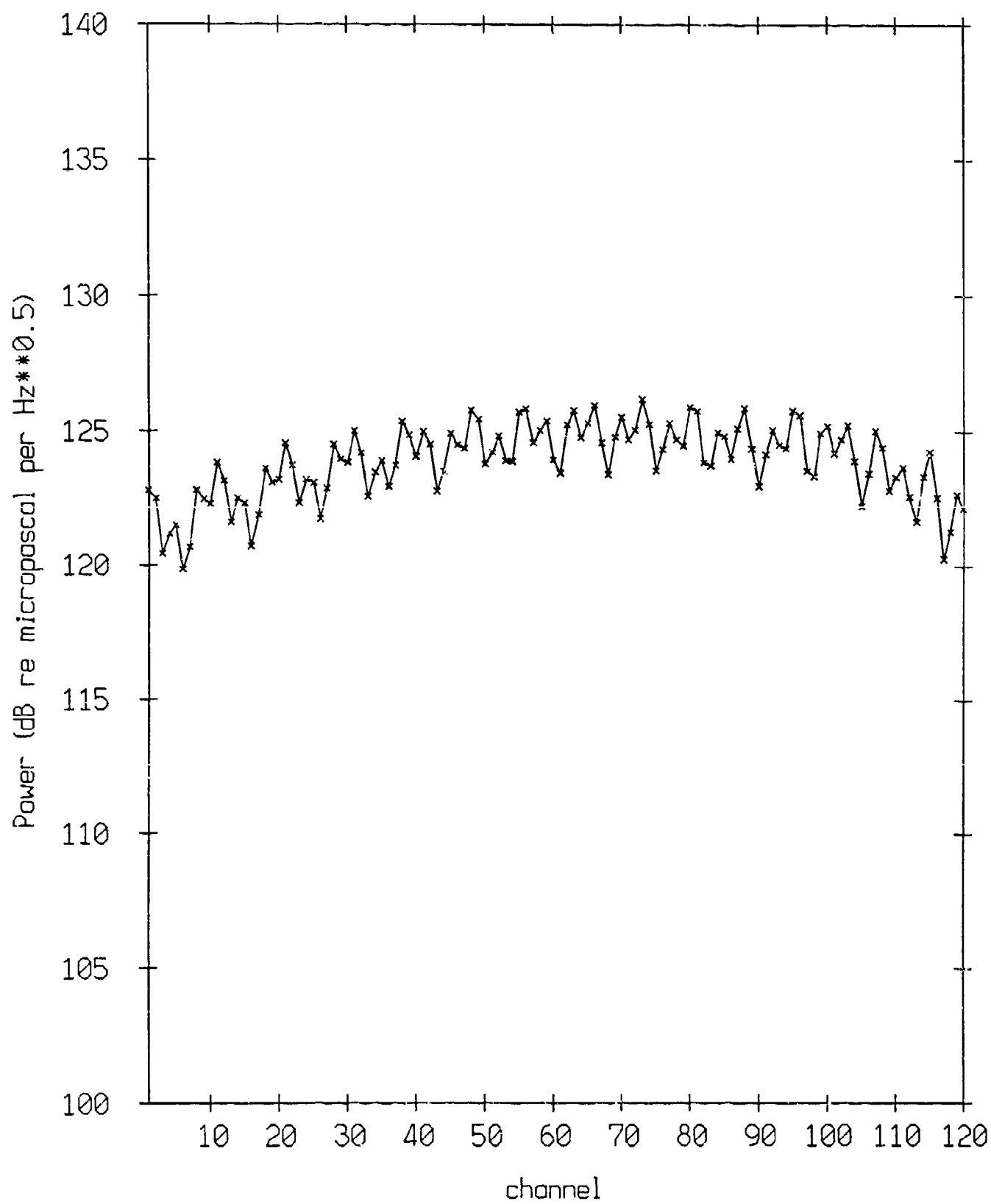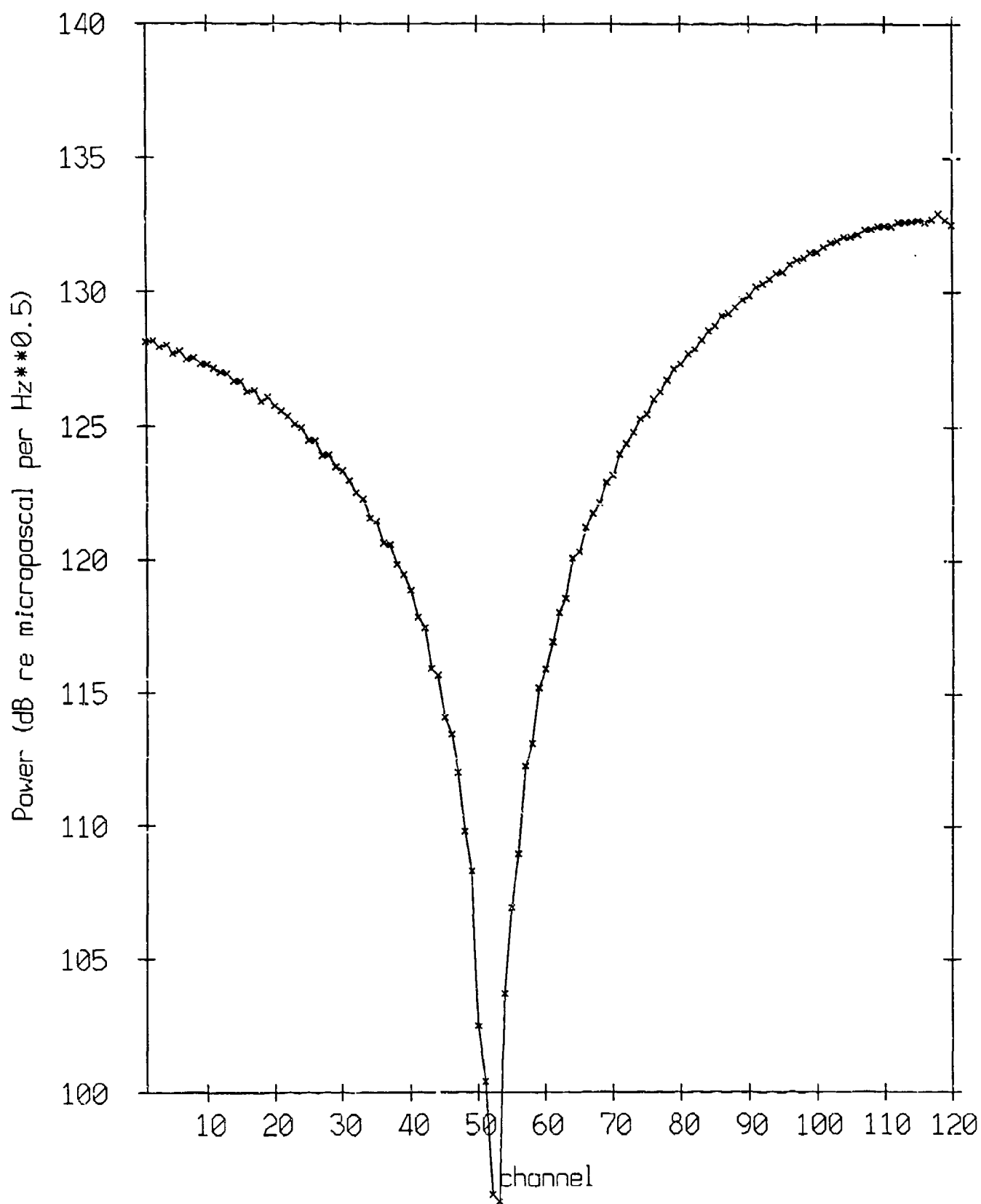
GSM Results   56 Hz

GSM Results   81 Hz

GSM Results   98 Hz

Power (dB re micropascal per Hz**0.5)

channel
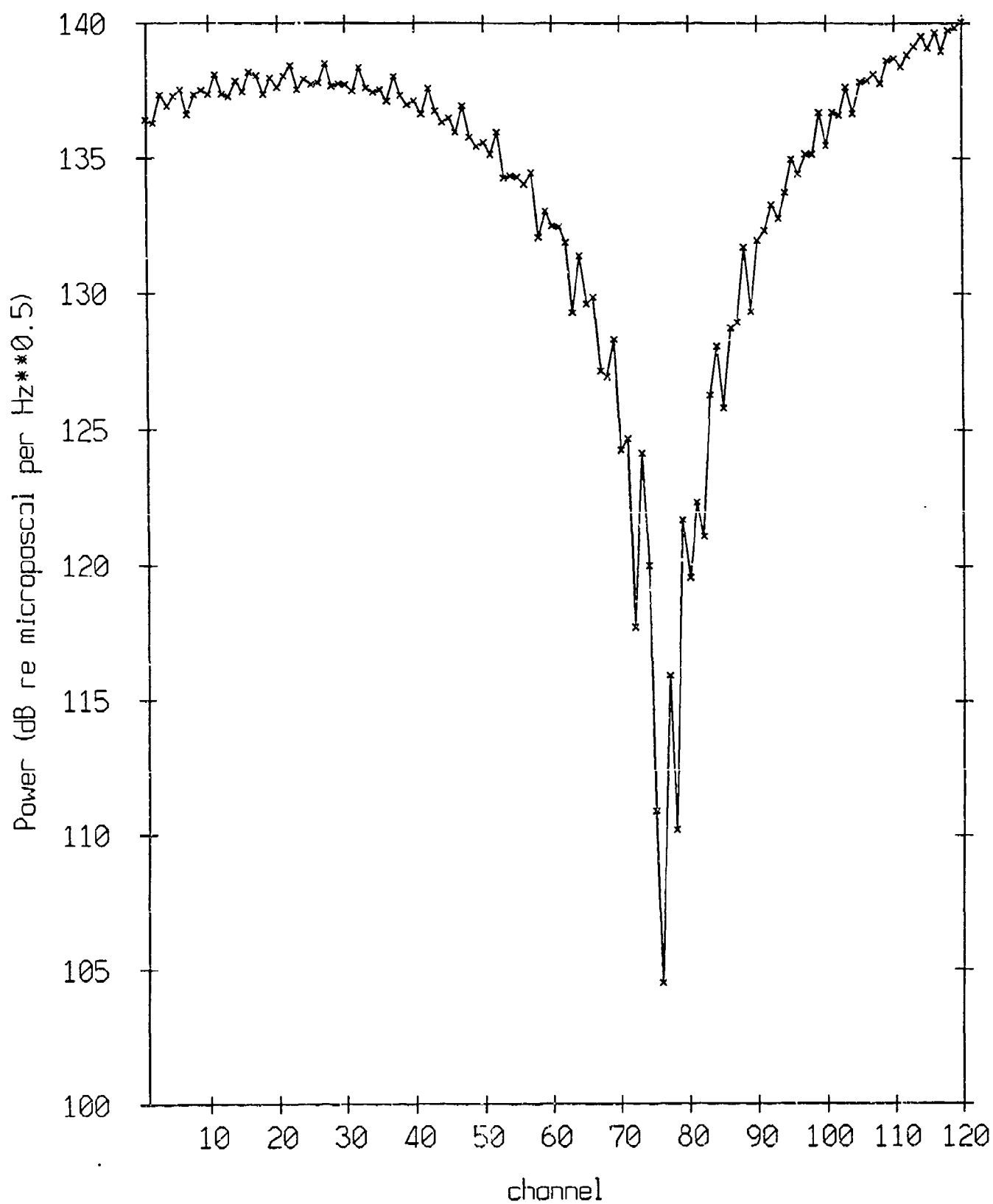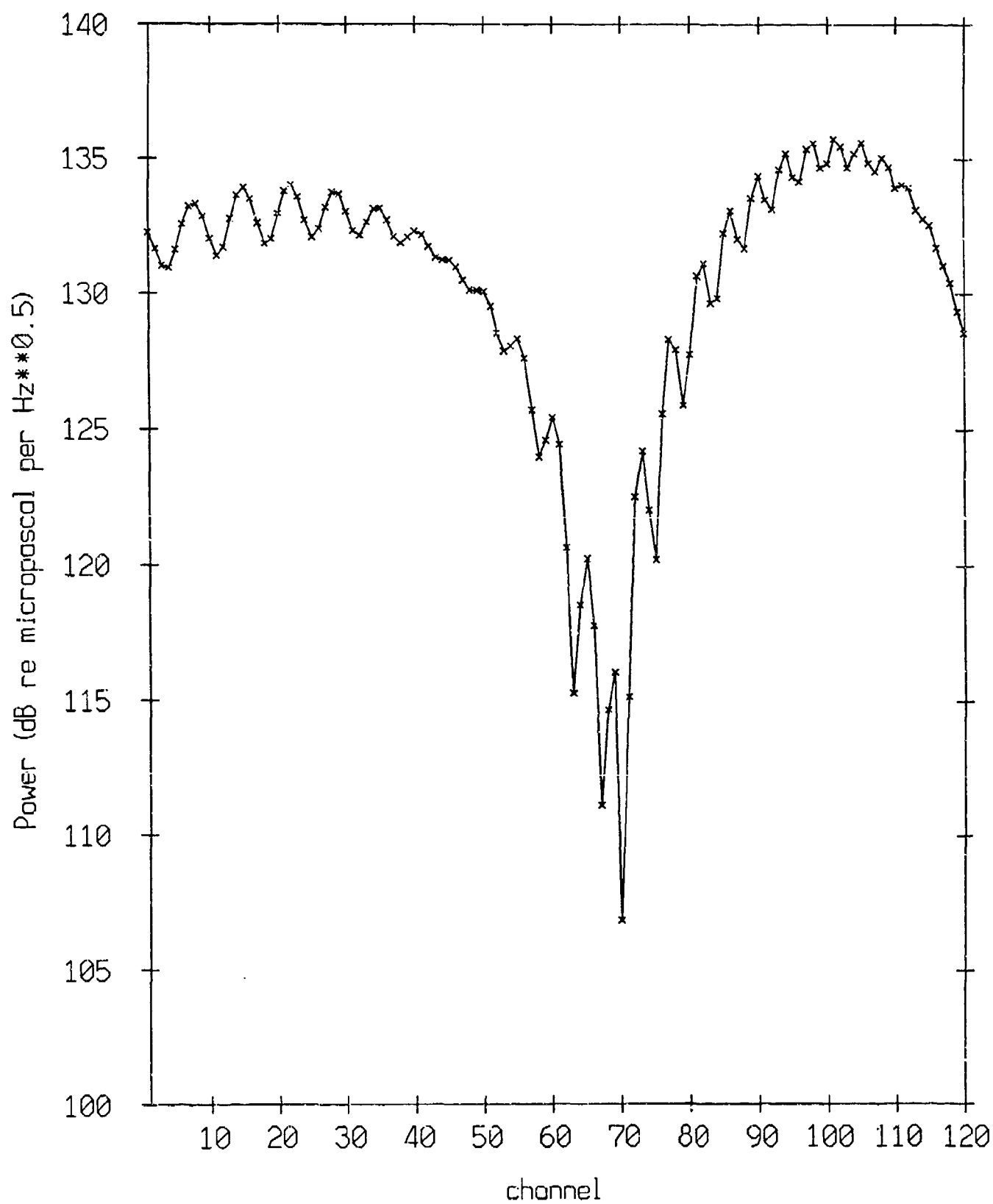
GSM Results 115 Hz

GSM Results   135 Hz

Power (dB re micropascal per Hz**0.5)

channel
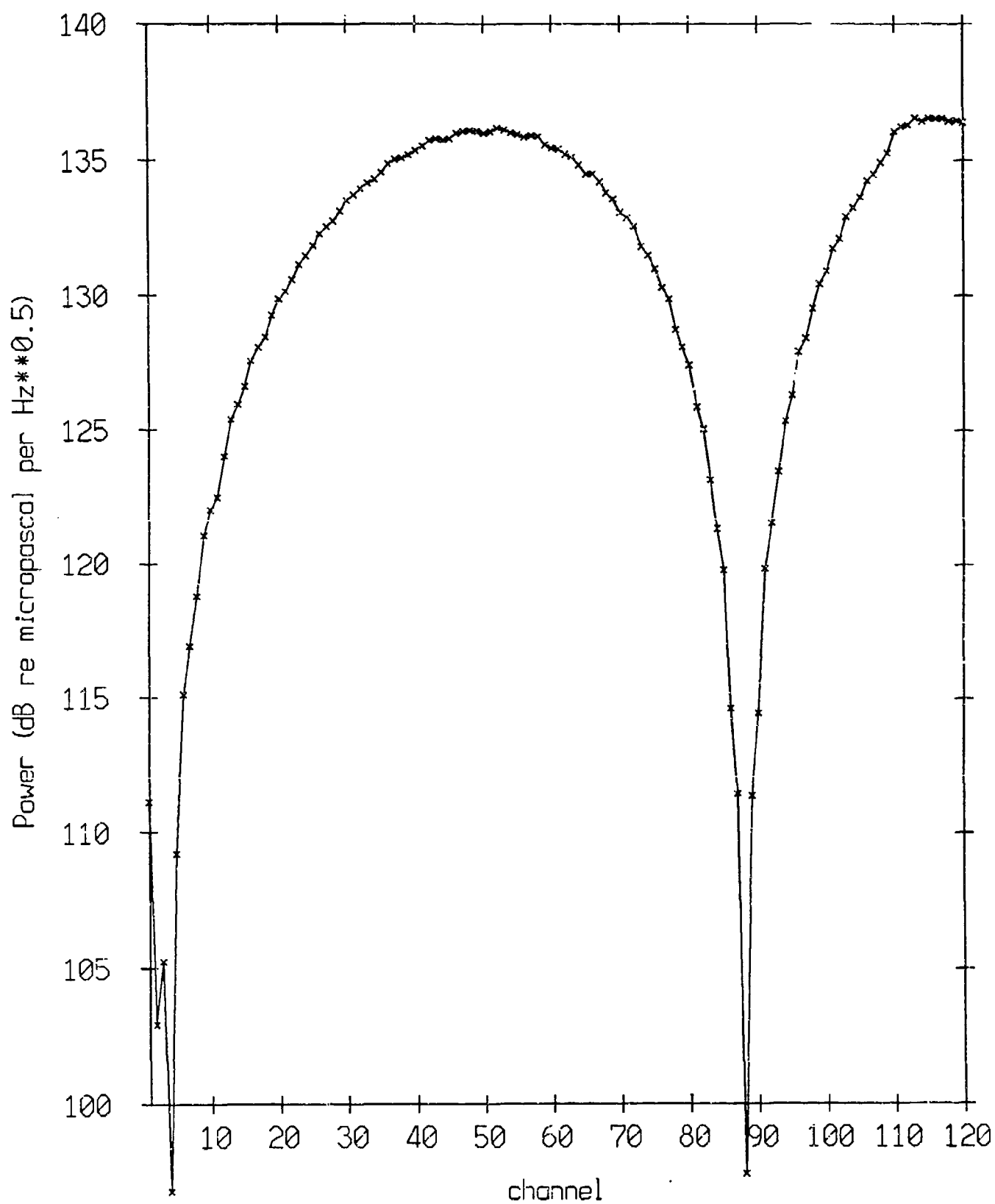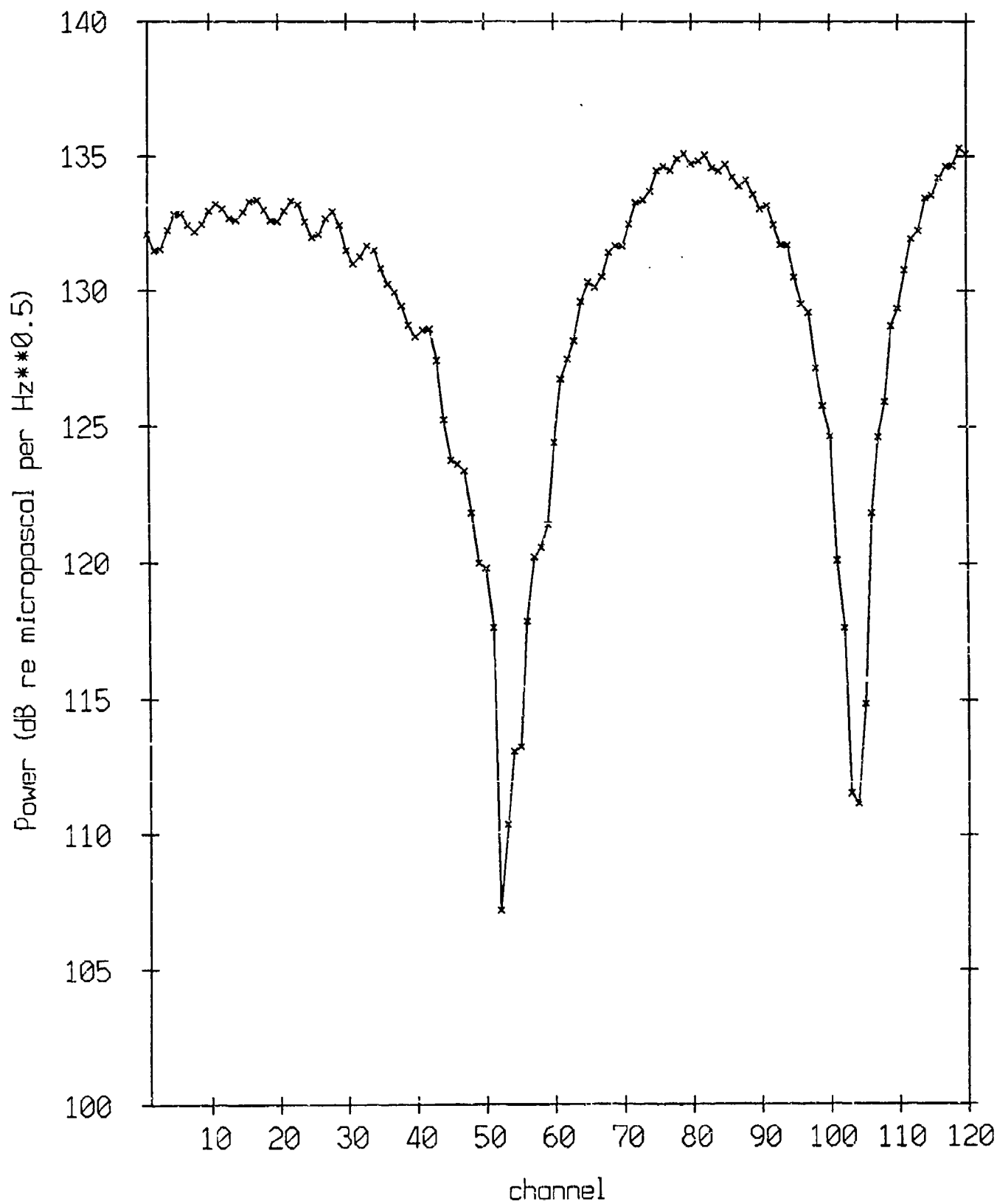
GSM Results   159 Hz
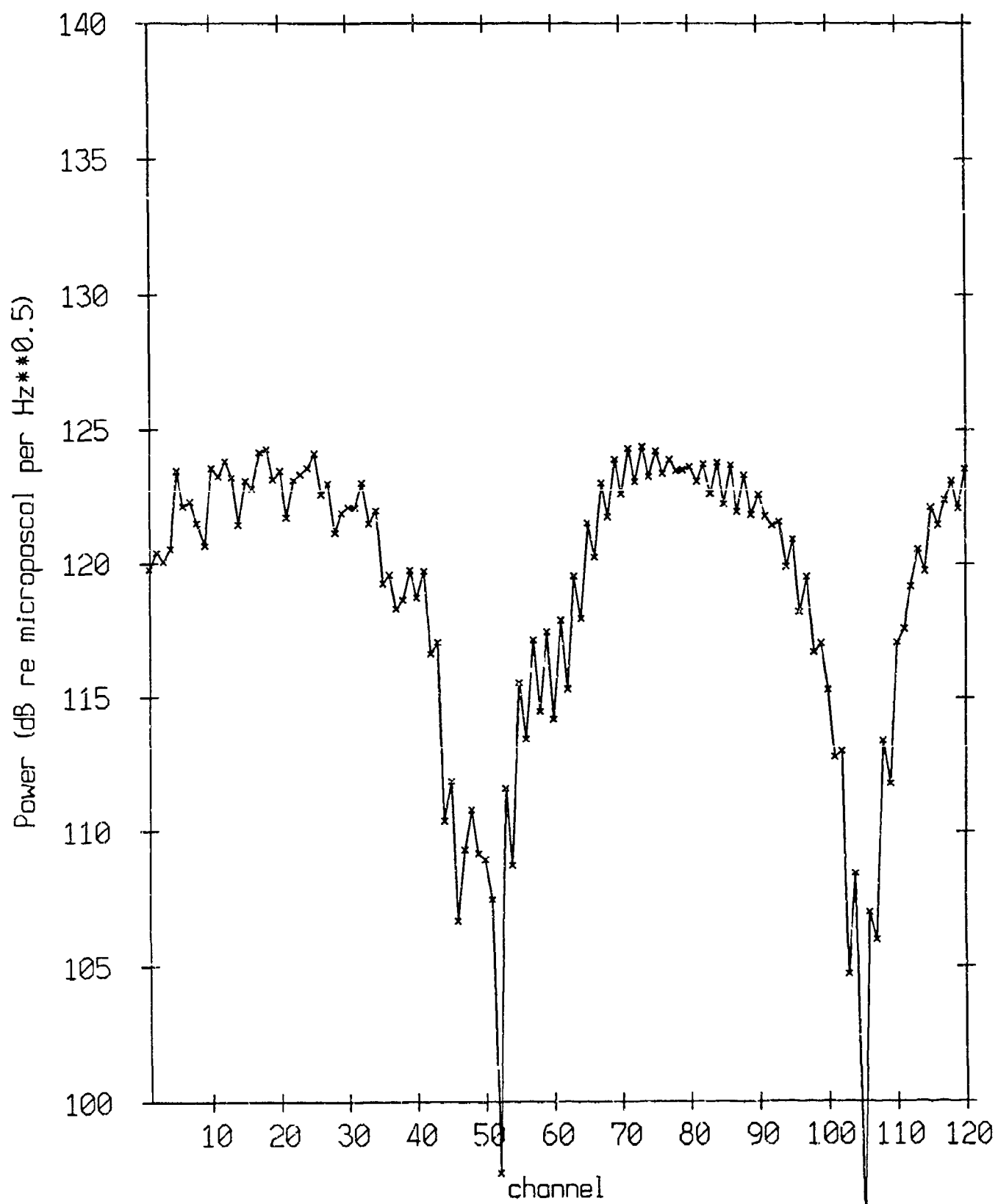
ATLAS: 16 Hz, SD:27 m, R:2295 m
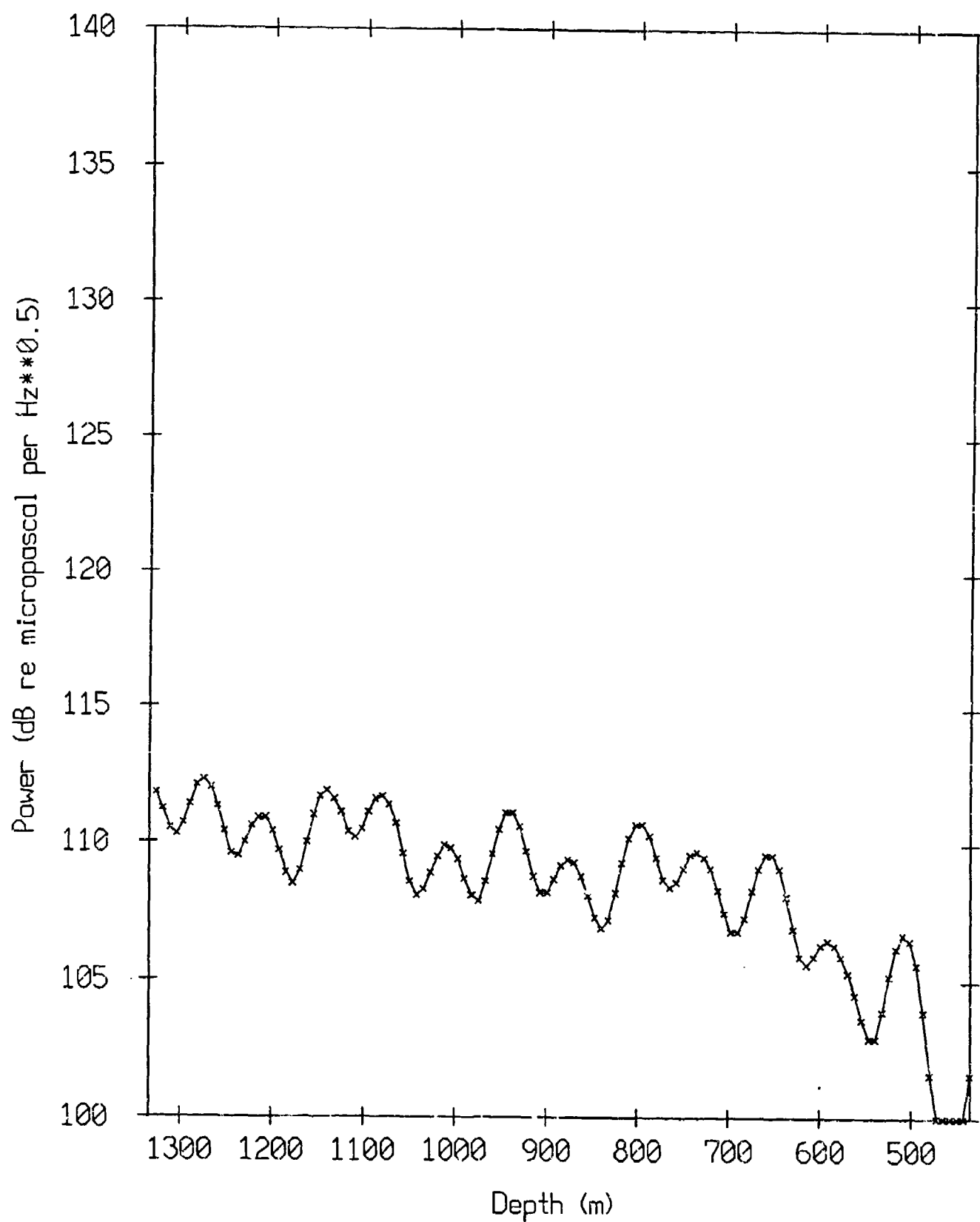
ATLAS: 22 Hz, SD:27 m, R:1332 m

45
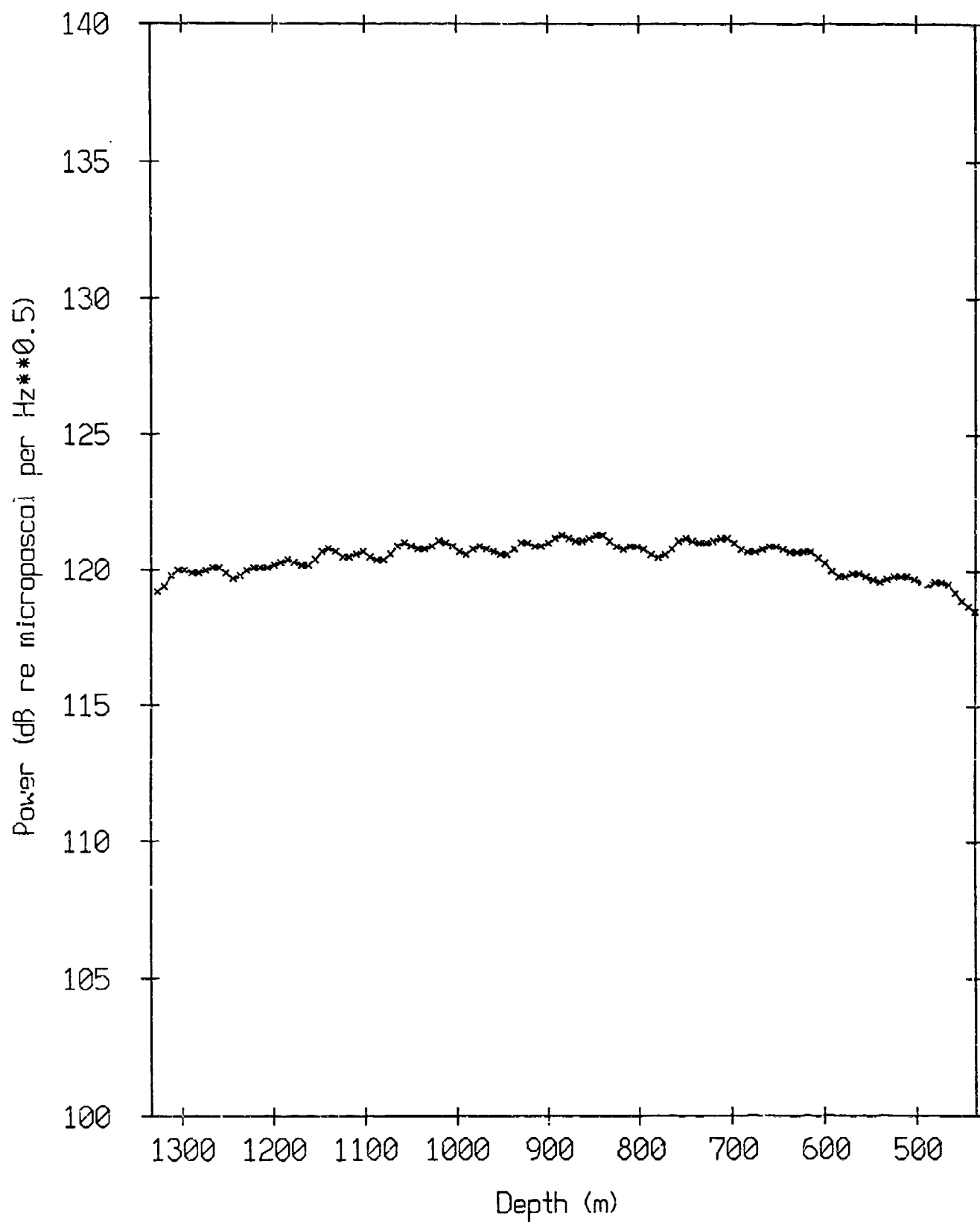
ATLAS: 27 Hz. SD:27 m, R:1944 m
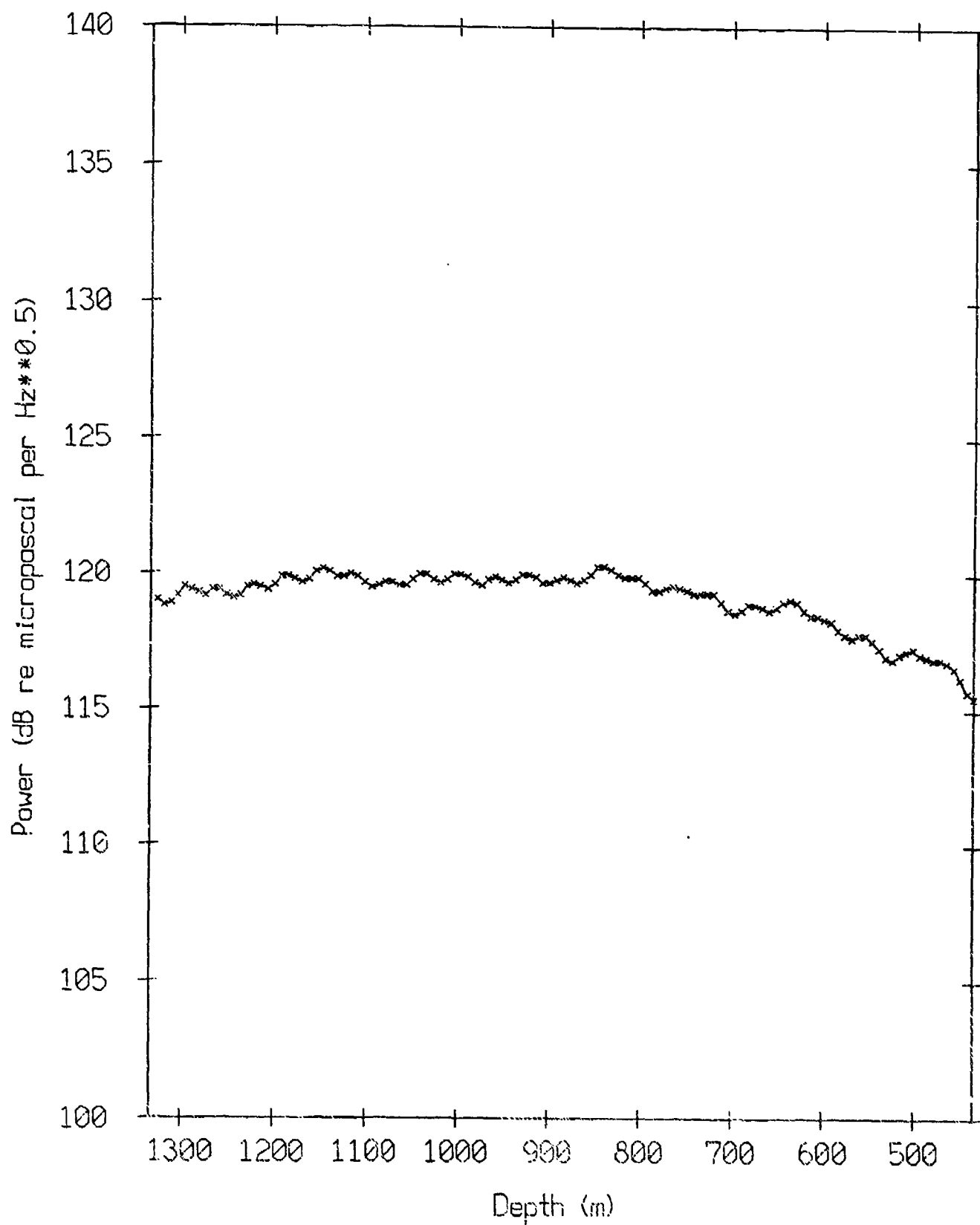
ATLAS: 41 Hz, SD:27 m, R:2142 m
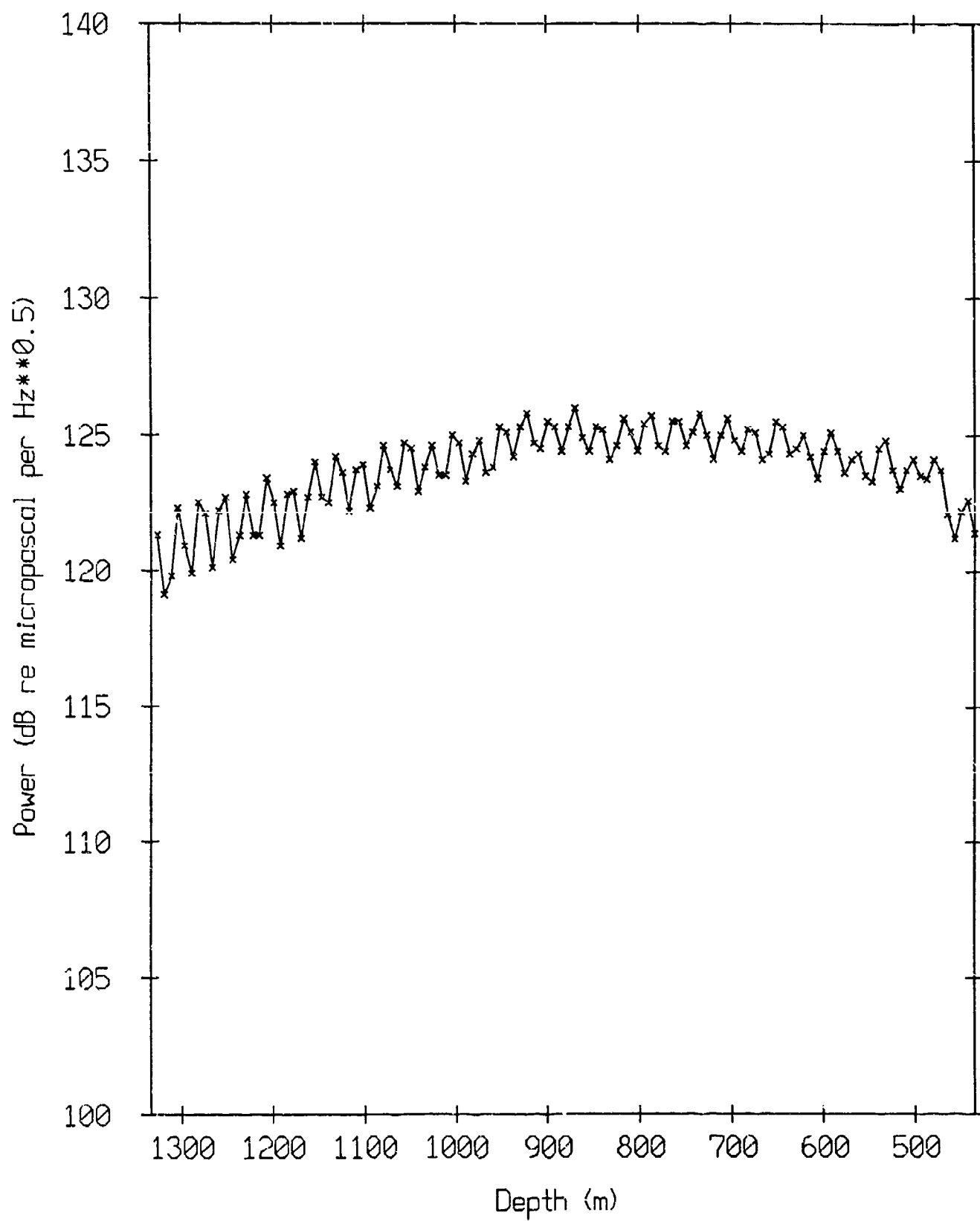
ATLAS: 56 Hz, SD:27 m, R:1550 m
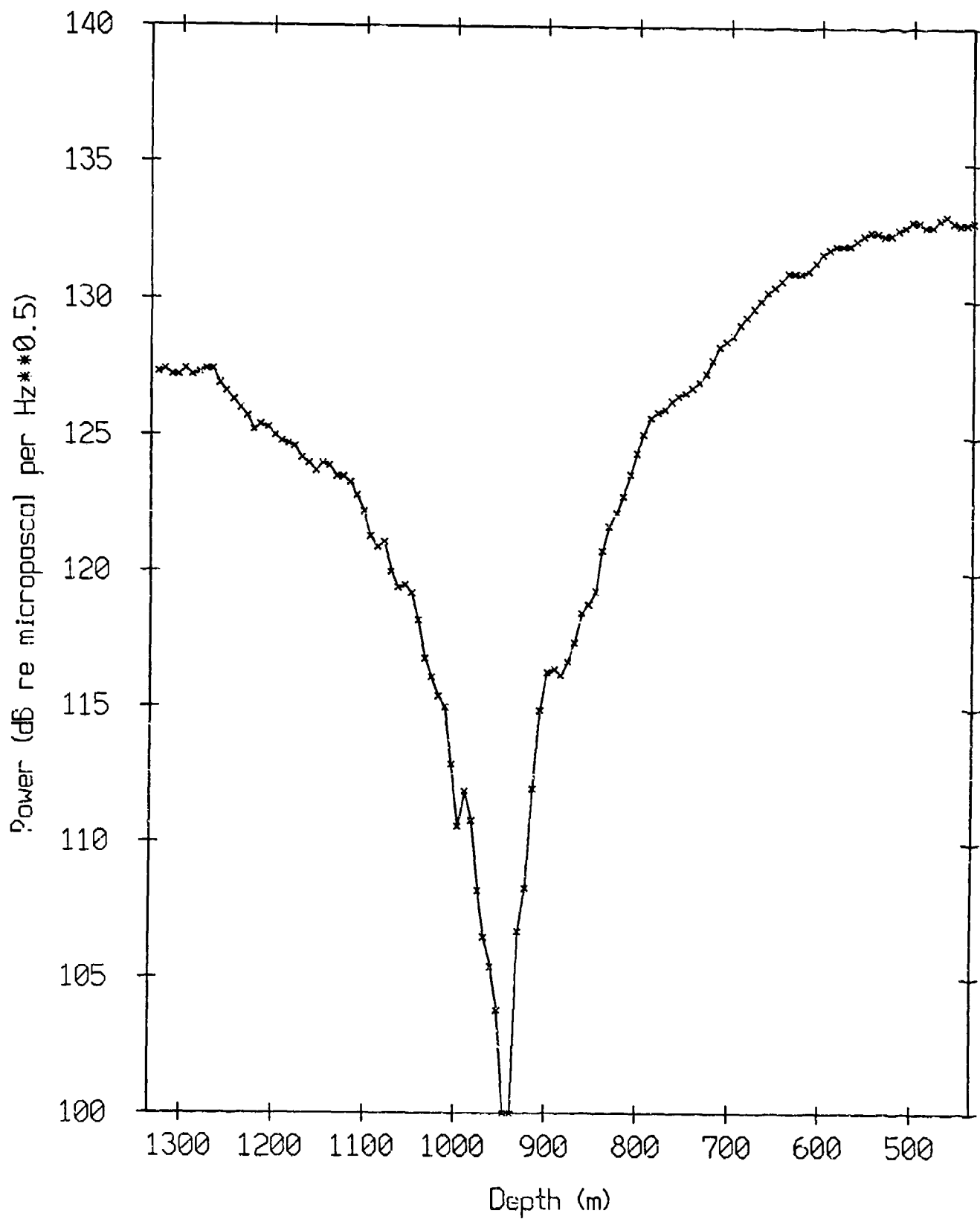
ATLAS: 81 Hz, SD:27 m, R:1854 m
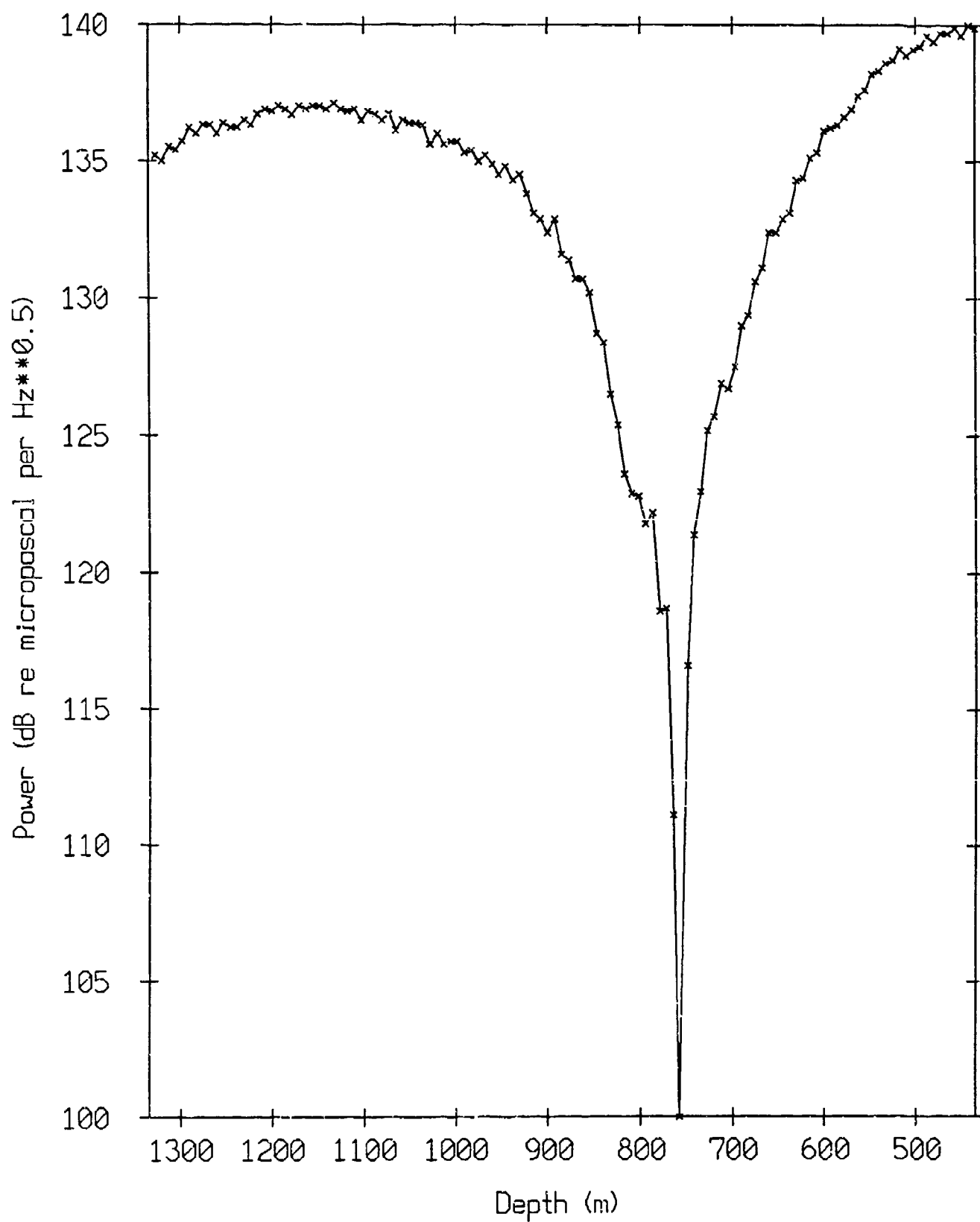
ATLAS: 98 Hz, SD:27 m, R:1141 m
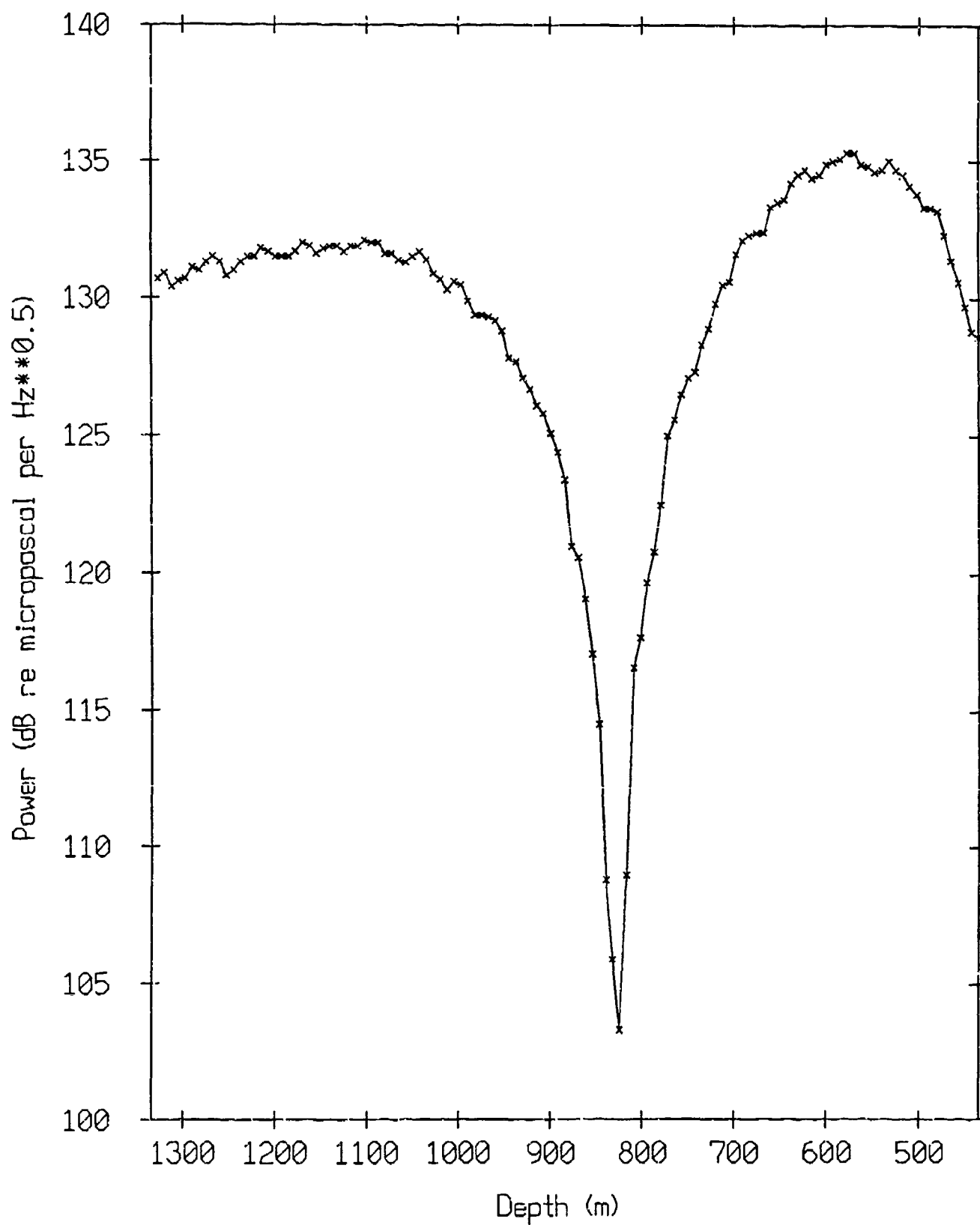
ATLAS: 115 Hz, SD:27 m, R:2217 m
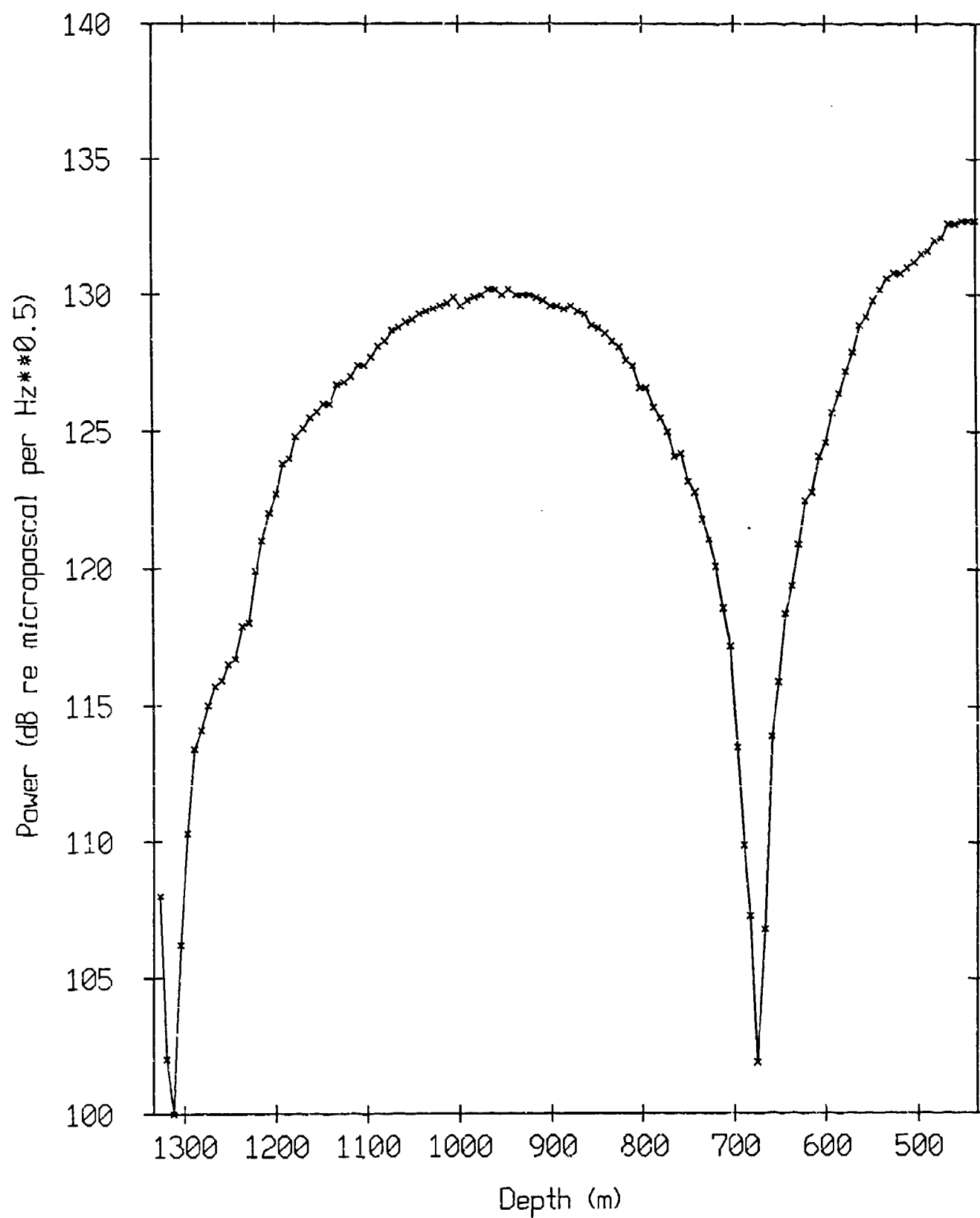
ATLAS: 135 Hz, SD:27 m, R:1141 m

Power (dB re micropascal per Hz**0.5) vs Depth (m)
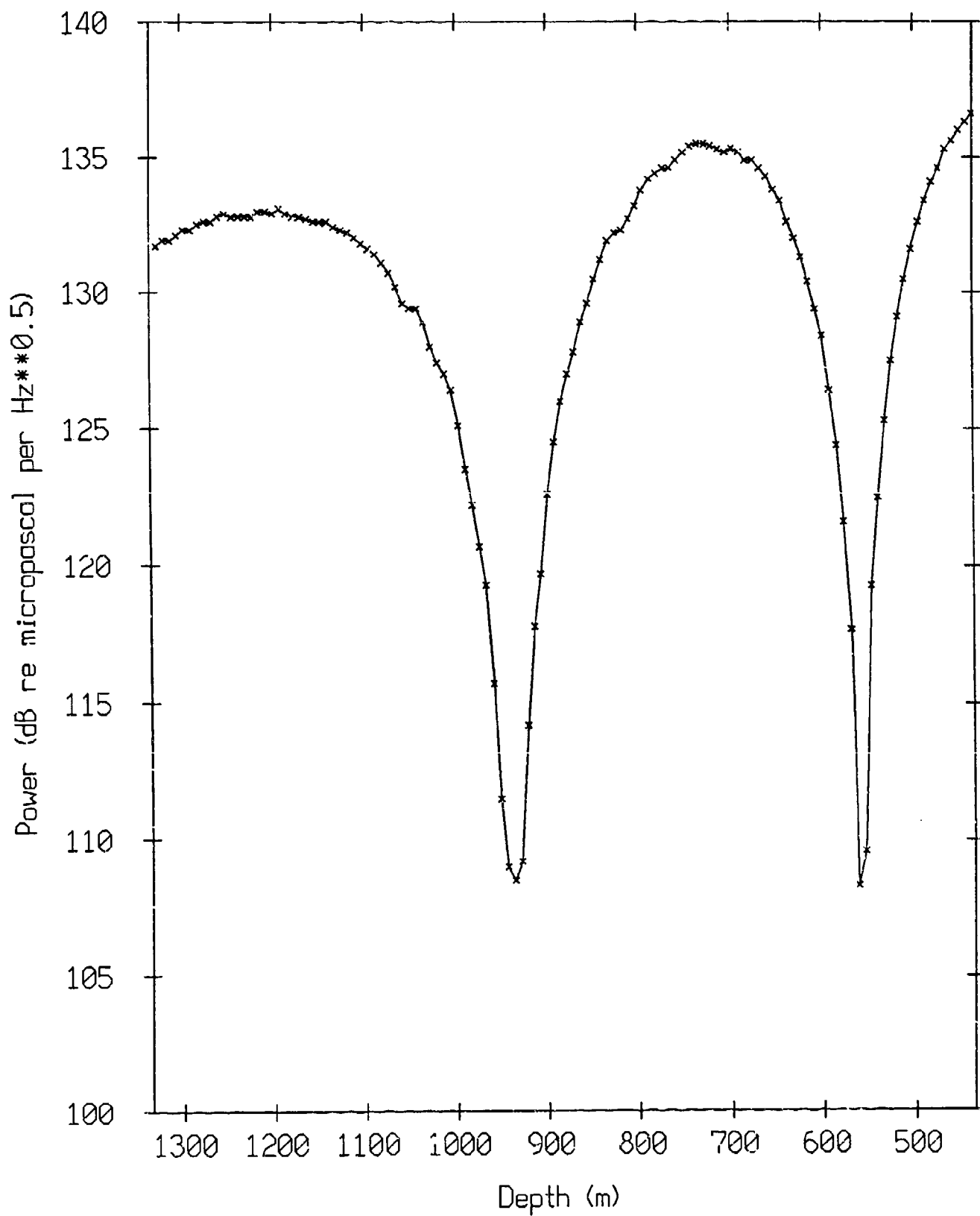
ATLAS: 159 Hz, SD:27 m, R:2276 m
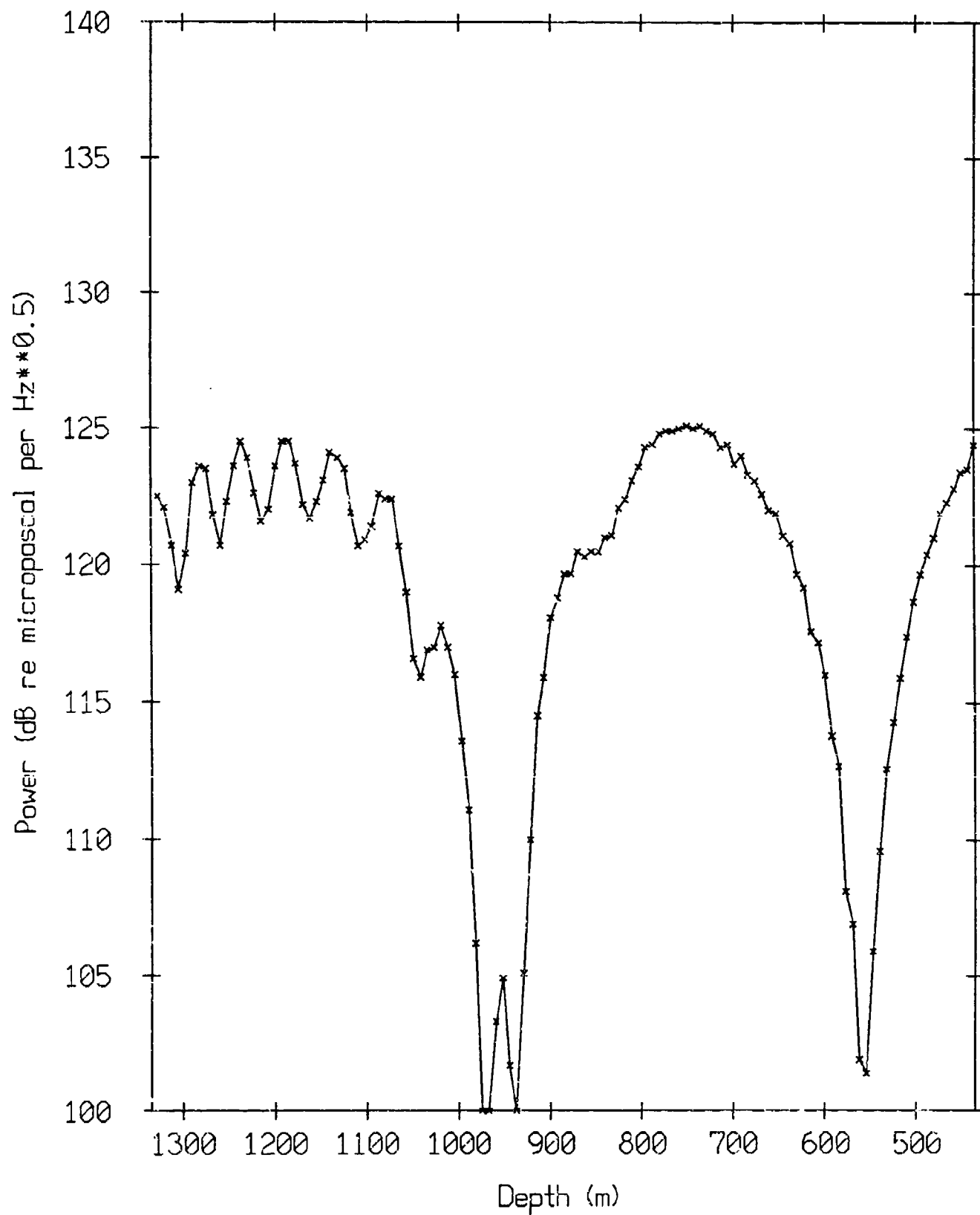
Regression Difference, 27 Hz

54

Regression Difference, 56 Hz

y-axis label: radians
x-axis label: channel
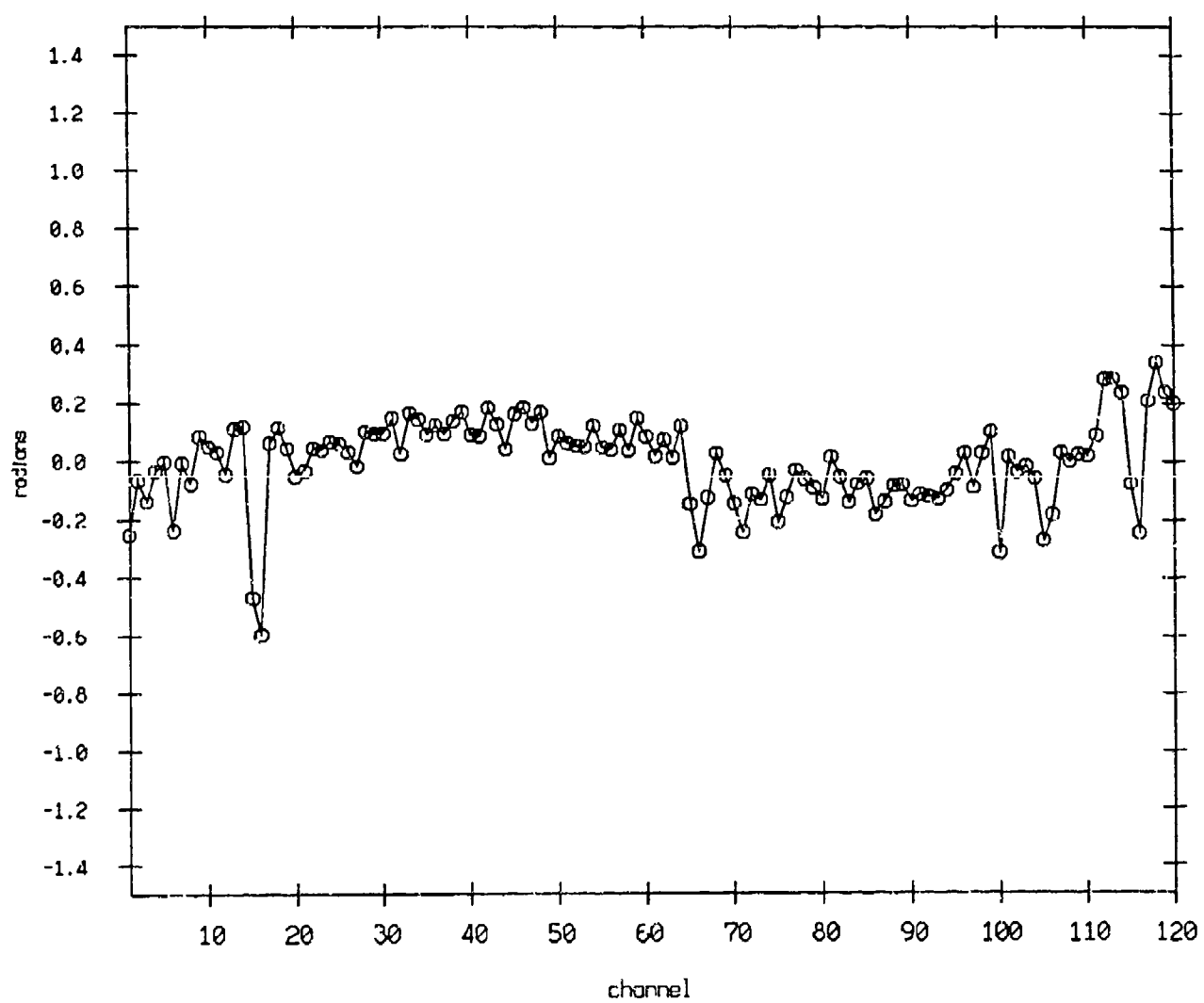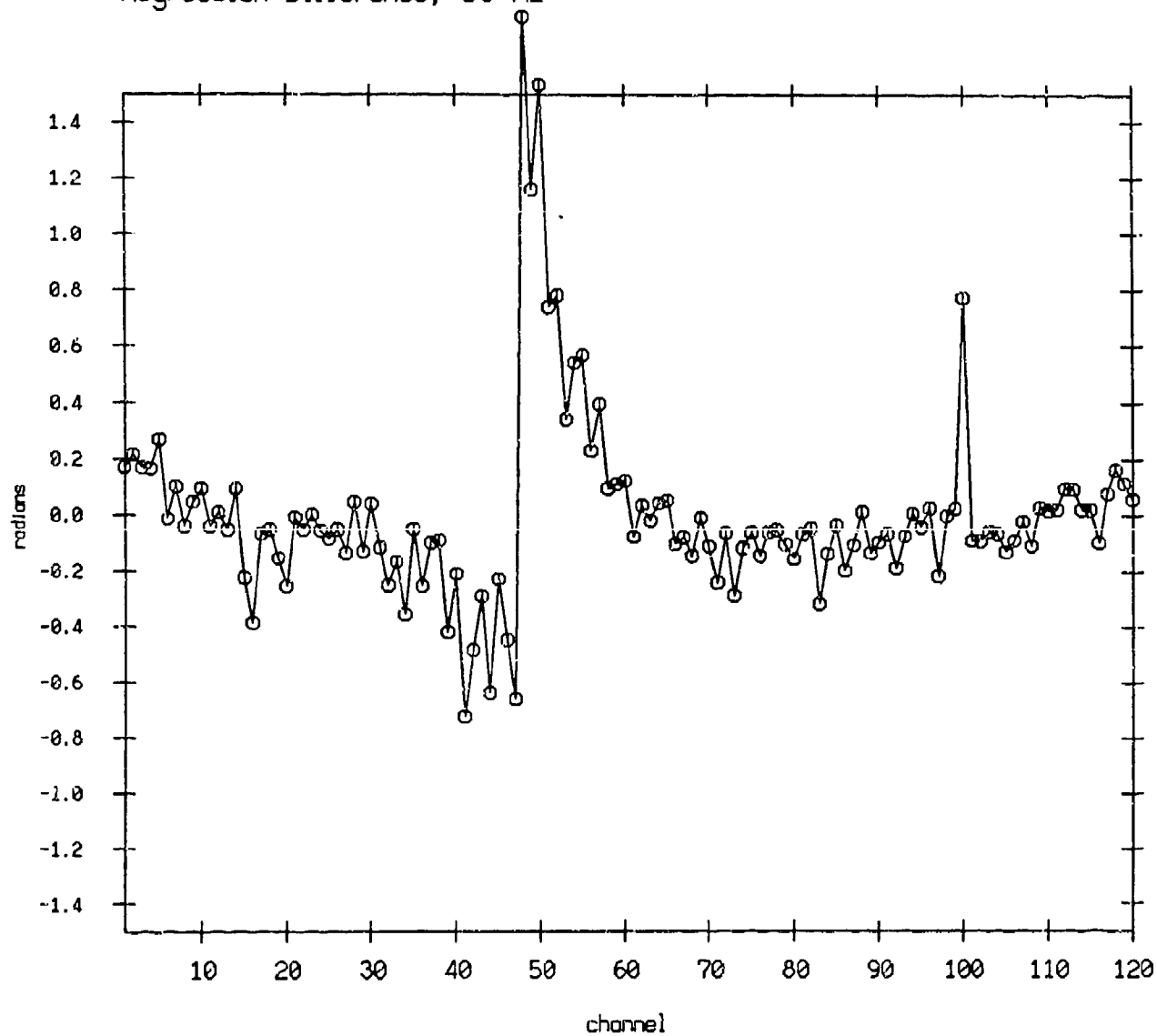
Regression Difference, 81 Hz
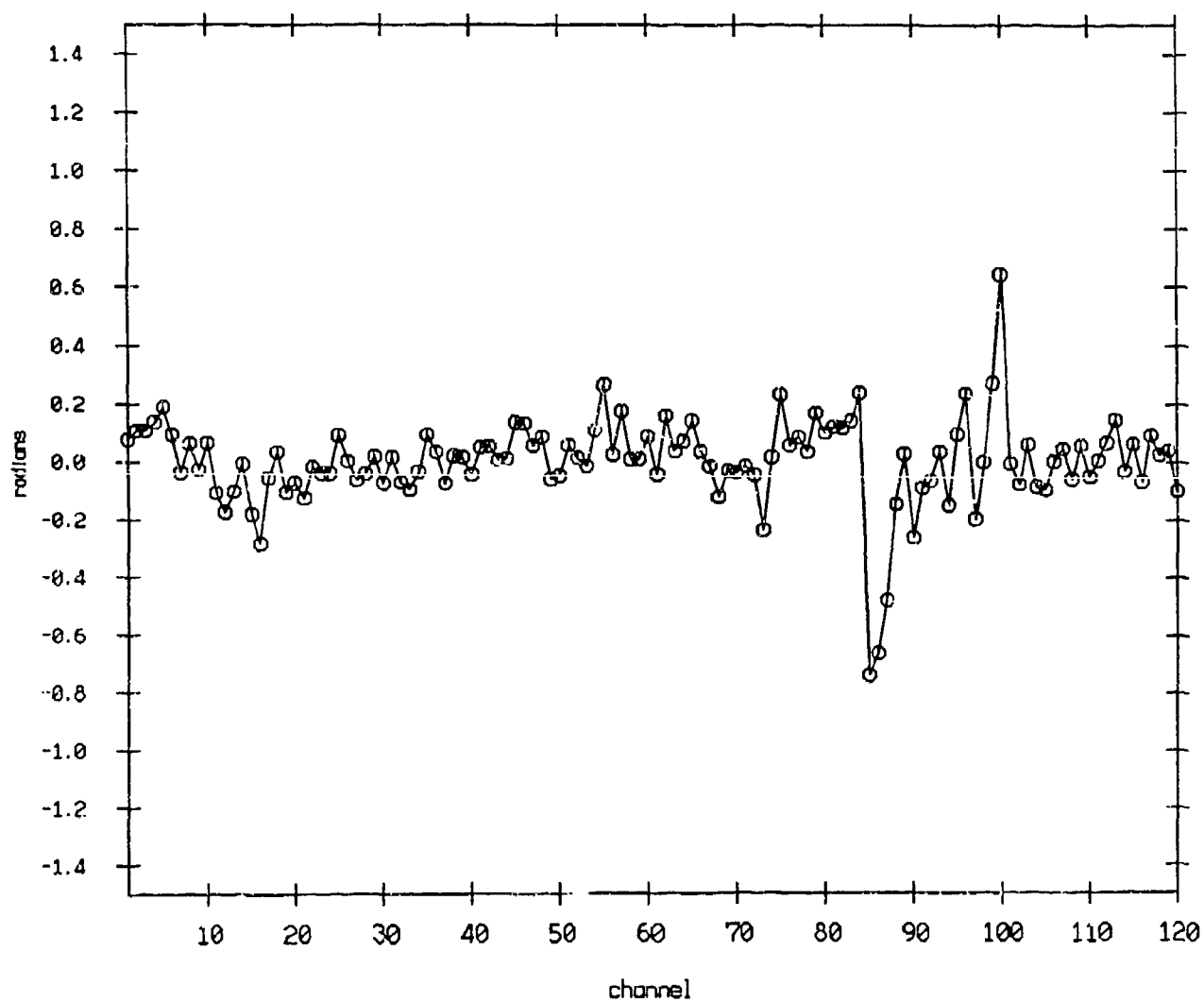
References

Anderson, V. C., private communication, Jan. 1989.

Bendat, J. S. and A. G. Piersol, *Random Data: Analysis and Measurement Procedures*, pp. 113, 128, 191. New York: Wiley-Interscience, 1971.

Bracewell, R. N. and J. A. Roberts, "Aerial smoothing in radio astronomy," Aust. J. Phys., Vol. 7, pp. 615-640, December 1954.

Cron, B. F., B. C. Hassell and F. J. Keltonic, "Comparison of Theoretical and Experimental Values of Spatial Correlation," J. Acoust. Soc. Am., Vol. 37, no. 3, pp. 523-529, March 1965.

D'Spain, G. L., private communication, May 1988.

Dyer, I., "Statistics of sound propagation in the ocean," J. Acoust. Soc. Am., 48(1), pp. 337-345, 1970.

Hodgkiss, W. S. and F. H. Fisher, "Vertical Directionality of Ambient Noise at 32° N as a Function of Longitude," Technical Memorandum 387, Marine Physical Laboratory, Scripps Institution of Oceanography, San Diego, CA, 1987.

Lastinger, J. J., "Measurements on NORDA/DTAG AQ-1 Hydrophones," Calibration Memorandum 6891, Underwater Sound Reference Detachment, NRL, Orlando, FL, 1982.

Morris, G. B., "Depth Dependence of Ambient Noise in the Northeastern Pacific Ocean," J. Acoust. Soc. Am., 64(2), pp. 581-590, Aug. 1978.

Nuttall, A. H., "Effects of Random Shading, Phasing Errors, and Element Failures on Beampatterns of Linear and Planar Arrays," NUSC TR 6191, Naval Underwater Systems Center, New London, CT, 1979.

Quazi, A. H. and A. H. Nuttall, "Effects of Random Shading, Phasing Errors and Element Failures on the Beampatterns of Line and Planar Arrays," IEEE ICASSP Proc., 79CH1379-7 ASSP, pp. 290-293, April, 1979.

Quazi, A. H., "Array beam response in the presence of amplitude and phase fluctuations," J. Acoust. Soc. Am., Vol. 72, no. 1, pp. 171-180, July, 1982.

Ramsdale, D. J. and R. A. Howerton, "Effect of element failure and random errors in amplitude and phase on the sidelobe level attainable with a linear array," J. Acoust. Soc. Am. Vol. 68, no. 3, pp. 901-906, Sept. 1980.

Sherrill, M. S. and R. L. Streit, "*In Situ* Optimal Reshading of Arrays with Failed Elements," IEEE Journal of Oceanic Engineering, OE-12, No 1, pp. 155-162, Jan. 1987.

Sotirin, B. J. and J. A. Hildebrand, "Large Aperture Digital Acoustic Array," IEEE Journal of Oceanic Engineering, OE-13, No 4, pp. 271-281, Oct. 1988.

Sotirin, B. J. and J. A. Hildebrand, "Acoustic navigation of a large aperture array," J. Acoust. Soc. Am., submitted for publication March, 1989.

Sotirin, B. J. and W. S Hodgkiss, "Fine-scale measurements of the vertical ambient noise field," in progress, 1989.

Stutzman, W. L., and G. A. Thiele, *Antenna Theory and Design*, pp. 108-167, New York: John Wiley and Sons, Inc., 1981.

Urick, R. J., *Principles of Underwater Sound*, 3rd ed. pp. 6-11, New York: McGraw-Hill Book Co., 1983.

Wagstaff, R. A., J. L. Berrou and F. D. Cotaras, "Use of the towship for assessing towed-array performance and analyzing data quality," J. Acoust. Soc. Am., Vol. 72, no. 3, pp. 983-992, Sept. 1982.

Table 4.1. Narrowband Transmission Parameters.						
Frequency Hz	range meters	source level dB re uPa	file.sio start time (49152 pts)	file.ssio start time (8192 pts)	tape number	skpbuf
98	1141.375	192.0	22:54:37.824	22:54:59.984	758	1312
135	1141.375	193.1	23:03:46.566	23:04:59.986	758	5600
22	1331.655	179.7	23:08:53.697	23:09:59.997	758	8000
56	1550.325	191.3	23:13:39.074	23:14:59.994	758	10390
81	1853.546	199.3	23:19:29.716	23:19:59.996	759	1970
27	1943.869	181.5	23:24:29.809	23:24:59.989	759	4315
41	2141.568	186.6	23:33:59.538	23:34:59.998	759	8767
115	2216.663	198.2	23:38:59.887	23:39:59.987	760	114
159	2275.890	186.0	23:44:00.108	23:44:59.988	760	2460
16	2295.145	176.3	23:48:59.562	23:49:59.982	760	4800
11	2358.765	170.0	23:54:00.295	23:54:59.995	760	7150

Depth of the top of the array estimated from tape 744:   435 meters

Table 4.2. Results of Narrowband Calibration										
Channel:	1	2	3	4	5	6	7	8	9	10
P1	-1	+1	-2							
P2					-1				-1	
P3					+1	-1	+2			
P4		-2	+.5							
P5		-.5					+1			
P6										
P7	-1						-1	+1		
P8			+1		-1		+1			
P9			+.5	-1						
P10				+1.5	-1					
P11					-5					
P12					-1	-1	-1		-1	-1

ARRAY SECTION DIAGRAM
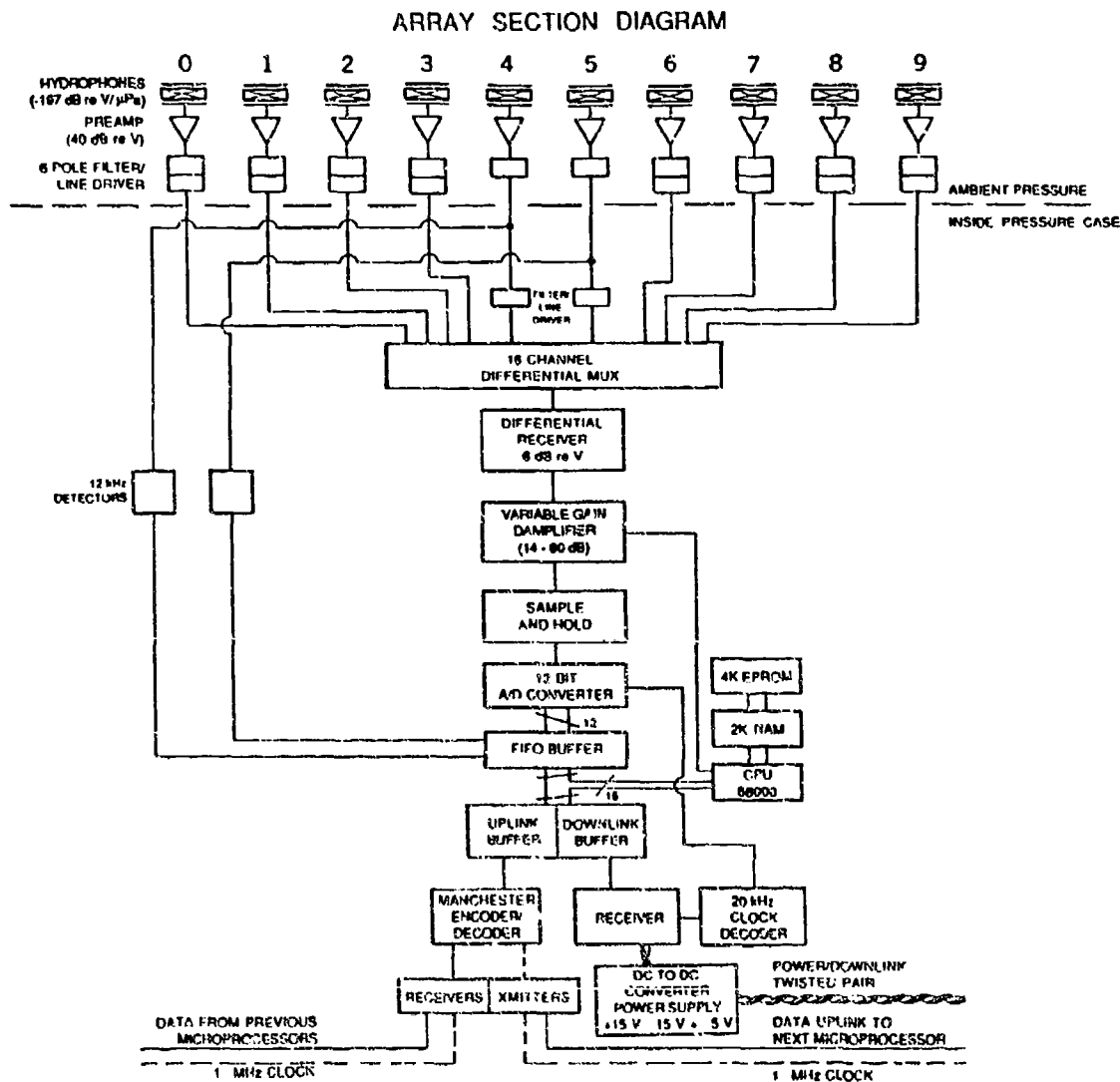
Figure 1 Array section schematic. The hydrophone signals are amplified and filtered at ambient temperature and pressure except for hydrophones 4 and 5 which are filtered within the processor pressure case to allow detection of 12 kHz navigation signals. The low frequency acoustic signals are multiplexed, amplified, captured by the sample and hold, and converted to digital format before being transmitted to the surface.
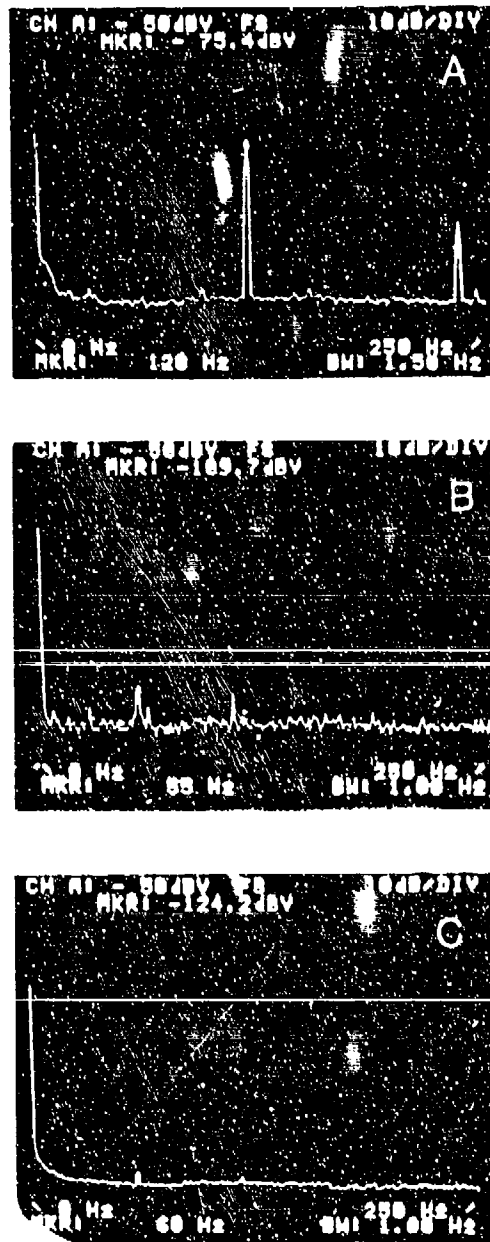
Figure 2 Power supply spectra. The photo of a spectrum analyzer window displays the spectra of (a) the DC-to-DC converter 5 VDC input, (b) the 5 VDC DC-to-DC output, and (c) the ±15 VDC DC-to-DC output. Narrowband signals other than line frequency harmonics were intermittent.
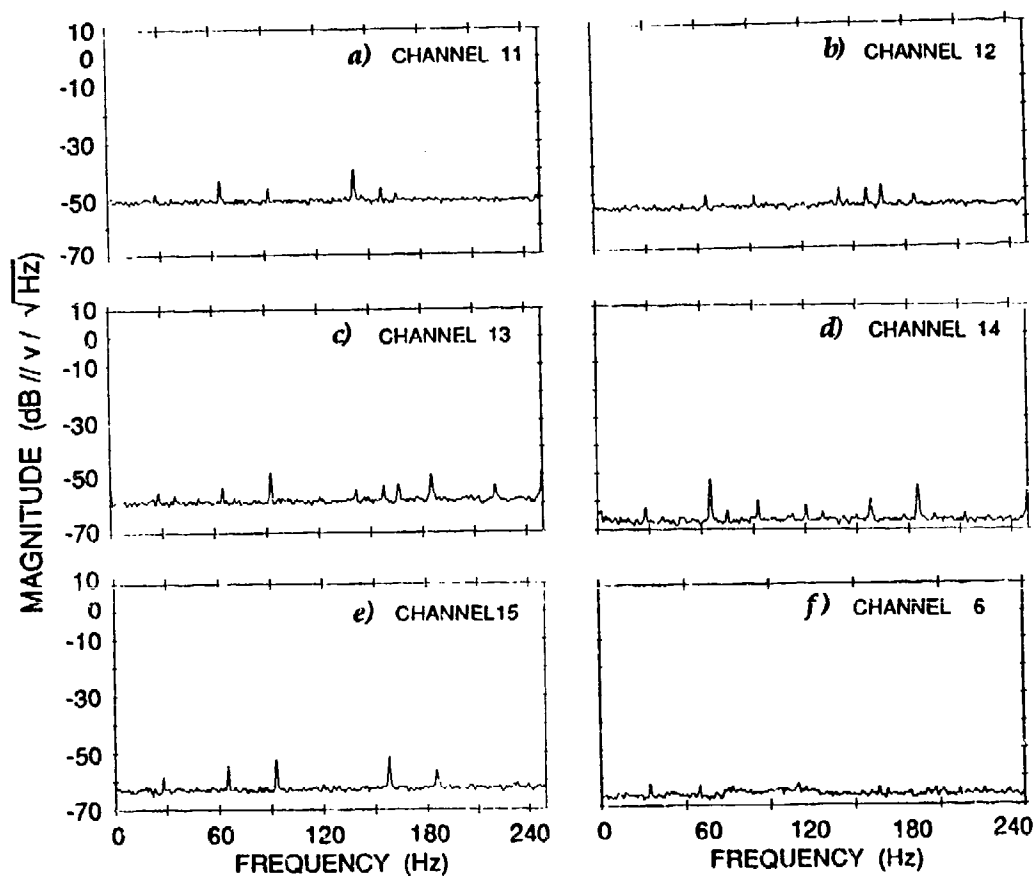
Figure 3 Common mode switching noise. The 1 MHz clock signal running the length of the array couples into the low level analog signals. This noise is suspected as the noise levels increase with increasing distance. In the figure, (a) Channel 11 transmitts 33.75 m, (b) Channel 12 transmitts 26.25 m, (c) Channel 13 transmitts 18.75 m, (d) Channel 14 transmitts 11.25 m, and (e) Channel 15 transmitts 3.75 m. The final panel (f) shows the array output with the variable gain stage shorted.
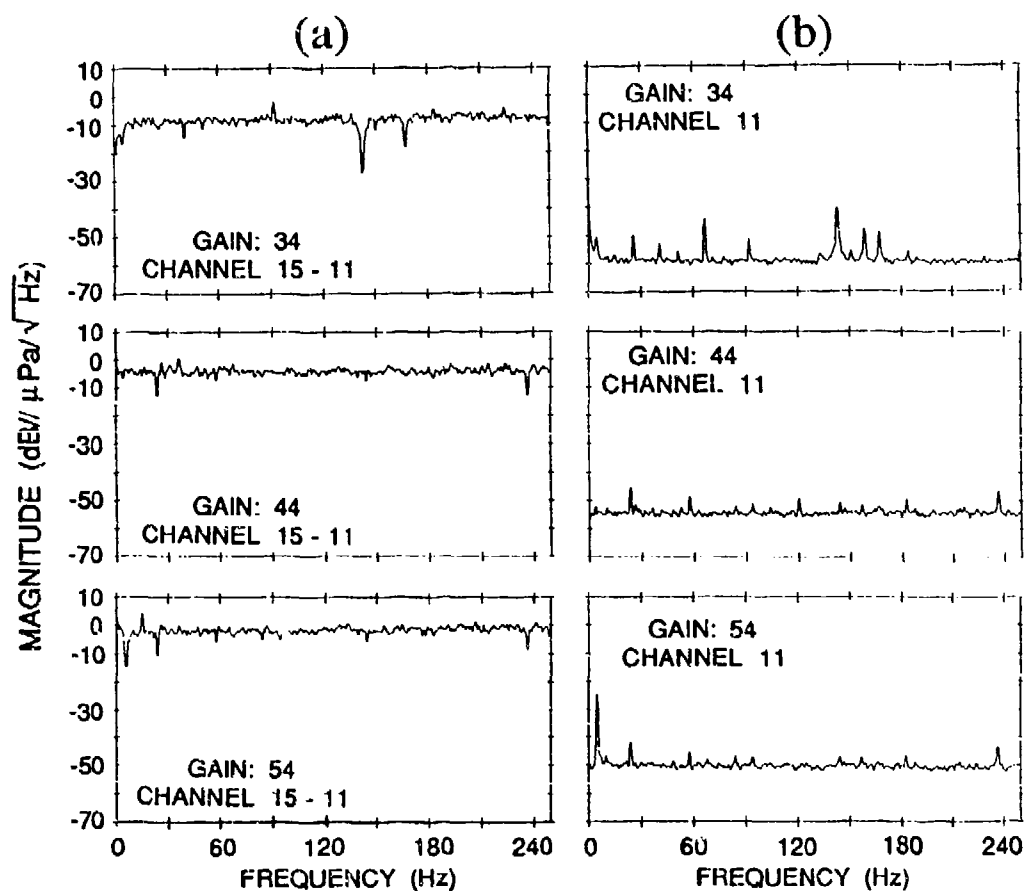
Figure 4 Channel gain difference. Slew rate limitation is suspected as a channel gain discrepancy correlates with transmit distance. The channel transmitting furthest (11) is compared to the closest channel (15). The difference between these channels (a) should ideally be zero at any gain setting. The variable gain stage was changed from 34 dB to 54 dB in 10 dB increments. The expected change in channel spectra level (b) is 10 dB for each increment however the actual measured change for channel 11 is about 5 dB.
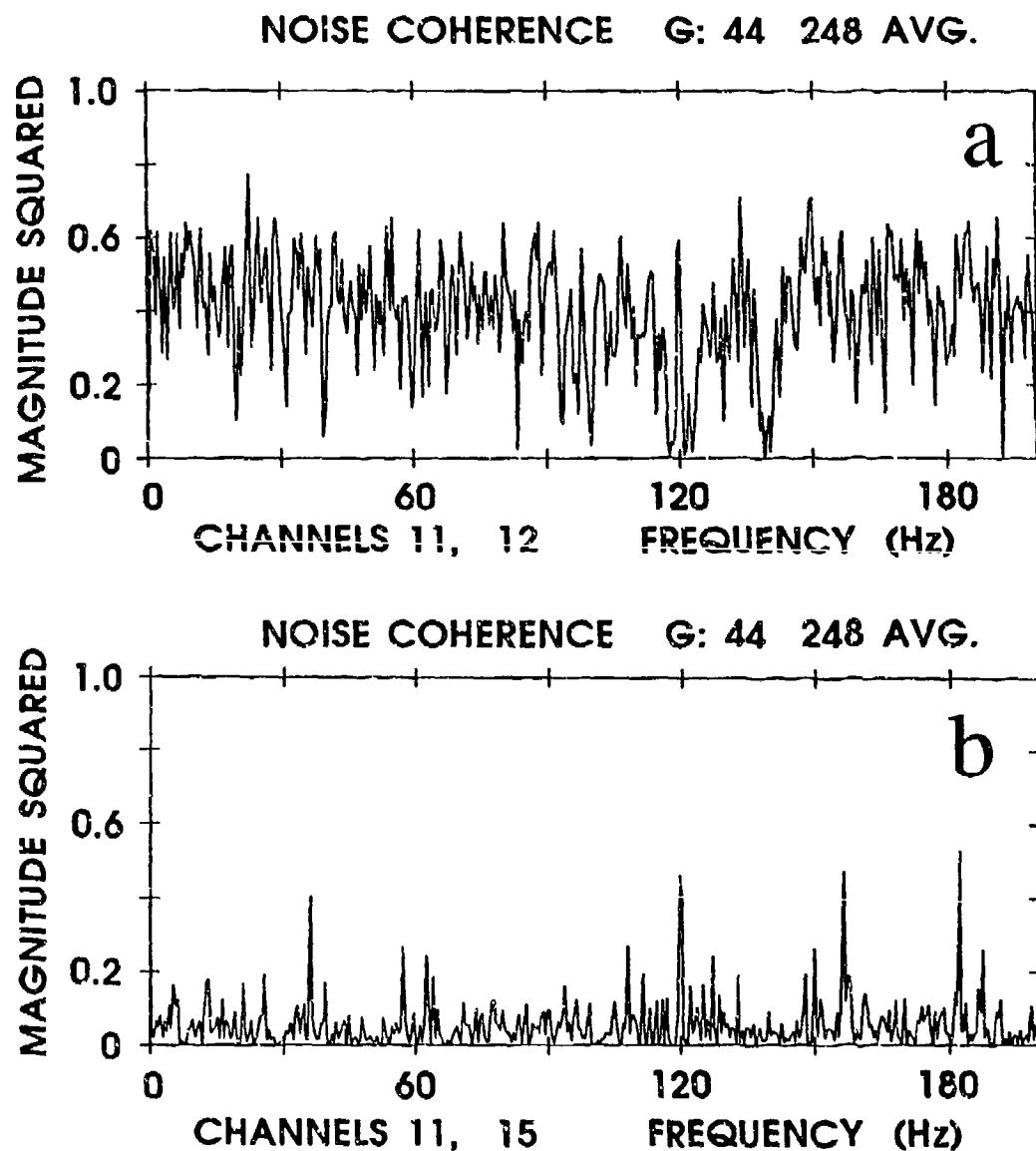
Figure 5 System noise coherence. The coupled noise shows a coherent structure across the array bandwidth. The top panel (a) displays the coherence between the channels at 33.75 m and at 26.25 m. The bottom panel (b) display the coherence between the channels at 33.75 m and at 3.75 m. Pair-wise coherence plots corroborate this result.

BEAMFORMING: AMBIENT NOISE vs. SELF NOISE
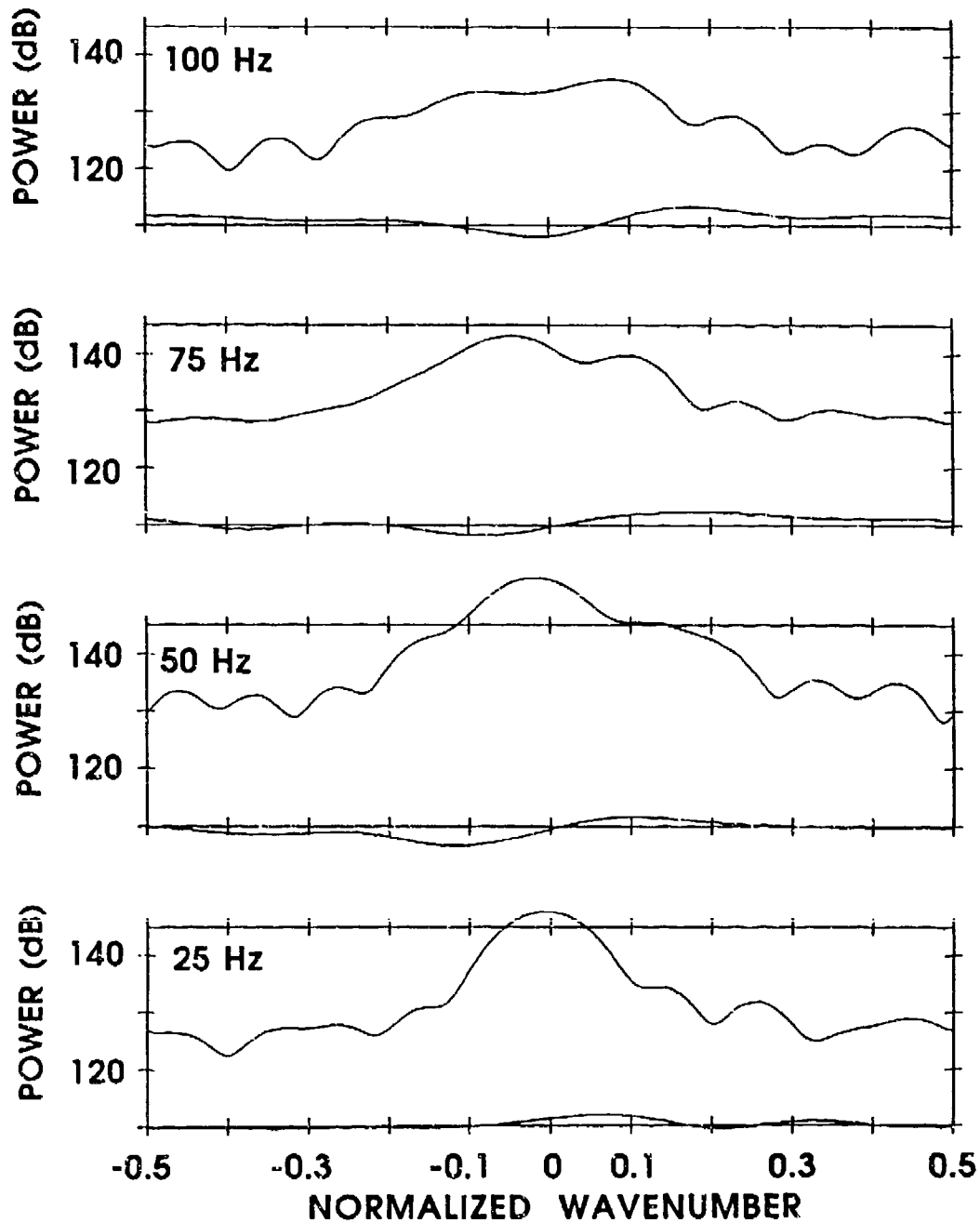
Figure 6 System noise directionality. The coherent noise is significant at only one or two channels per section in the array and does not affect the directionality noise levels which remain below than of the ambient noise.
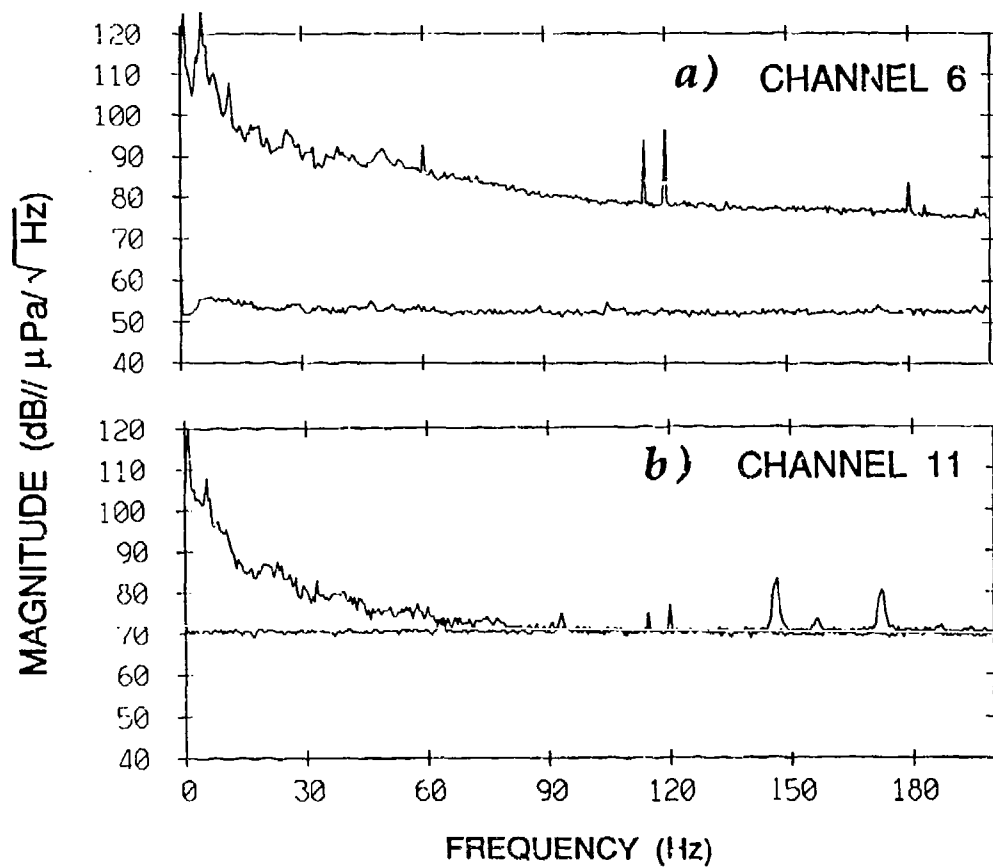
Figure 7 System noise spectral levels. The coherent noise spectral level is of concern as it approaches and possibly exceeds the ambient noise level. This level is dependent on the array gain setting, increasing as the gain decreases. The gain shown here is 34 dB; gain settings during the experiment averaged around 40 dB, with 34 dB used only during high wind conditions.
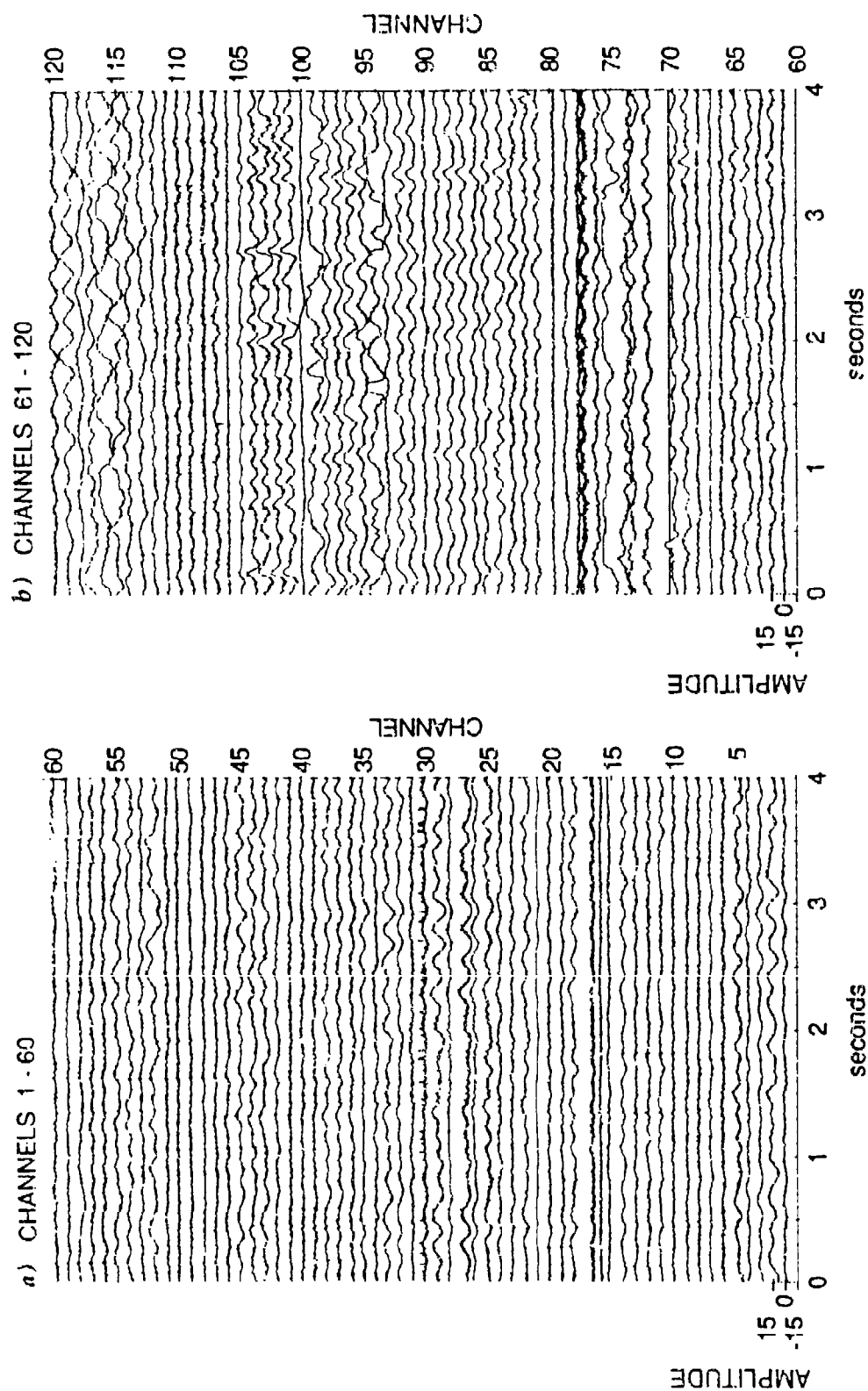
Figure 8 Time series. Two seconds of data is shown for 120 channels. Channel 1 is the deepest channel at about 1300 m. The amplitude is referenced to ±10 VDC at the ADC.

67
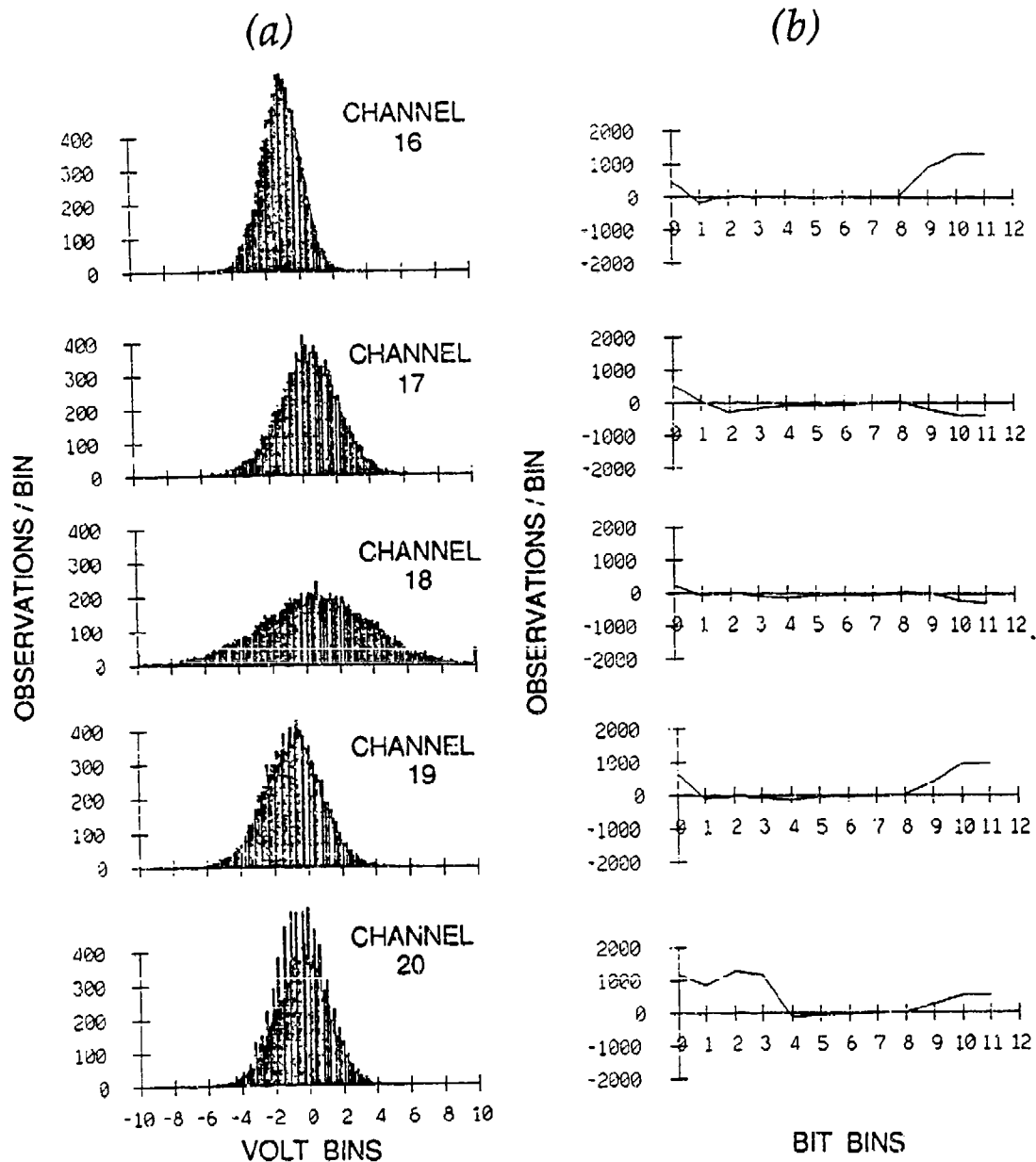
Figure 9 Time series and bit distribution. (a) The distribution for 16 s of the array element time series is calculated as a histogram with a bin width of 0.1 V. (b) The output of the ADC is an offset binary representation of the voltage. The array processors convert this to 2's complement by inverting the most significant bit. The 2's complement samples are used in the same process as the bit distribution simulations to generate the results shown here for the same 4096 samples used in the time series distribution.
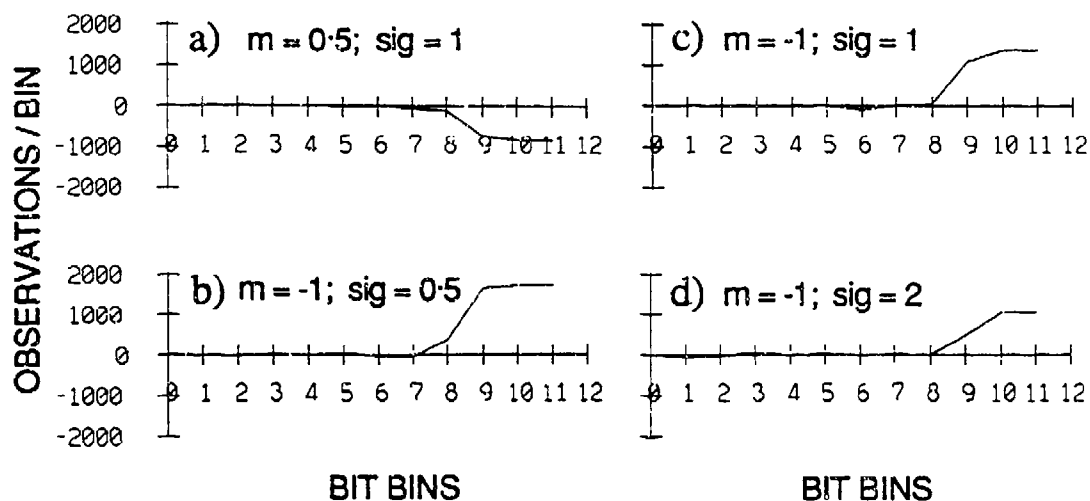
Figure 10 Bit distribution. The 2's complement samples are used in a process which records the number of times each bit is high in a 4096 sample series minus 2048. For a zero mean gaussian random process, this results in a near zero distribution for each bit. A non-zero mean process affects the most significant bits depending on the mean and standard deviation as seen by the simulations (a) mean = 0.5, standard deviation (σ) = 1, (b) mean = -1, σ = 0.5, (c) mean = -1, σ = 1, (d) mean = -1, σ = 2.
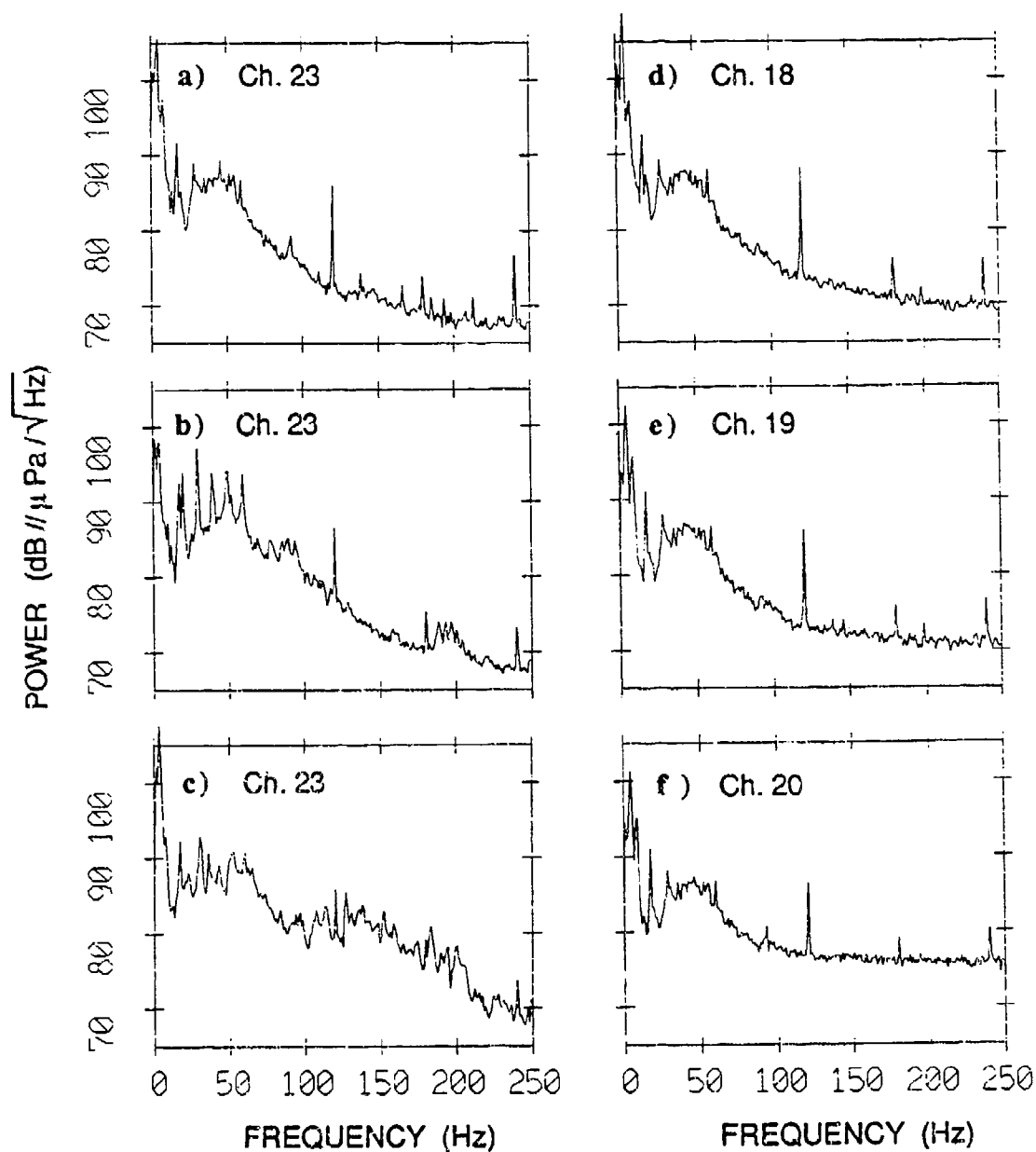
Figure 11 Power spectral density. The spectra were generated by incoherently averaging 15 8192-pt FFT of 50% overlaped, Kaiser-Bessel windowed (α=2.5) time series. The data sequence was 2 minutes in length and the results were plotted as a 16 bin average yeilding a 90% confidence interval of +0.5/-0.4 dB. The spectra show different facets of the ambient noise including (a) a typical array response, (b) local ship noise (low frequency) and a pseudo random code transmission (200 Hz), (c) seismic profiler noise, (d, e and f) the effect of system noise on the high frequency response for channels furthest away (33.75 m) from the processor.
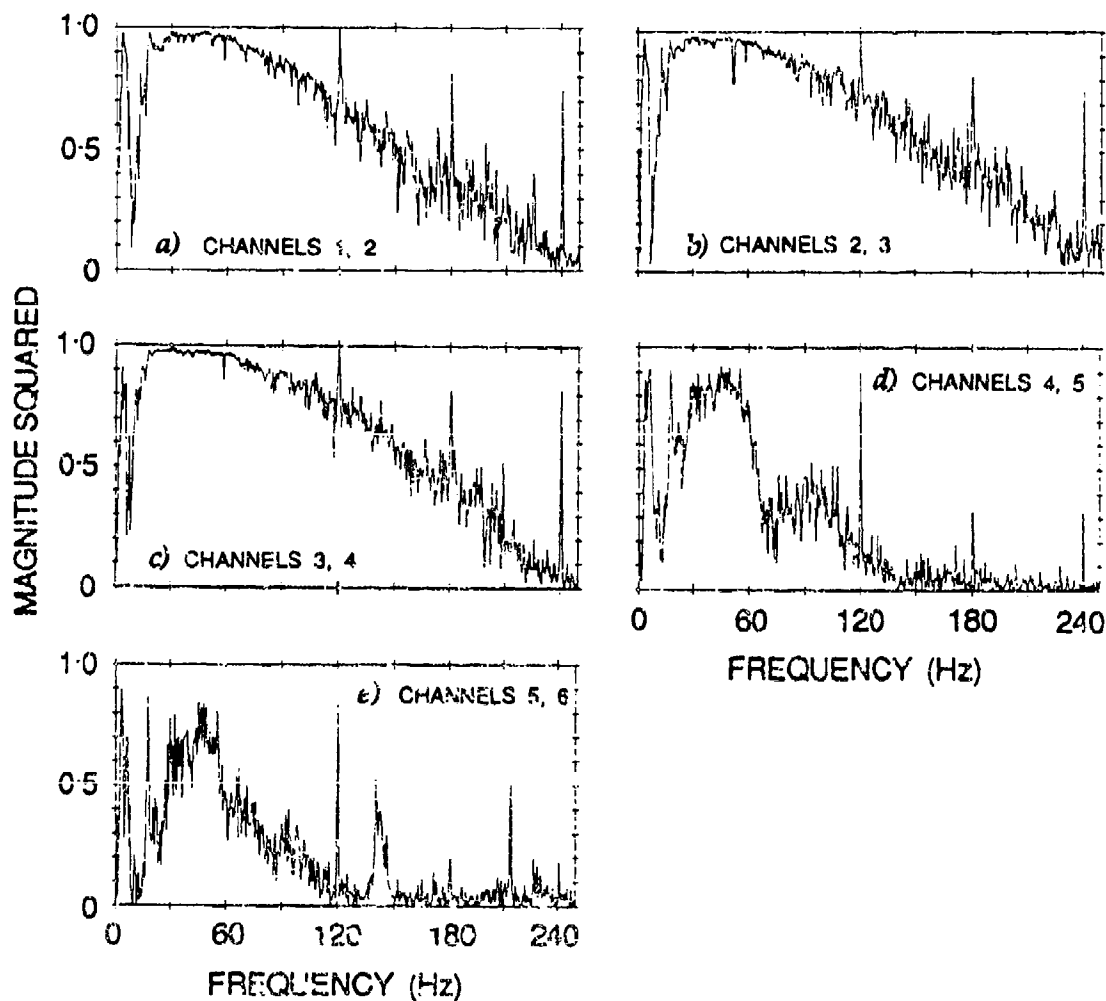
Figure 12 Channel to channel coherence. The coherence is calculated as the magnitude squared cross spectra of the specified channels normalized by the single channel spectra. The results shown in (a), (b) and (c) are typical of vertical ambient noise coherence. The results shown in (d) and (e) indicate the presence of incoherent noise in the channels filtered within the processor case (channels 5 and 6).
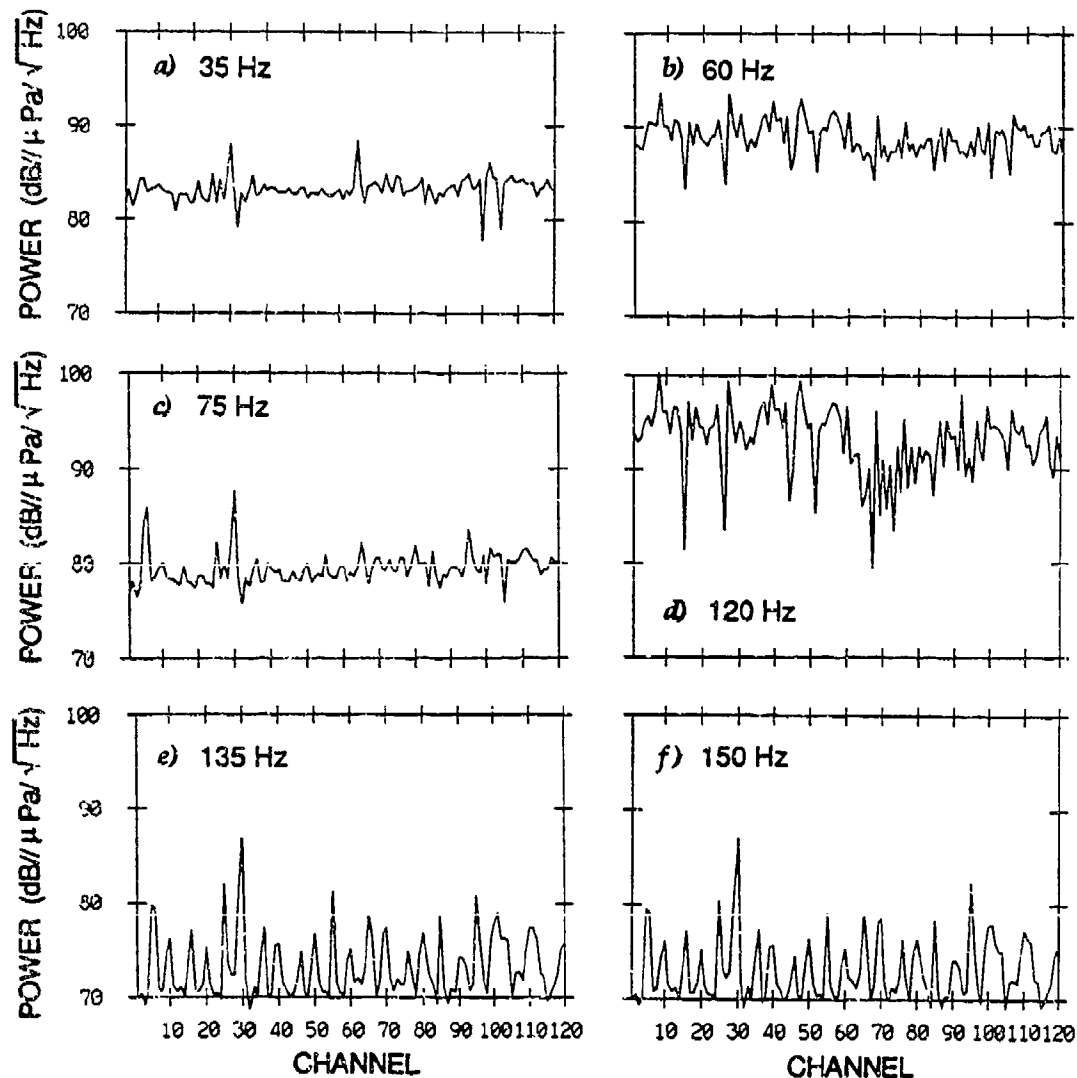
Figure 13 Narrowband spectral estimate. The spectral estimates for a specified bin (0.98 Hz bin width) were incoherently averaged (N = 2583) and plotted against array channel number. The time series were 21.9 minutes long and windowed with a Kaiser-Bessel (α=2.5) function. The frequencies shown represent ambient noise, line frequency and system noise interference distributions.
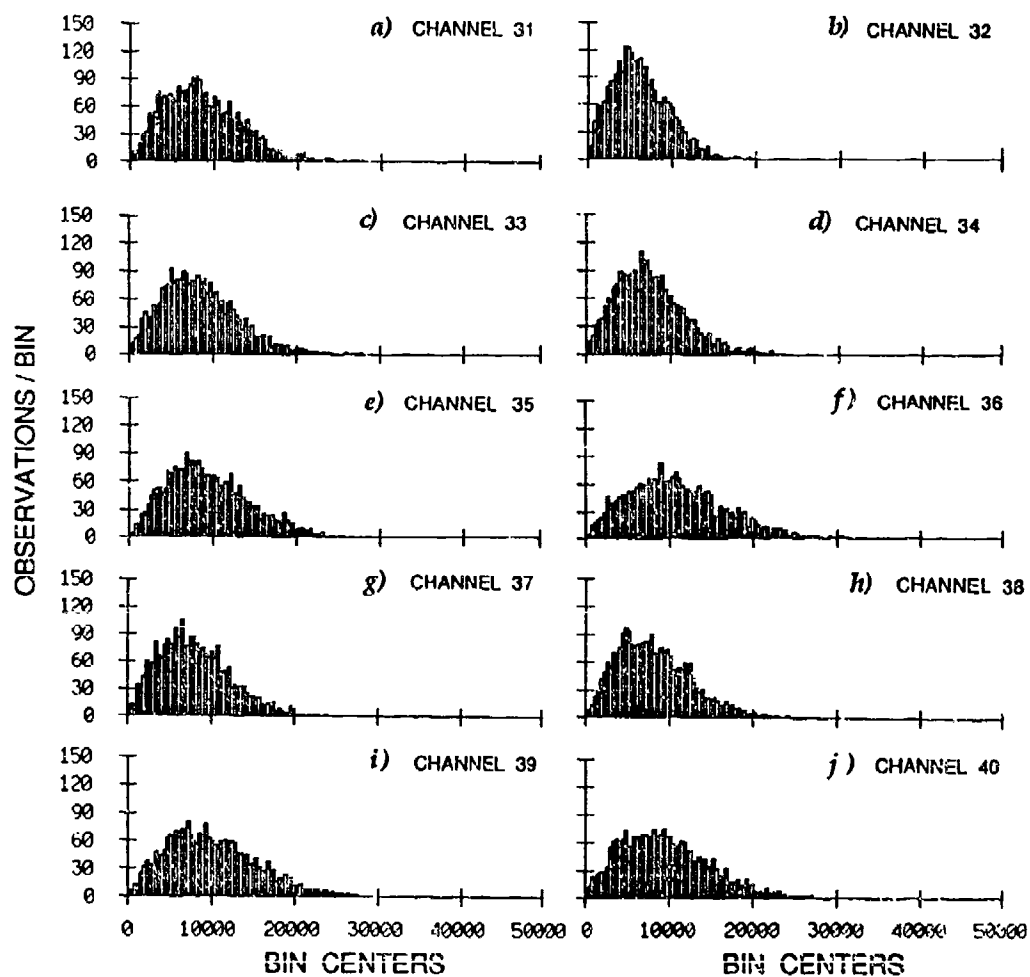
Figure 14 Spectral estimate distribution. The distribution was calculated as a histogram of calibrated (linear) spectral estimates with bin widths of 350 $\mu Pa/\sqrt{Hz}$. Deviation from the expected Rayleigh distribution would require investigation.
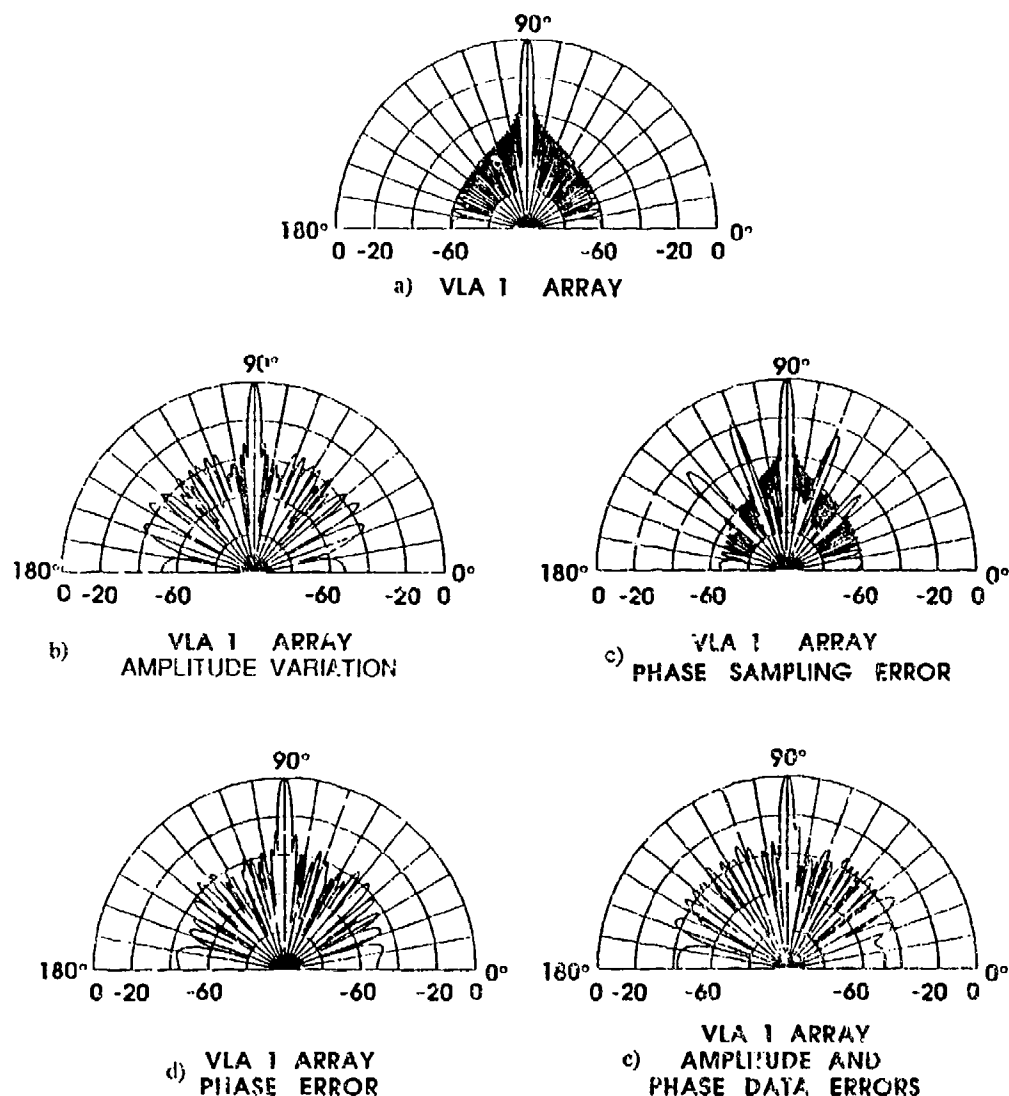
Figure 15 Beampatterns. The array beampatterns were calculated for the 120 element equally-spaced line array at 56 Hz with Kaiser-Bessel shading ($\alpha=1.5$). Errors were introduced in amplitude (b) and phase (c and d) and compared to the theoretical pattern shown in (a). The estimate of the true beampattern incorporating the amplitude and phase calibration errors (e) indicates an almost constant side lobe level at -35 dB.
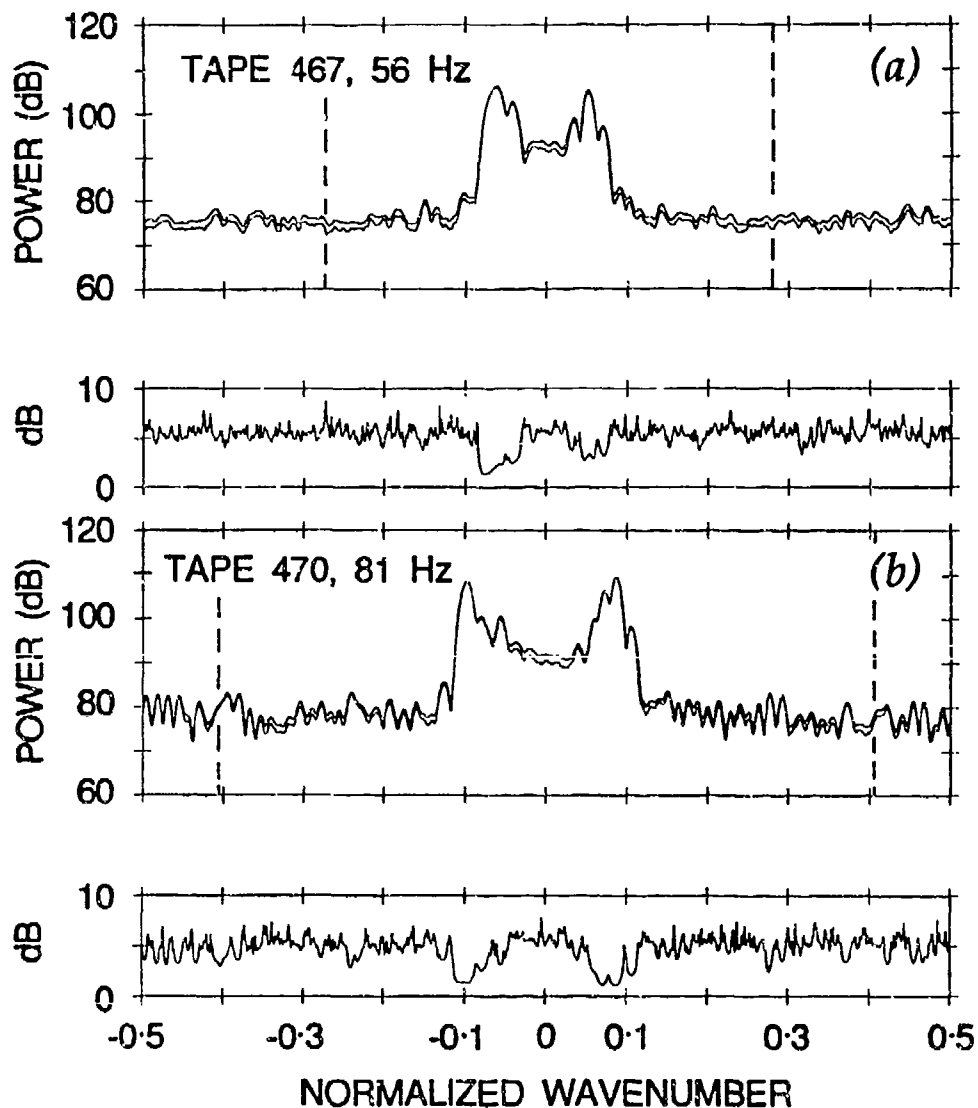
Figure 16 Beam levels. The beam levels are calculated by taking the Fourier Transform of a single frequency bin across the 120 array channels. The result is displayed as a linear average (top curve), a dB average (bottom curve) and the standard deviation of the dB estimates (separate plot). The ordinate is referenced to a watt/Hz/m and the abscissa is normalized phase ($\phi/2\pi$) with positive numbers looking up. The dotted lines mark the visible region.

Figure 17 Beam correlation levels. Correlation between beams (120 Hz) is calculated as a rank correlation coefficient and displayed (magnified by 100) above the main diagonal. The numbers below the main diagonal are zero if the correlation coefficient redefined in terms of the normally distributed function w is accepted at a 5% level of significance. If the correlation is significant, it is displayed as w normalized by its standard deviation and magnified by 10. The first four rows and last four rows have been deleted for display purposes.
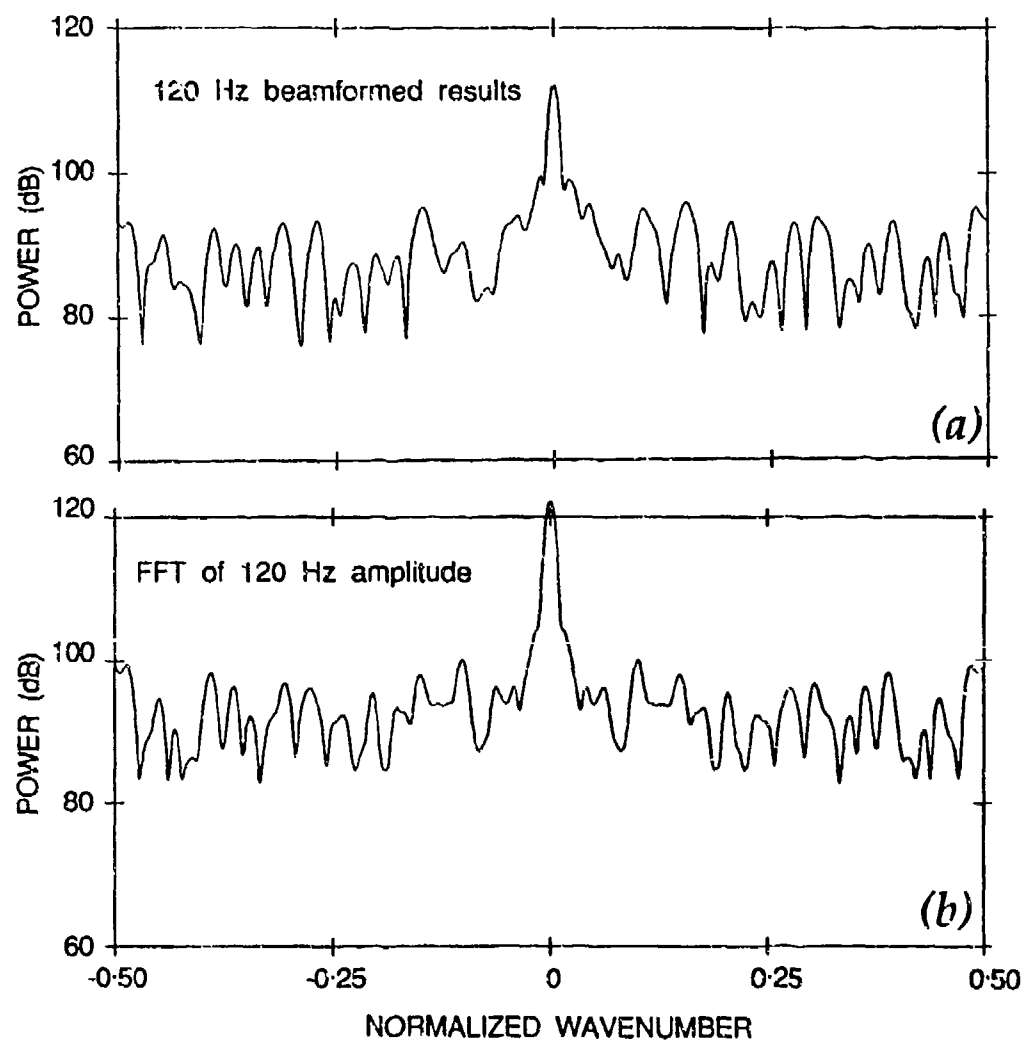
Figure 18 Line frequency spatial distribution. The correlation levels indicated at 120 Hz are shown to be an artifact of the amplitude variations across the array. The beamformed results (a) show a spatial distribution which is very similar to that obtained from the Fourier Transform of the magnitude estimates at 120 Hz (b). The similarity indicates that the arrivals from directions other than broadside are not due to coherent combinations.
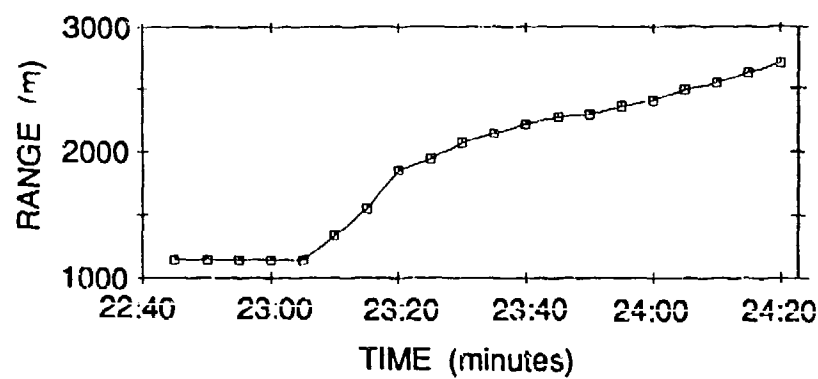
Figure 19 Narrowband transmission range. The range of the narrowband source from the array deployed from *FLIP* were recorded from ship's radar every 5 minutes during the transmissions.
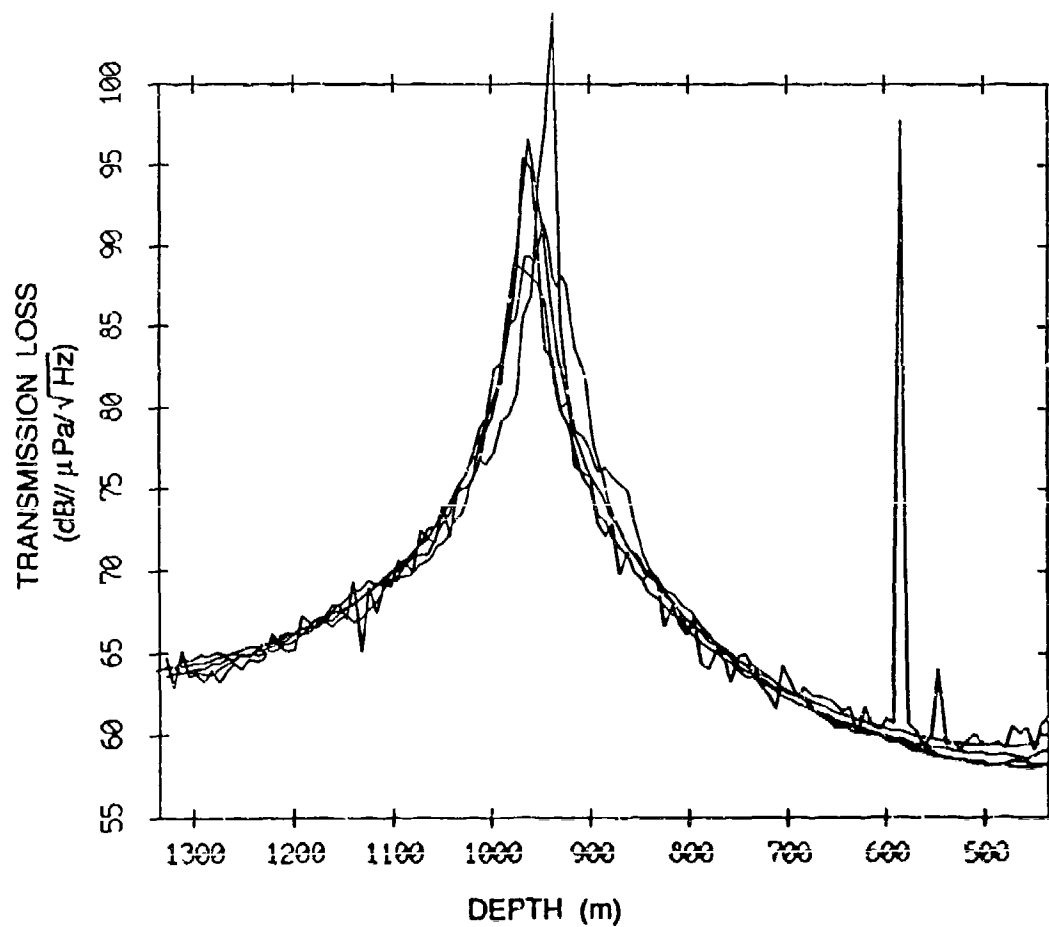
Figure 20 Calibration modeling. The transmission loss estimates of several different propagation models are shown for empirical comparison of the variability at array element depths. Array measurements are also plotted.
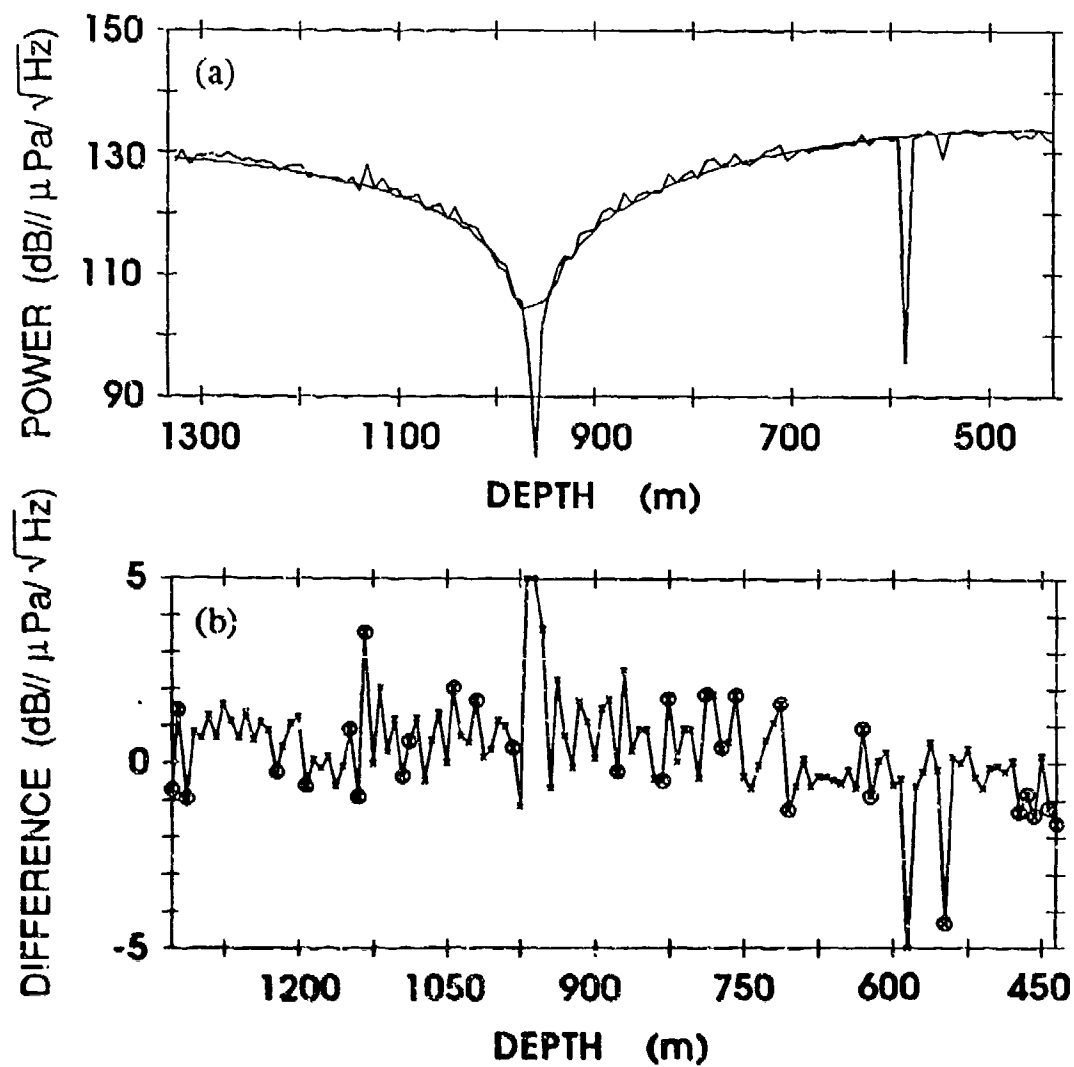
Figure 21 Narrowband magnitude results. (a) The model prediction vs. array data is plotted at 56 Hz. The GSM magnitude prediction is the smooth curve with a deep null at 960 m. (b) The difference between the model prediction and the array response is shown.
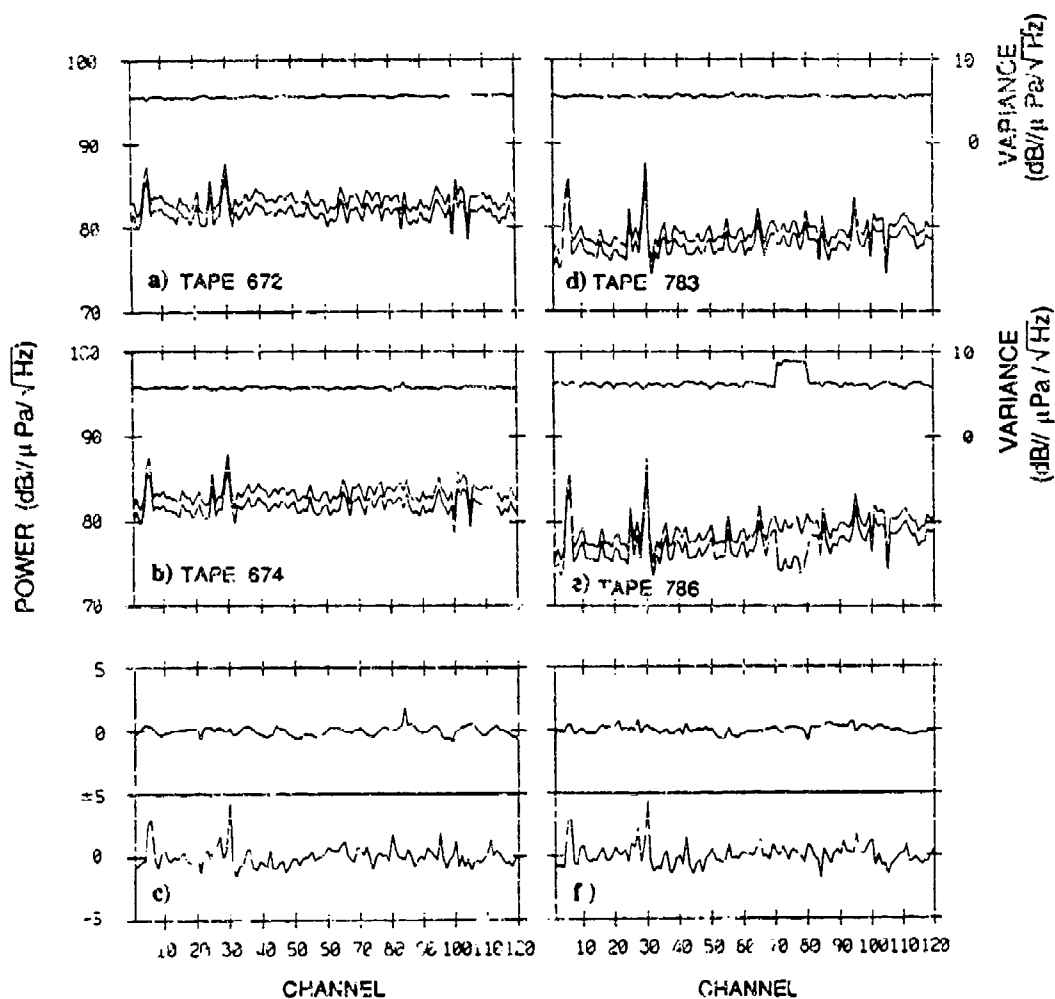
Figure 22 Ambient noise variability. The variation in ambient noise at 75 Hz is shown. The top four panels (a, b, c and d) represent the 75 Hz bin estimate across the array at different times. The smooth curve at the top of each panel is the variance of the dB estimates. The two similar curves in each panel are the linear (top) and dB (bottom) averages. The data was take at four different times during the experiment to reflect 1 hour and 2 day variations: (a) Julian Day (Jday) 266 at 08:53 GMT, (b) Jday 266 at 09:41 GMT, (c) Jday 268 10:09 GMT, (d) Jday 268 11:19 GMT. Array telemetering errors are noticeable in the dB estimates of the data for channels 70-79 in (d); the data were corrected in the linear average which is more sensitive to error.
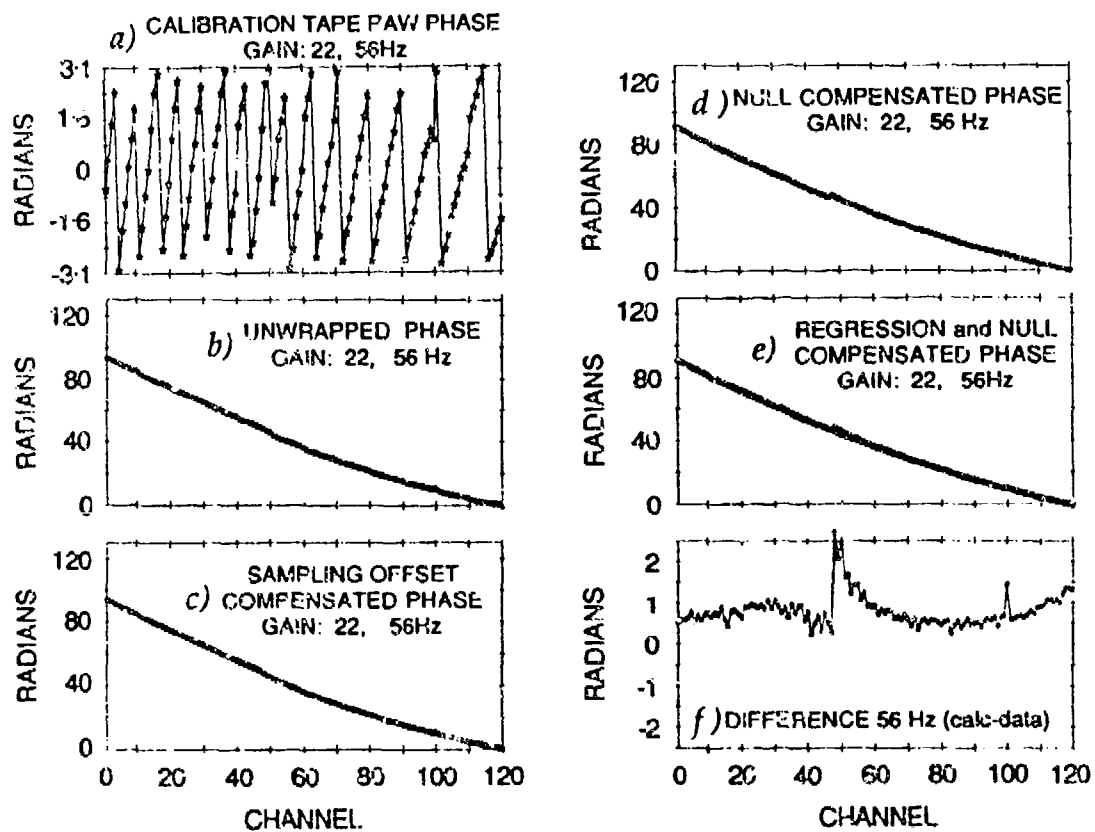
Figure 23 Narrowband phase results. The phase estimate across the array at 56 Hz is calculated from the narrowband calibration transmissions and processed; (a) The phase estimate from a coherent Fourier Transform has an inherent 2π phase shift. This is unwrapped (b) and deviation from the resulting smooth phase change across the array is due to the 0.2 ms sampling offset. Compensating for the deterministic sampling offset (c) reveals a phase shift of π radians at the transmission loss peak. The fully compensated phase curve (d) varies smoothly across the array excep' at the transmission loss peak where the SNR is too low to provide an accurate phase estimate. A multiple (order 3) linear regression (e) is subtracted and the difference (f) is an indication of the array phase error. The curvature of the difference is due to a mismatch in the regression and a more accurate estimate (order 4) is shown in Appendix C.

82
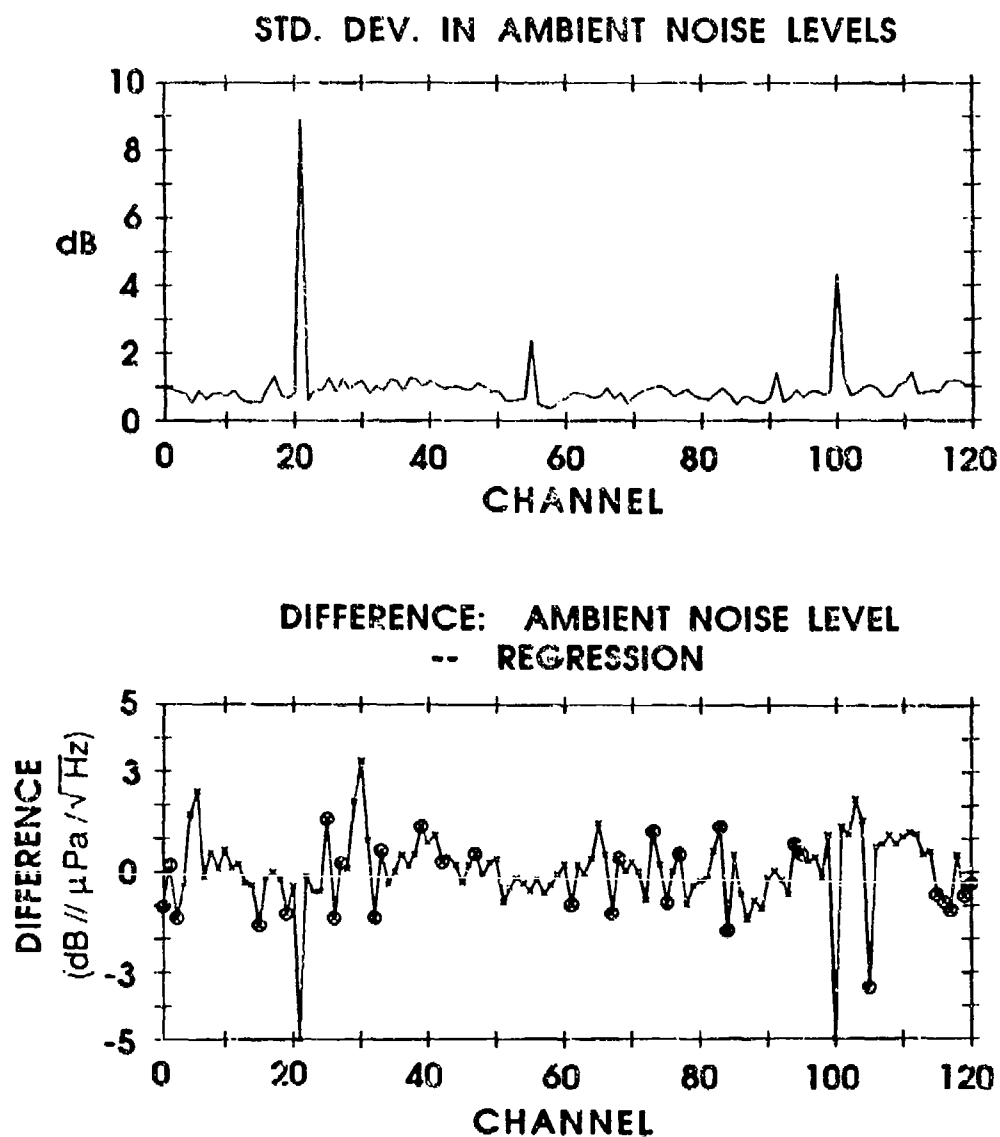
Figure 24 Broadband magnitude results. Ambient noise measurements were used to estimate the spectral levels at 56 Hz for each array channel. These estimates (N=2583) were calculated at 15 different times during the experiment and the results averaged to minimize the variability of the ambient noise. (a) The standard deviation of the 15 different time estimates was calculated. (b) A multiple linear regression was subtracted from the mean. The calibration results using ambient noise